Silke Muckenfuß

Wall Effects in Shear-Flowing Suspensions

Cuvillier Verlag Göttingen

Wall Effects in Shear-Flowing Suspensions

zur Erlangung des akademischen Grades eines
Doktors der Ingenieurwissenschaften (Dr.-Ing.)
von der Fakultät für Chemieingenieurwesen der
Universität Karlsruhe (TH)

genehmigte

Dissertation

von

Dipl.-Ing. Silke Muckenfuß

aus Pirmasens

Dekanin: Prof. Dr. B. Kraushaar-Czarnetzki
Referent: Prof. Dr. H. Buggisch
Korreferent: Prof. Dr. H. Nirschl
Tag der mündlichen Prüfung: 9. Juni 2006

1. Auflage, 2006
Gedruckt auf säurefreiem Papier

Dank

Zum Gelingen dieser Arbeit haben viele Personen auf verschiedene Art und Weise beigetragen. Ganz besonders möchte ich mich bei meinem Doktorvater Prof. Hans Buggisch bedanken, für Vertrauen und Freiheit, für seine fachliche Kompetenz und für den persönlichen und humorvollen Umgangston.

Vielen Dank an

- Prof. Hermann Nirschl für die freundliche Übernahme des Korreferates

- Dr. Bernhard Hochstein für seine stetige, große Hilfs- und Gesprächsbereitschaft

- Herrn Prof. Weber für seinen Beitrag zu einer positiven Stimmung in der Gruppe

- Dietmar Paul, vielen Dank für sehr tatkräftigen Beistand

- Dr. Edme H. Hardy und Emilio Oliver für funktionierende NMR-Experimente und gemütliche Kaffeepausen im NMR-Labor

- anderen Mitarbeitern des MVM-Institutes

- Dominik Nagel, der zwar vorerst nichts mit dieser Dissertation zu tun hatte, mir aber auf anderen Ebenen ganz enorm geholfen hat

- meine liebe Freundin Cora für unzählige schöne Cocktail- und Kinoabende, die bei mir für Schwung und gute Laune gesorgt haben

- meinen Geschwistern Heide und Jan für ihre herzliche Freundschaft und ihr Mitgefühl in kritischen Situationen

- meine Eltern Lieselotte und Klaus für eine andauernde Unterstützung und mehr.

Contents

Chapter 1

Introduction

In many industrial processes the flow behaviour of liquids plays an important role. The macroscopic flow properties as volume flux and pressure loss are determined by the local structure of the flowing substance and production efficiency, optimization processes, security, ecological aspects or quality management might be affected extremely. Within the production of many materials suspensions are involved. The filler material affects the properties of the material that for instance may be paints and varnish, ceramics, pastes and slurries, paper, certain foodstuffs or cosmetics. Also non-industrial fields as medical science (blood circuits) and phenomena in nature like dunes formed by sedimentation are connected with the streaming of a particle-laden fluid. In the shear flow of a suspension hydrodynamic particle-particle interactions lead to stochastic particle movements and the so-called hydrodynamic diffusion takes place. A demixing might be generated if a systematic particle migration orthogonal to the flow direction is induced by gradients of the interaction frequency and of the resistance force to transverse particle movement. These phenomena were investigated experimentally and analyzed theoretically (for instance by Happel and Brenner [12]). A gradient of resistance also affects the particle drift. Such a gradient originates in the vicinity of solid boundary walls or a viscosity gradient. Near the wall the resistance coefficient regarding particle movements orthogonal to the wall is increased. An enhanced relative viscosity coming along for instance with an increased particle concentration also leads to an increased resistance coefficient. A laminar tube flow of a suspension at steady state develops a boundary layer at the wall with a low particle concentration leading to the phenomenon of pseudo wall slip resulting in a decreased pressure difference related to a constant particle flux. Due to inhomogenity the local shear rates, velocities and particle concentrations vary causing differing residence times in the tube and different degrees of mechanical strain.

1

The overall object of this work was the development of a phenomenological theory to describe the wall influence in a shear flow of a suspension combined with an experimental investigation. Due to time constraints the experimental analysis was confined to a chiefly qualitative character. As far as the theory is concerned an approximation of the resistance force under wall influence was set up leading to a new diffusion equation. The model was employed in order to calculate the shear rate profiles, velocity profiles and particle concentration distributions of a shear-flowing suspension including wall influence and gravity as well as the time-dependant gravity effect of a non-flowing suspension. By means of nuclear magnetic resonance (NMR) methods suspensions and solutions were analyzed experimentally to evaluate the model. This powerful technology allows the detection of spin densities of nuclei operating non-invasively. The distinction between protons and non-protons (H-NMR) makes the imaging of particle distributions and velocity profiles in suspensions possible. In this regard a special shearing device featuring an oscillating tube flow was constructed to realize a timely unlimited shearing process.

Chapter 2

Theoretical Background

2.1 Rheological Basics

2.1.1 Definitions

The main topic of the rheology (greek rheos=flow) is the constitutive behaviour of fluids. The relation between resistance and deformation is measured (rheometry), described (phenomenological rheology), expressed by mathematical modelling (theoretical rheology) and interpreted investigating the molecular processes (structure rheology).

The system response to a deformation consists of shear stresses τ_{ij} parallel to the surface areas and of normal stresses σ_{ii} perpendicular to these (cp. fig. 2.1). The representing stress tensor indicating the nomenclature is:

$$\mathbf{S} = \begin{pmatrix} \sigma_{xx} & \tau_{xy} & \tau_{xz} \\ \tau_{yx} & \sigma_{yy} & \tau_{yz} \\ \tau_{zx} & \tau_{zy} & \sigma_{zz} \end{pmatrix}$$

Usually an isotropic pressure p is separated from $\mathbf{S}$

$$\mathbf{S} = -p\mathbf{E} + \mathbf{T}$$

leading to

$$\mathbf{S} = \begin{pmatrix} -p + \tau_{xx} & \tau_{xy} & \tau_{xz} \\ \tau_{yx} & -p + \tau_{yy} & \tau_{yz} \\ \tau_{zx} & \tau_{zy} & -p + \tau_{zz} \end{pmatrix} \quad .$$

τ is called 'extra stress tensor'. A flowing fluid may experience varying normal stresses. In this case the pressure is defined as:

$$\bar{p} = -\frac{(\sigma_{xx} + \sigma_{yy} + \sigma_{zz})}{3}$$
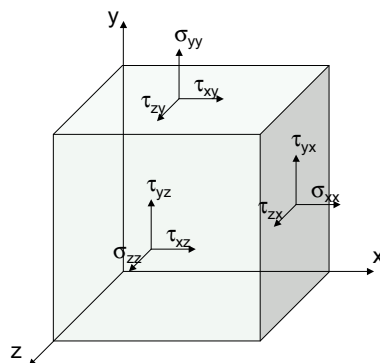
Figure 2.1: Shear stresses and normal stresses of a volume element
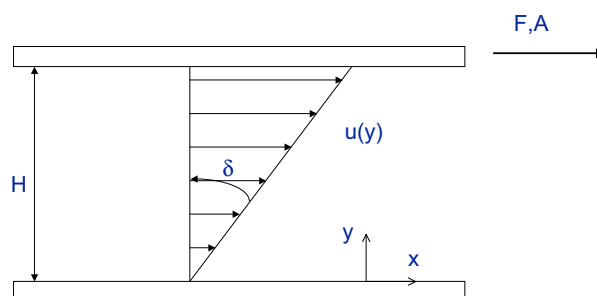
Figure 2.2: Couette Flow

Torque balance proves that $\tau_{ij} = \tau_{ji}$. The kinematics of a simple shear flow (fig. 2.2) results in the extra stress tensor

$$\mathbf{T} = \begin{pmatrix} \sigma_{xx} & \tau & 0 \\ \tau & \sigma_{yy} & 0 \\ 0 & 0 & \sigma_{zz} \end{pmatrix} \quad .$$

Below the definition of the typical rheological properties is explained considering a volume element of a substance between two parallel plates at a distance of H as shown in fig. 2.2 (Couette flow). The element is sheared by moving one of the plates. To pull the plate along the fluid a force F is needed due to the occurring friction that results from molecular momentum transport caused by momentum gradients and molecular interactions. The shear stress τ is defined as the force F per area:

$$\tau = \frac{F}{A}$$

The shear strain γ is defined as the moved distance X per height unit (in the case of a Couette flow it is constant due to the linear velocity profile):

$$\gamma(y) = \frac{dX(y)}{dy} = X/H = \tan \delta$$

Here at the plates no slip is presumed. The shear angle δ is

$$\delta = \arctan \frac{X}{H}$$

The shear rate is the obtained strain per time:

$$\dot{\gamma}(y) = \frac{d\gamma}{dt} = \frac{d(u(y))}{dy} = \frac{U}{H} \tag{2.1}$$

A central rheological property is the dynamic viscosity η. Characterizing the flowability of a substance it is defined as the proportionality factor linking shear rate and shear stress:

$$\eta = \frac{\tau}{\dot{\gamma}} \tag{2.2}$$

The dynamic viscosity strongly depends on temperature. When increasing the temperature fluids show viscosity reduction as the dominating intermolecular interactions are weakened whereas within gases a higher collision rate makes the sliding by of the shear layers more difficult leading to a rise of the viscosity. Furthermore considering suspensions the viscosity is a function of particle size and fibre length, respectively shape of particles and other properties of the system.

Shear rate dependance of viscosity   Fig. 2.3 shows the viscosity dependance on the shear rate of different types of material at steady state. A special case is the newtonian fluid with a constant viscosity with respect to time as well as to shear rate. The most famous example is water. At
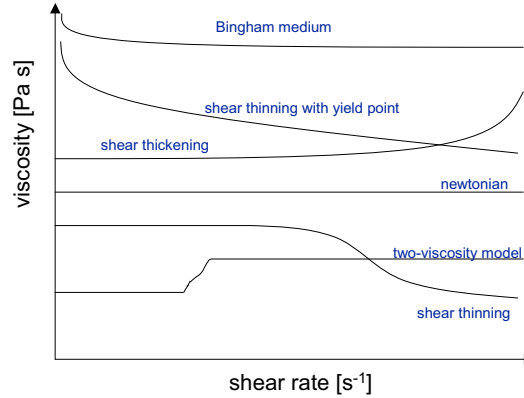
Figure 2.3: Shear rate dependance of viscosity function

higher shear rates the viscosity might decrease due to structural changes within the molecular scale of the substance. This behaviour is called shear thinning or pseudo plasticity showed by polymer solutions mostly. Shear thickening substances basically including some highly concentrated suspensions and dispersions, pastes and slurries, become more viscous at high shear rates leaving the elements of the disperse phase not enough time to sidestep each other generating transverse forces via momentum exchange. Some substances require a certain shear stress till they deform, the shear yield stress, corresponding to an infinite zero-shear viscosity. A typical example for a fluid with shear yield stress τ_F (Bingham fluid) is oil paint. Some shear thinning substances also possess a yielding point. The two-viscosity model represents substances developing two newtonian regions. A common characterization of a non-newtonian fluid is given by the Power Law (Herschel-Bulkley):

$$\eta(\dot{\gamma}) = \frac{\tau_F}{\dot{\gamma}} + k\dot{\gamma}^{n-1}$$

$\tau_F = 0$ delivers the Ostwald/de Waele law whereas $n = 1$ describes a Bingham fluid.

Time dependance of viscosity   Possible time dependances of the viscosity if shearing starting from a state of rest are displayed in fig. 2.4. An increase of the viscosity is called rheopexy, a decrease of the viscosity is
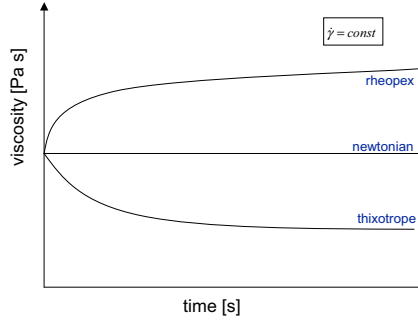
Figure 2.4: Time dependance of viscosity function

called thixotropy. Both types of behaviour occur at disperse systems originating in the structure of the disperse phase. Thixotropy also might be the consequence of changing molecular orientation or rearranging of molecular structures. The responsible mechanisms may be reversible or irreversible.
Every point of the viscosity functions in fig. 2.3 is the asymptotic value of the viscosity for $t \to \infty$ in the diagram of fig. 2.4.

A non-newtonian substance generally shows different normal stresses described by the first and the second normal stress difference:

$$
\begin{aligned}
N_1(\dot{\gamma}) &= \sigma_1(\dot{\gamma}) - \sigma_2(\dot{\gamma}) \\
N_2(\dot{\gamma}) &= \sigma_2(\dot{\gamma}) - \sigma_3(\dot{\gamma})
\end{aligned}
$$

The first and the second normal stress coefficients are defined as:

$$
\begin{aligned}
\Psi_1 &= \frac{N_1(\dot{\gamma})}{\dot{\gamma}^2} \\
\Psi_2 &= \frac{N_2(\dot{\gamma})}{\dot{\gamma}^2}
\end{aligned}
$$

2.1.2 Disperse Systems

The viscosity function of suspensions is dependent on the viscosity of the matrix fluid as well as on the volume concentration ϕ of the disperse phase. A great amount of formulas was created to describe this relation. Our choice is the Krieger-Dougherty equation stated by Krieger and Dougherty [26] valid

for suspensions with a newtonian matrix fluid of the viscosity η_0:

$$\eta(\phi) = \eta_0 \left(1 - \frac{\phi}{\phi_m} \right)^{-2} \tag{2.3}$$

Maximum concentration ϕ_m is the theoretically maximal concentration at which the transition to bulk solid takes place implicating an infinite viscosity. Here $\phi_m = 0.68$. The relative or reduced viscosity $\eta(\phi)/\eta_0$ relates η to the viscosity of the matrix fluid.

Wall slip   Most highly concentrated suspensions possess a yield stress. The system might slide along the wall as between wall and particles a thin layer of pure matrix fluid can be found. If the applied shear stress is less than the yield stress either there is no flow or flow is pure plug flow and there is no wall adhesion. Applying a shear stress higher than yield stress makes internal shear flow possible and there may be a superposition of wall slip and internal shear flow. It is possible to distinct these two by the method of Mooney. It is assumed that the volume flow is composed of the flow rate due to wall slip $\dot{V}_W$ and the flow rate due to shear $\dot{V}_S$:

$$\dot{V} = \dot{V}_W + \dot{V}_S$$

Second assumption is the dependancy of the slip velocity u_W solely on the wall shear stress:

$$u_W = f(\tau_W)$$

Then the total flow rate of a shear flow through a capillary with length L and radius R is:

$$\dot{V} = \pi R^2 u_W + \frac{\pi R^3}{\tau_W^3} \int_0^{\tau_W} \frac{\tau^3}{\eta(\tau)} d\tau$$

$$\Leftrightarrow \quad \frac{\dot{V}}{\pi R^3} = \frac{u_W}{R} + A(\tau_W)$$

Measuring the volume flow using different capillaries with the same ratio L/R (for example with a twin-capillary) gives the slip velocity as the slope in the $L/R, \dot{V}/\pi R^3$-diagram.

Pseudo wall slip   If the shear rates near the wall are significantly higher than farther away flow velocity increases fast within a short distance from the wall. Macroscopical observation might lead to the (wrong) impression that the system is sliding at the wall. This phenomenon is referred to as pseudo wall slip [6].

2.1.3   Rheometers

Devices for measuring rheological properties are called rheometers. There is a great variety of them, each with its own specific advantages and disadvantages. In this section only a small selection is described.

There are many types of rotational rheometers featuring an axially symmetrical design consisting of a rotating and a non-rotating component. Either the torque and with it shear stress or the angular velocity and with it the shear rate can be set obtaining in each case the other parameter being the measured quantity as a response of the system (CSS: Controlled Shear Stress, CSR: Controlled Shear Rate). Significant advantages are the realizability of different geometries, different basic tests including oscillating shear, a wide working range and the possibility of investigating the normal stresses. Within the following specific description of rotational rheometers no slip is assumed.

Parallel Plate Rheometer

The rotating element is a plate (fig. 2.5). As the local angular velocity ω of
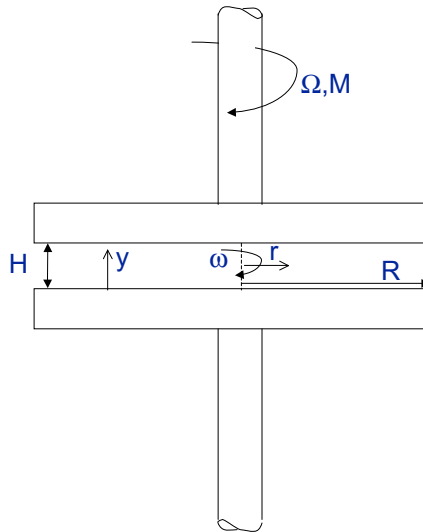
Figure 2.5: Parallel plate rheometer

a layer of liquid is dependant on the position y and the angular velocity of

the upper plate Ω

$$\text{with} \quad \omega(y) = \Omega \frac{y}{H}$$

and thus the circumferential velocity alike $\quad u(r,y) = r\frac{\Omega}{H}y$

the shear rate (2.1) is not constant in this case (for denotation cp. fig. 2.5). Approximately the shear rate is:

$$\dot{\gamma} = \frac{du}{dy} = \frac{r\Omega}{H} \tag{2.4}$$

The shear stress can be determined out of the torque:

$$M = \int_0^R r\tau(r)2\pi r\,dr \qquad .$$

In case of a Newtonian fluid with

$$\tau(r) = \eta\dot{\gamma}(r) = \frac{\eta r\Omega}{H}$$

the shear stress at the border is

$$\tau(r = R) = \frac{2M}{\pi R^3} \qquad .$$

For non-newtonian fluids a correction is needed to obtain $\tau(r = R)$ from M [29].

Cone plate rheometer

The sensor is a rotating cone with a very flat cone angle α instead of a plate (fig. 2.6). In contrast to the parallel plate rheometer the shear rate is constant according to

$$\dot{\gamma} = \frac{du}{dy} = \frac{dr\Omega}{dr\tan\alpha} \approx \frac{\Omega}{\alpha} \tag{2.5}$$

since the height is $h(r) = r\tan\alpha \approx r\alpha$
and the circumferential velocity of the plate $u(r) = r\Omega$.
With the torque equivalent to that of the parallel plate rheometer

$$M = \int_0^R r\tau 2\pi r\,dr \tag{2.6}$$
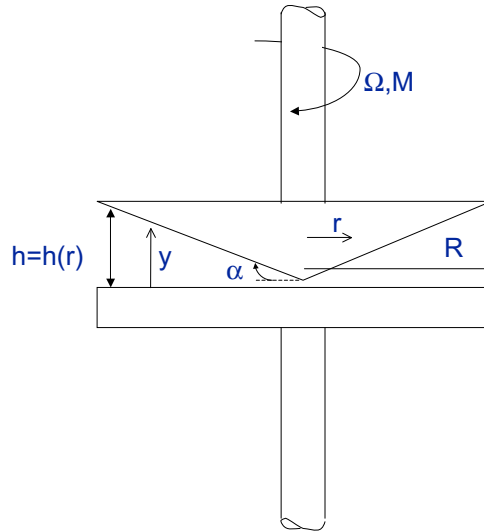
Figure 2.6: Cone plate rheometer

and the resulting shear stress

$$\tau = \frac{3M}{2\pi R^3} \tag{2.7}$$

the viscosity measured is (2.5, 2.7):

$$\eta = \frac{3M}{2\pi R^3}\frac{\alpha}{\Omega}$$

2.1.4   Shear Tests

Linear Shear

The most common shear tests are the creep experiment featuring steady shear $\dot{\gamma} = const$ and the stressing experiment characterized by constant shear stress $\tau = const$.

The time-dependant reaction $\tau(t) = G(t)\gamma$ after applying a shear strain step (relaxation test) shows the capacity for remembering of the substance described by the shear modulus $G(t)$ comprising the characteristic relaxation times λ_i and the associated individual values of the storage moduli g_i accord-

ing to

$$G(t) \;=\; \sum_i g_i \exp(-t/\lambda_i) \quad .$$

The relaxation spectrum (λ_i, g_i) is not well-defined. Usually for a certain system various sets of fitting relaxation times λ_i and corresponding moduli g_i can be found. Hereby the number of relaxation times (and moduli) may vary as well.

Oscillatory Shear

The behaviour of a viscoelastic material undergoing oscillatory shearing is a result of the combination of viscous and elastic characteristics of a material:

$$\gamma(t) \;=\; \hat{\gamma}\sin(\omega t)$$
$$\dot{\gamma}(t) \;=\; \hat{\gamma}\omega \cos(\omega t)$$

The occurring shear stress consists of a viscous component represented by the loss modulus G'' and an elastic component described by the storage modulus G' (fig. 2.7):

$$\tau(t) \;=\; G'\hat{\gamma}\sin(\omega t) + G''\hat{\gamma}\cos(\omega t)$$

The elastically stored energy represented by the storage modulus G' becomes maximal at maximum strain, the maximum of the dissipated energy (viscous behaviour) described by the shear loss modulus G'' is the point of the maximum shear rate that is the the middle position being the zero-point of strain. As a result the run of the shear stress is shifted by a phase difference $\delta(\omega)$ ($\hat{\tau}$ is the amplitude)

$$\tau(t) = \hat{\tau}sin(\omega t + \delta(\omega))$$
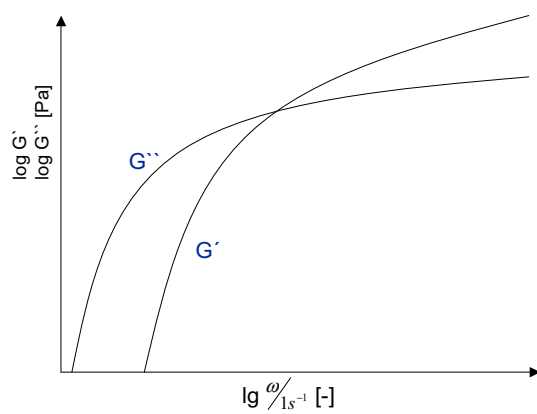
Figure 2.7: Frequency dependance of storage modulus and loss modulus (oscillatory shear)

2.2 Hydrodynamic Diffusion

Considering creeping shear flow without inertia from the Navier Stokes differential equations and the force and momentum equilibria of the particles follows zero transverse force acting on single floating neutrally buoyant spheres [42].
The global dynamic lift force composed of

the Saffman force [40]: In case of non-neutrally buoyant spheres the density difference induces a velocity slip. In vertically upward flow the velocity profile of the particle system varies from that of the matrix fluid. If the particle density is lower than that of the fluid they flow faster than the fluid, if they possess a larger density than the fluid they are slower than the fluid. The direction of the particle migration is determined by the velocity difference between the particle and the flanking streamlines. The particles migrate towards the larger difference where the pressure is lower. Thus the interaction between slip velocity and shear causes a transverse force.

the force due to a curvature of the velocity profile [23]: A curved velocity profile (e.g the parabolic profile of a Poiseuille flow) leads to different relative (to the particle velocity) fluid velocities tangent to the particle causing again a pressure difference and a force-dipole. Particles migrate in the direction of lower pressure and therefore towards larger relative fluid velocities (corresponding to higher shear rates).

the Magnus effect / Rubinow-Keller force [43]: The interaction of particle rotation and shear leads to a pressure reduction on the side with rotation resulting in a tangential velocity pointing in the same direction like the fluid velocity causing a transverse force directed likewise.

can be neglected because in all these cases the effects originate from inertia. Still particles move transverse to the flow direction leading to demixing or structuring eventually. The origin lies in the mechanism of hydrodynamic diffusion.

2.2.1 Theory of Hydrodynamic Diffusion

According to the theory of hydrodynamic dispersion, also known as 'hydrodynamic diffusion', in shear flow of suspensions statistical velocity fluctuations occur due to hydrodynamic particle interactions. This leads to a homogenous redistribution of particles taking place continuously and possibly to a systematic

particle drift transverse to flow direction.

Moving particles that come near each other are imagined to affect their paths. They give way and return afterwards to their original courses if the interaction was reversible (as arising from the linearity of the Stokes equations). In reality the interactions are always irreversible. An explanation may be the chaotical behaviour of the system. If the system is very sensitive relating to the initial conditions a slight change of these or a small imperfectness entails an extreme impact on the subsequent states. After the interaction the particle might end up on another streamline having experienced a displacement at random direction in average. This leads in a suspension featuring a homogenous particle distribution without relevant gradients (cp. section 2.2.2) to a continuous mixing of the disperse component.

This mechanism and effects of hydrodynamic diffusion is not to be confused with the Brownian motion of the particles and the resulting interactions and displacements described by Fick's law.

2.2.2 Shear-Induced Particle Drift Transverse to Flow Direction

We look at the creeping plane shear flow of a suspension without inertia effects. The particles are monomodally distributed rigid spheres and big enough for rendering the Brownian motion insignificant. That is diameters are $1 - 10\mu$m minimum depending on the present velocities. Certain gradients might induce a systematic particle drift orthogonal to the shear direction. The net particle transport is not connected with movements of a single particle but a purely statistical and collective phenomenon related to the entirety of the system. It is caused by gradients of interaction frequency that come along with gradients of concentration and shear rate and by gradients of the dynamic viscosity that may be caused for example by a gradient of the particle concentration.

Particle drift due to gradients of interaction frequency We picture the particles as passing by each other on neighboring streamlines. As a particle-particle interaction results in moving the involved particles the probability of a particle changing its place is growing with increasing interaction frequency. Thus an overall particle drift in the direction of lower interaction frequency is generated. The interaction frequency $\phi\dot{\gamma}$ is linearly dependant on the particle volume concentration ϕ as the more particles pass by the more interactions happen and also on the local shear rate $\dot{\gamma}$ since the greater the velocity difference of the two streamlines the more interactions take place in

the same time interval. Thus the particles drift from higher to lower particle concentrations and from higher to lower shear rates.

Particle drift due to gradients of resistance force The resistance force $F_\perp$ onto a particle moving across the shear direction determines the distance a particle is dislocated by an interaction. The higher the resistance force respectively the viscosity of the fluid the shorter is the covered distance. As on the average particles moving in the direction of lower resistance force move farther than particles moving in direction of higher resistance force, a particle drift in the direction of lower resistance force is induced.

Particle drift due to curvature of streamlines The particle transport in the direction of less streamline bending [4] is neglected here.

Diffusion Equation

Phillips et al. [33] have set up a diffusion equation to describe the shear-induced particle migration.
The particle flux $\vec{N}_f$ through an area element out of a volume element orthogonal to flow direction due to a gradient of interaction frequency is proportional to the particle concentration. Additionally a dimensionless material independent diffusion coefficient k_f and, according to dimension-analytical considerations, a factor a^2 as the radius a of the particle is the relevant length unit are needed. Therefore the local particle flux is calculated as

$$\vec{N}_f = -k_f a^2 \phi \nabla(\phi\dot\gamma) \quad . \tag{2.8}$$

The particle flux due to the gradient of the resistance coefficient $F_\perp/u_P = 6\pi\eta a$ scales with $\frac{\nabla(F_\perp/u_P)}{F_\perp/u_P}$. Further proportionality factors are again a^2 and an adequate diffusion coefficient k_η as well as the interaction frequency and the particle concentration

$$\vec{N}_\eta = -k_\eta a^2 \phi^2 \dot\gamma \frac{\nabla\,(F_\perp/u_P)}{F_\perp/u_P} \quad . \tag{2.9}$$

The total particle flux is

$$\vec{N} = \vec{N}_f + \vec{N}_\eta \quad .$$

Here the resistance force acting on a particle is the Stokes force

$$F_{St} = 6\pi\eta a u_P \quad . \tag{2.10}$$

This was found independently by Navier [30] and by Stokes [44, 45] deduced from the Navier-Stokes equations as the resistance force acting on a particle

due to friction valid in an infinite expanded homogenous and parallel approaching flow field without inertia effects. u_p shall be the particle velocity across the shear direction. With (2.10) the particle flux due to the gradient of resistance force corresponds to the gradient of the dynamic viscosity (Leighton and Acrivos [27]):

$$\frac{\nabla\left(F_\perp/u_P\right)}{F_\perp/u_P} = \frac{\nabla 6\pi\eta a}{6\pi\eta a} = \frac{\nabla\eta}{\eta} \tag{2.11}$$

and with (2.9)

$$\vec{N}_\eta = -k_\eta a^2 \phi \dot{\gamma}\frac{\nabla\eta}{\eta} \tag{2.12}$$

The diffusion coefficients were determined experimentally by Leighton and Acrivos [27] and others. The diffusion equation results from the mass balance:

$$\frac{\partial\phi(y,t)}{\partial t} = -\nabla\vec{N} \tag{2.13}$$
$$= -\nabla\left(-k_f a^2\phi\nabla(\phi\dot{\gamma}) - k_\eta a^2\phi^2\dot{\gamma}\frac{\nabla\eta}{\eta}\right)$$

In the case of a fully developed one-dimensional simple shear flow with flow direction as x-direction and y-direction for direction of shear gradient, the particle flux is limited to its y-component and the diffusion equation is

$$\frac{\partial\phi(y,t)}{\partial t} = -\frac{\partial}{\partial y}N \tag{2.14}$$
$$= -\frac{\partial}{\partial y}\left(-k_f a^2\phi\frac{\partial}{\partial y}(\phi\dot{\gamma}) - k_\eta a^2\phi^2\dot{\gamma}\frac{\frac{\partial}{\partial y}\left(F_\perp/u_P\right)}{F_\perp/u_P}\right) \tag{2.15}$$
$$= -\frac{\partial}{\partial y}\left(-k_f a^2\phi\frac{\partial}{\partial y}(\phi\dot{\gamma}) - k_\eta a^2\phi^2\dot{\gamma}\frac{\frac{\partial}{\partial y}\eta}{\eta}\right) \quad.$$

This equation describes the temporal development of the particle concentration distributions due to hydrodynamic diffusion. At steady state the various particle fluxes are balanced.

An alternative description of the shear-induced velocity fluctuations in monodisperse suspension is the concept of the 'granular temperature' as a measure of the extent of fluctuations (Jenkins and McTigue [25], enhanced by Nott and Brady [31]). This model will not be used here.

2.2.3 (De)mixing and Structuring Phenomena

Various resulting phenomena originating in a net particle drift due to hydrodynamic diffusion were predicted theoretically, investigated by numerical

simulations or observed experimentally. The applied experimental methods include visual registration of tracer particles (Eckstein et al. [14], van Breedveld [11]), infrared spectroscopy, laser-Doppler techniques, ultrasonic spectroscopy and nuclear magnetic resonance imaging. Numerical Simulations of hydrodynamic and nonhydrodynamic interactions were performed basing on the Stokesian dynamics investigating for instance the autocorrelation functions or probability distribution functions of the transverse velocity components [15, 10]. In 1836 Poiseuille [36] stated an inhomogenous radial distribution of red and white corpuscles in blood flow implying a deviation from ideal Poiseuille flow. Demixing in shear flow was observed first by Segré and Silberberg [42] noticing a circular accumulation of particles in pipe flow with small Reynolds numbers at approximately $r = 0.62R$ (r is radial coordinate, R is radius of tube). The reasons of the so-called ′tubular pinch effect′ are the transverse lift forces due to (weak) inertia and particle rotation, and lift due to the curved velocity profile (cp. the beginning of section 2.2). Shear induced particle migration phenomena due to hydrodynamic diffusion were observed first by Gadala-Maria and Acrivos [16] showing as a long-term viscosity decrease in a cylindrical Couette flow. Leighton and Acrivos [27] found that the reason was a particle drift out of the gap into the reservoir beneath. Furthermore they reported a short-term viscosity increase that also could be traced back to diffusion processes respectively to particle drift along the shear rate gradients. Beyond they noticed an accumulation of particles behind an advancing meniscus during the procedure of filling in the rheometrical devices. Since then various experimental investigations indicated nonuniform particle distributions in shear flow. In tube flow particle depletion near the wall coming along with a flattened velocity profile was detected by magnetic resonance imaging (Hampton et al. [38]), by infrared spectroscopy (Hartmann [34]), by laser-Doppler techniques (Koh et al. [13], Abbott et al. [1]) and by the use of tracer particles (van Breedveld [11], Eckstein et al. [14]). Some authors mention that in order to attain particle migration the particle concentration has to overstep a certain threshold [35].

Tube flow   As in Poiseuille flow the shear rates increase with decreasing wall distance according to the diffusion model by Phillips et al. [33] particles are not homogenously distributed at steady state due to hydrodynamic diffusion caused by shear rate gradients. Along the tube axis the particles concentrate whereas at the wall a thin layer without particles can be found (Lyon and Leal [28], [48]). This was observed by Abbott and coworkers [24] per MRI. Hampton et al. [38] also analyzed particle distributions in tube flow by MRI and found out that the diffusion model by Phillips fitted the

better the smaller the ratio of particle radius to tube radius r/R. The generated gradients of particle concentration and relative viscosity flatten the velocity profile (Phillips et al. [33], Shauly [1]). The reduction of the integral viscosity of a suspension flowing through a thin capillary coming along with an assembling of particles at the tube axis due to shear rate gradients is called 'sigma effect' [41, 13].

Cylindrical Couette flow   Phillips et al. [33] calculated that the particles in a Couette flow migrate to the outer cylinder and verified this phenomenon by the use of NMR similar to Abbott et al. [24]. Although experimental investigations have shown that the particle drift is directed from higher to lower shear rates the calculations of Haber and Brenner [21] predict that also the contrary leading to a meta stable state might be the case under particular circumstances. Furthermore they calculated the particle fluxes, velocity and viscosity fields due to viscosity gradients in a Couette rheometer accompanied by experiments.

Parallel plate flow and cone plate flow   The theoretical models so far lack in complexity to describe these flow situations sufficiently. The experimentally investigated particle distributions in a parallel plate and in a cone plate rheometer indicate that within parallel plate flow (e.g. measured per MRI by Chow et al. [5]) particle migration seems to be weaker than in cone plate flow.

Wall effects   Wall slip effects and boundary layers in tube and Couette flow have been observed by rheological measurements (e.g. Yilmazer [47]).

Resuspension of sedimented particles   The shear-induced resuspension of a sedimentated suspension due to hydrodynamic interparticle interactions was observed by Schaflinger et al. [46] and by Leighton and Acrivos [27]. The separation interface in terms of a discontinuity of the particle concentration does not disappear completely.

Polydisperse suspensions   Shauly [4] extended the concept from Phillips to polydisperse suspensions. The calculation referring to a Couette flow lead to a particle migration to the outer cylinder and an intern demixing of the particles with the bigger particles located outwards. This was observed per MRI by Abbott et al. [24].
An investigation of the correlation between hydrodynamic diffusion and agglomeration is described in [7].

2.3 Nuclear Magnetic Resonance (NMR)

2.3.1 The Quantum State of a Nucleus

The effect of nuclear magnetic resonance depends on the existence of a nuclear magnetic moment. Due to the interaction with a static magnetic field there exists an energy splitting between the different allowed states of the nucleus, being degenerate before. Electromagnetic irradiation at the right frequency enables transitions between the different nuclear states. By changing population of the different nuclear energy levels as well as establishing phase coherence between the magnetic moments in the sample leads to detectable magnetization. As the magnetic moments undergo Larmor precession $\omega = \gamma B$ an oscillating voltage may be detected by a detection coil.

In absence of a time dependant magnetic field

The spin quantum number I of a nucleus indicates the magnitude of its angular momentum $\vec{I}$ consisting of orbital angular momentum and eigen angular momentum with

$$\begin{aligned} |\vec{I}| &= \sqrt{I(I+1)}\hbar \\ (\hbar &= \frac{h}{2\pi} \quad , h\text{: Planck's constant}) \quad . \end{aligned}$$

The orientation of the quantization axis z of $\vec{I}$ is determined by the hyperfine interactions between nuclear momentum and applied polarizing magnetic field. The z-component of $\vec{I}$ is $m_I\hbar$ quantized corresponding to the magnetic quantum number $m_I = -I, (-I+1), ..., I$. The magnetic dipole moment is

$$\vec{\mu} = \gamma\vec{I} \quad \text{with} \quad |\vec{\mu}| = \gamma\sqrt{I(I+1)}\hbar \quad .$$

γ is the gyromagnetic ratio of the nucleus. For instance the gyromagnetic constant of a hydrogen proton has the value $\gamma_H = 42.6\text{MHz/T}$. Each value of m_I corresponds to a certain orientation of the nuclear spin. $2I + 1$ is the number of orientations. For a spin-$\frac{1}{2}$-nucleus with $I = \frac{1}{2}$ there are two possible spin orientations referring to the quantization axis:

$$\begin{aligned} m_I &= +\frac{1}{2} \quad \text{(state denoted as } \alpha \text{ or } \uparrow) \\ m_I &= -\frac{1}{2} \quad \text{(state denoted as } \beta \text{ or } \downarrow) \end{aligned}$$

The spin vector is located at a cone angle defined by $|\vec{I}|$ and I_z, I_x and I_y remaining undefined due to the uncertainty principle. The orientation of the

nuclear magnetic moment $\vec{\mu}$ is alike. The probabilities of a spin adopting α- or β-state obeys the Boltzmann equation. For example the nucleus might be a proton (proton magnetic resonance / ^{1}H-NMR). Considering a spin system in the absence of a magnetic field the net magnetization is zero.

Spin system in a static magnetic field

Applying an external static magnetic field

$$\vec{B}_0 = (0, 0, B_z)$$

only consisting of a z-component, energy changes of the α- and β-energy levels take place. The quantization axis for all spins is now the z-axis. The numbers of α- and β-spins differ causing a magnetization $\vec{M}$ parallel to the field. The z-component of the nuclear magnetic moment $\vec{\mu}$ is

$$\mu_z \;=\; \gamma I_z = \gamma \hbar m_I \quad.$$

The nuclear spin energy levels change to

$$E_{m_I} = -\vec{\mu} \cdot \vec{B} = -\gamma \hbar B_z m_I \quad.$$

These equally spaced levels are called Zeeman energies. The resulting energy separation of the two states α and β is

$$\Delta E = E_\beta - E_\alpha = \frac{1}{2}\gamma \hbar B_z - \left(-\frac{1}{2}\gamma \hbar\right) = \gamma \hbar B_z \quad.$$

According to the Planck Einstein equation $\Delta E = \hbar \omega$ it is reasonable to define a frequency

$$\omega_L = \frac{\Delta E}{\hbar} = \gamma B_z \quad.$$

The Larmor frequency ω_L determines the expectation values of the transverse components of nuclear spins corresponding to superpositions of α and β-state. The number of α spins exceeds the number of β spins slightly according to the Boltzmann distribution valid in thermal equilibrium

$$\frac{N_\beta}{N_\alpha} = \exp\{-\Delta E/k_B T\} = \exp\{-\gamma \hbar B_z/k_B T\} \quad. \tag{2.16}$$

With the spin density

$$\rho = \frac{N_\alpha - N_\beta}{V}$$

it results in a macroscopic magnetization parallel to $\vec{B}_0$:

$$M_z = \rho \langle \mu_z \rangle \vec{e}_z$$

Curie's law delivers with (2.16) and $N = N_\alpha + N_\beta$:

$$\Delta N = \frac{\rho \gamma^2 \hbar^2 I(I+1)}{3 k_B T}$$

Effect of an additional oscillatory field

If a circular polarized electromagnetic field in the xy-plane orthogonal to $\vec{B}_0$ with the radio frequency $\omega_{RF} = \omega_L$ is applied the resonance condition

$$\Delta E = \hbar \omega_{RF} = \gamma \hbar B_z$$

is satisfied and the energy of the photons matches the energy separation of the two states. Energy transfer comes into resonance with the radiation and strongly absorbing $\alpha \to \beta$ transitions take place. That means precessing spins experience the field $\vec{B}_1$ rotating with the frequency ω_{RF} as steady as they precess with the same frequency. Therefore they start to precess additionally around $\vec{B}_1$.
Hereby the magnetic field $\vec{B}_1$ rotates the magnetization $\vec{M}$ out of the z-orientation by an angle

$$\alpha = \gamma |\vec{B}_1| t_P$$

t_P is the duration of the HF pulse. If the duration of the pulse lets the spin vectors rotate into the xy-plane (90° pulse, $\frac{\pi}{2}$ pulse) the new expectation values of the xy-components M_x, M_y of the magnetization $\vec{M}$ might be detected by a coil located in the xy-plane by the induced alternating voltage. As the spin system is no more in thermal equilibrium it starts to relax towards it. Thus magnetization relaxes longitudinally by β-spins becoming α-spins again, the magnetization component M_z approaches its equilibrium value. The corresponding longitudinal relaxation time is called T_1. Further fanning out of the spin vectors due to different precession rates and inhomogenity of the field $\vec{B}_0$ caused by local magnetic fields induced by the movement of molecules lead to the disturbance of phase coherence and the expectations values of the magnetization components M_x and M_y decrease. The relaxation time T_2 refers to general transverse relaxation whereas T_2^* additionally includes the effect of the inhomogenity of $\vec{B}_0$. For a thin fluid $T_2 \approx T_1$ whereas a solid or a highly viscous fluid complies with $T_2 < T_1$. The decaying signal is denoted as a free induction decay (FID).

In the simplest case the relaxation of $\vec{M}$ proceeds corresponding to the following (Bloch) equation:

$$\frac{d\vec{M}}{dt} = \gamma \vec{M} \times \vec{B} - \frac{1}{T_1} \begin{pmatrix} 0 \\ 0 \\ M_z - |\vec{M}| \end{pmatrix} - \frac{1}{T_2} \begin{pmatrix} M_x \\ M_y \\ 0 \end{pmatrix}$$

The first term describes the precession of $\vec{M}$ around the net magnetic field $\vec{B} = \vec{B}_0 + \vec{B}_1$. The solution of the Bloch equation referring to the x', y', z'-coordinate system rotating with the frequency ω_L after a 90° pulse is:

$$M_{x'} = M_{x'}(t = 0) \exp\{-\frac{t}{T_2}\}$$

$$M_{y'} = M_{y'}(t = 0) \exp\{-\frac{t}{T_2}\}$$

$$M_{z'} = M_{z'}(t = 0) \left(1 - \exp\{-\frac{t}{T_1}\}\right)$$

2.3.2 Pulse Techniques in NMR

Free induction decay (FID) Applying a 90° pulse to a spin system in a static magnet field makes the spins rotate into the xy-plane. This makes it possible to detect different resonance frequencies (for instance if belonging to different kinds of molecules). The overall FID signal $S(t)$ consisting of signals with frequencies ω and intensities $I(\omega)$

$$S(t) = \int_{-\infty}^{+\infty} I(\omega) \exp\{\imath \omega t\} d\omega$$

delivers the harmonic components by Fourier transformation

$$I(\omega) = 2\Re \int_0^\infty S(t) \exp\{\imath \omega t\} dt$$

whereas

$$M_x \sim \Re\{S(t)\}$$
$$\text{and} \quad M_y \sim \Im\{S(t)\} \quad .$$

Spin echo Adding a 90° pulse to a field $\vec{B}_0$ rotates the spins into the xy-plane. As described in section 2.3.1 the phase coherence dwindles away continually (T_2^* relaxation). Setting then a 180° pulse the spins refocus with respect to the T_2 relaxation. In this way the reversible effect of $\vec{B}_0$ inhomogenities is eliminated and measurement of the relaxation time T_2 excluding inhomogenity effect is possible.

T$_1$ measurement   A 180° pulse inverts the magnetization due to a $\vec{B}_0$ field by 180°. Afterwards x- and y-component of $\vec{M}$ still are zero. Longitudinal relaxation proceeds till a 90° pulse is set. The following FID is recorded. By varying the duration between the first and the second pulse the relaxation time T_1 can be determined.

Magnetic field gradients   Overlaying a magnetic field gradient to the constant field $\vec{B}_0$ the total magnetic field and as a consequence thereof also the Larmor frequencies become dependant on the position:

$$\begin{aligned} \vec{B}(\vec{r}) &= \vec{B}_0 + \vec{G} \cdot \vec{r} \\ \omega_L(\vec{r}) &= \omega_0 + \gamma \vec{G} \cdot \vec{r} \end{aligned}$$

The phase shift entails the additional twist angle

$$\Delta\phi(\vec{r}, t) = \gamma \int_0^t \vec{G} \cdot \vec{r} d\tilde{t} = \vec{k} \cdot \vec{r} \quad .$$

The wave vector $\vec{k}$ refers to the reciprocal $\vec{k}$ space describing the integral

$$\vec{k} = \gamma \int_0^t \vec{G}(\tilde{t}) d\tilde{t} \quad .$$

Translational displacements $\vec{R}$ of spins might also cause a phase shift under certain circumstances (PGSE, narrow-pulse limit):

$$\Delta\phi(\vec{R}, t) = \gamma \int_0^t \vec{G} \cdot \vec{R} d\tilde{t} = 2\pi\vec{q} \cdot \vec{R}$$

$\vec{q}$ is the equivalent of $\vec{k}$.

PGSE / Imaging   Using magnetic field gradients makes it in general possible to analyze the 1D, 2D or 3D structure (magnetic resonance imaging – MRI) of a system as well as transport processes like flow or diffusion. The spatial encoding is made by frequency applying a magnetic field gradient during data acquisition and by phase inducing a phase shift by applying a field nonconstant in space. The slice selection is controlled by the bandwidth of applied frequencies of $\vec{B}_1$. The intensity of signal

$$S(\vec{k}) = \int\int\int \rho(\vec{r}) \exp\{\imath\vec{k} \cdot \vec{r}\} d\vec{r}$$

leads by inverse Fourier transformation to the spin density $\rho(\vec{r})$. Analogous the investigation of a moving system results from the signal

$$E(\vec{q}) = \int \int \int \bar{P}(\vec{R},t) \exp\{\imath \vec{q} \cdot \vec{R}\} d\vec{R} \quad .$$

$\bar{P}(\vec{R},t)$ is the so-called mean propagator declaring the mean probability of a particle experiencing a transitional displacement $\vec{R}$ during the time t. Coherent translations, e.g. flow, have an impact on the phasing of the signal, whereas noncoherent transport processes, e.g. diffusion, affect the amplitude. Therefore in experiment distinction is possible alike the differing between $\vec{k}$ and $\vec{q}$ space.

Chapter 3

Phenomenological Theory

We develop a new phenomenological theory in order to describe the effect of solid boundary walls in sheared suspensions. According to experimental results the presence of walls yields certain effects like structure formation and demixing processes leading to the formation of a depleted boundary layer along the wall and therewith pseudo wall slip (cp. section 2.1.2).

3.1 Approach

3.1.1 Modelling the Wall Effect

Starting Point

We start with an unidirectional creeping shear flow of a liquid containing monodispersely distributed spheres neglecting Brownian motion and inertia. Particle-particle interaction is assumed to be solely due to hydrodynamic forces. The fluid is assumed as newtonian. To make sure that our experimentally realized flows are creeping indeed we check the particle-related Reynolds number that describes the ratio of inertia and friction:

$$Re = \frac{\rho_F \dot{\gamma}(2a)^2}{\eta_0} \tag{3.1}$$

If $Re << 1$ flow is creeping.
The Péclet number represents a comparison between shear stresses and Brownian forces:

$$Pe = \frac{\eta_0 \dot{\gamma}(2a)^3}{k_B T}$$

If $Pe >> 1$ shear dominates and the Brownian motion can be left out.
The suspension is treated as a continuum and the concepts of continuum

mechanics apply. This is justified as in general the length scale of the macroscopical properties we are interested in is considerably bigger than the length scale of the particle size. More about the conditions suspensions have to meet to justify continuum mechanical description is explained e.g. by Ohl [32].

Idea

According to the analytical theory of Happel and Brenner [12] near the wall the resistance force differs from the usually assumed Stokes force. We presume that a particle very near the wall moving orthogonal to the wall experiences an increased resistance force in comparison to farther particles as the particle has to squeeze fluid out of the narrow gap between particle and wall or, alternatively, fluid has to be retracted into the gap. That means the resistance force $F_\perp$ acting on a single particle related to transverse movement is dependant from the distance to the wall y. (Shear flow is flowing parallel to the wall, obviously.) We suggest the following expression based on the Stokes force (2.10) provided with an additional factor $\left(\frac{a}{y}\right)$ that is the reciprocal wall distance made dimensionless with the particle radius:

$$F_\perp(y) = 6\pi a u_P \eta_0 \left(1 + \left(\frac{a}{y}\right)^m \right) \tag{3.2}$$

With decreasing distance to the wall the resistance force increases till infinity. For $y \to \infty$ it becomes the Stokes force.

Validation

Happel and Brenner [12] have determined theoretically forces on particles closeby a plane wall moving orthogonal to the wall and expressed the results with a series expansion.
If we choose the exponent m in (3.2) as 1 the values for $F_\perp$ agree with the values calculated from the series expansion of Happel and Brenner by Raasch [37] (fig. 3.1). Thus our proposed factor is appropriate (q.v. section A.1) and we can use it to include the wall influence into the diffusion model of Phillips et al. (section 3.1.2).
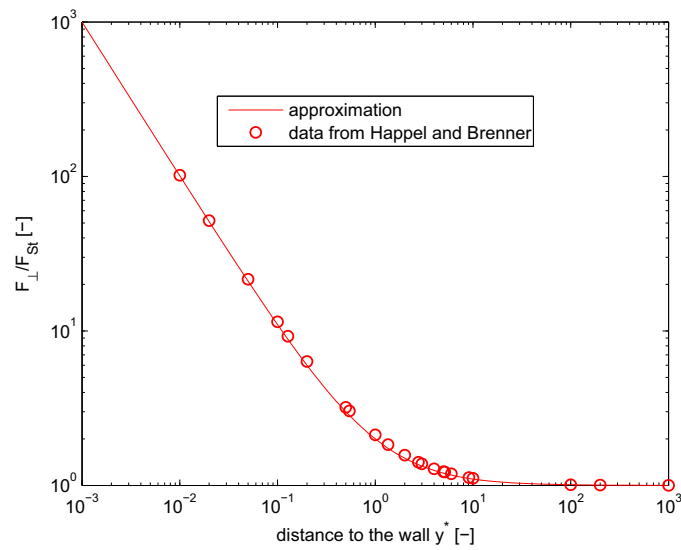
Figure 3.1: The approximation (3.2) describing the wall influence on the resistance force acting on particles moving perpendicular to the wall is in agreement with the theoretical data of Happel and Brenner [12].

Concentration Dependancy and Two Walls

Since we are concerned with suspensions the viscosity $\eta(\phi)$ is dependant on the particle concentration. We choose the suggestion of Krieger and Dougherty (2.3) and combine viscosity and wall influence factor $\left(\frac{a}{y}\right)$ to the new factor

$$\eta_0 \left(\frac{1}{(1 - \frac{\phi}{\phi_m})^2} + \left(\frac{a}{y}\right) \right)$$

that leads with (3.2) to the resistance force

$$F_\perp(y, \phi(y,t)) = 6\pi a u_P \eta_0 \left(\left(1 - \frac{\phi(y,t)}{\phi_m}\right)^{-2} + \left(\frac{a}{y}\right) \right) \quad . \qquad (3.3)$$

We neglect a further dependency on the particle distribution. In the presence of two walls with gap width h (Couette flow, fig. 2.2) the resistance force is increased by an additional term $\left(\frac{a}{h-y}\right)$ due to the second wall and it follows:

$$F_\perp(y, \phi(y,t)) = 6\pi a u_P \eta_0 \left(\left(1 - \frac{\phi(y,t)}{\phi_m}\right)^{-2} + \left(\frac{a}{y}\right) + \left(\frac{a}{h-y}\right) \right) \qquad (3.4)$$

This term is not valid if a particle is positioned directly at the wall ($y = 0$ or $y = h$) since at this position the van der Waals forces make the particle stick to the wall. Detaching would require forces beyond.

3.1.2 New Diffusion Equation

With (2.13) and the approximation (3.4) we set up a new diffusion equation including the wall influence:

$$\frac{\partial \phi(y,t)}{\partial t} \;=\; -\nabla \vec{N} \qquad (3.5)$$

$$\text{with}$$

$$\vec{N} \;=\; -k_f a^2 \phi \nabla(\phi \dot{\gamma}) - k_\eta a^2 \phi^2 \dot{\gamma} \frac{\nabla \left((1 - \frac{\phi}{\phi_m})^{-2} + \left(\frac{a}{y}\right) + \left(\frac{a}{h-y}\right) \right)}{\left((1 - \frac{\phi}{\phi_m})^{-2} + \left(\frac{a}{y}\right) + \left(\frac{a}{h-y}\right) \right)}$$

The particle flux due to gradient of resistance force is now a function of the wall distance.

At this point we introduce some new variables for simplification. The variables of length y and h are made nondimensional by relating them to the

particle radius and we define a concentration related to ϕ_m:

$y^* := y/a, \quad h^* := h/a, \quad \varphi(y,t) := \frac{\phi(y,t)}{\phi_m}$

With (3.5) we obtain for a plane Couette flow:

$$\frac{\partial \varphi(y^*,t)}{\partial t} = -\frac{\partial}{\partial y^*} \left(-k_f \phi_m \varphi \frac{\partial}{\partial y^*}(\varphi \dot{\gamma}) - k_\eta \phi_m \varphi^2 \dot{\gamma} \frac{\frac{\partial}{\partial y^*} \left((1-\varphi)^{-2} + y^{*-1} + (h^* - y^*)^{-1}\right)}{(1-\varphi)^{-2} + y^{*-1} + (h^* - y^*)^{-1}} \right)$$

(3.6)

Basing on (2.2) the shear rate of a plane Couette flow follows from a shear stress $\tau(t)$ and the viscosity $\eta(\phi)$ without wall dependance as flow is parallel to the walls:

$$\dot{\gamma}(t, \varphi(y^*,t)) = \frac{\tau(t)}{\eta_0}(1 - \varphi(y^*,t))^2$$

(3.7)

This is the shear rate of the fluid. There is also an influence of the wall onto the particle movement parallel to the wall making the velocity profile of the particle system differ from the velocity profile of the fluid. A comparison of the resulting particle concentration distribution and velocity profiles with and without taking into account such an effect of the wall on particle velocity parallel to the wall makes sure that this simplification is justified and we can assume the velocity profile of the particle system identical to the velocity profile of the fluid phase (cp. section A.2). With (3.7) and (3.6) we obtain:

$$\frac{\partial \varphi(y^*,t)}{\partial t} = -\frac{\tau(t)}{\eta_0} \frac{\partial}{\partial y^*}[-k_f \phi_m \varphi(y^*,t) \frac{\partial(\varphi(y^*,t)(1-\varphi(y^*,t))^2)}{\partial y^*}$$

$$-k_\eta \phi_m \varphi^2(y^*,t)(1-\varphi(y^*,t))^2 \frac{\frac{\partial}{\partial y^*} \left((1-\varphi(y^*,t))^{-2} + y^{*-1} + (h^* - y^*)^{-1}\right)}{(1-\varphi(y^*,t))^{-2} + y^{*-1} + (h^* - y^*)^{-1}}]$$

The solution of this partial differential equation considering appropriate initial and boundary conditions is the particle concentration $\varphi(y^*,t)$. It can not be solved analytically. The concentration profile as well as the gap width h^* scale with the particle radius. The time scale on the other hand depends on $\tau(t)$. Assuming $\tau(t) > 0$ we define a new time scale:

$$T = \frac{1}{\eta_0} \int_0^t \tau(\tilde{t})d\tilde{t}$$

$$\Leftrightarrow \quad \frac{\partial T}{\partial t} = \frac{\tau(t)}{\eta_0}$$

This leads to the modified particle concentration $\varphi_T(y^*,T)$ setting $\varphi_T(y^*,T) = \varphi(y^*,t)$:

$$\frac{\varphi_T(y^*,T)}{\partial T} = \frac{\partial \varphi(y^*,t)}{\partial t} \frac{\partial t}{\partial T}$$

$$= \frac{\partial \varphi(y^*,t)}{\partial t} \frac{\eta_0}{\tau(t)}$$

With (3.5) and still the shear rate $\dot{\gamma}(y^*, t)$ being valid it follows

$$\frac{\varphi_T(y^*, T)}{\partial T} = \frac{\eta_0}{\tau(t)}(-\nabla\vec{N})$$

and

$$\frac{\partial \varphi_T(y^*, T)}{\partial T} = -\frac{\partial}{\partial y^*}[-k_f \phi_m \varphi_T(y^*, T)\frac{\partial(\varphi_T(y^*, T)(1 - \varphi_T(y^*, T))^2)}{\partial y^*}$$

$$-k_\eta \phi_m \varphi_T^2(y^*, T)(1 - \varphi_T(y^*, T))^2 \frac{\frac{\partial}{\partial y^*}((1 - \varphi_T(y^*, T))^2 + y^{*-1} + (h^* - y^*)^{-1})}{(1 - \varphi_T(y^*, T))^{-2} + y^{*-1} + (h^* - y^*)^{-1}}]$$

This equation shows that the particle distribution is associated with the total macroscopical shear strain function. During shear experiment at a certain local shear strain always the same particle concentration $\varphi_T(y^*, T)$ occurs independently from the course of the experiment $\tau(t)$ at a fixed initial particle concentration. The modified time scale is determined by the shear stress function $\tau(t)$ respectively the shear strain $\gamma(t)$ as to any shear stress function $\tau(t)$ a shear strain function $\gamma(t)$ corresponds. The modified shear rate $\dot{\gamma}_T(y^*, T)$ follows from $\gamma_T(y^*, T) = \gamma(y^*, t)$:

$$\dot{\gamma}_T(y^*, T) := \frac{\partial \gamma_T(y^*, T)}{\partial T} = \frac{\partial \gamma(y^*, t)}{\partial t}\frac{\partial t}{\partial T}$$

$$= \frac{1}{\eta_r(\varphi)}$$

(η_r is the relative viscosity $\eta_r := \eta/\eta_0$.) Hence also the shear rate referring to the new time scale is not a function of $\tau(t)$ but of the particle distribution only.

3.1.3 Gravity Effect

If there is a density difference between the fluid and the disperse phase meaning $\rho_F - \rho_P \neq 0$ the gravity effect may influence the particle drift since the particles then go up or down due to sedimentation or buoyancy respectively. In the following we assume that the gravity direction is transverse to flow direction (that is y direction) and parallel to the shear-induced particle drift. The lift force due to gravity acceleration in case of buoyancy

$$F_A = \rho_F g \frac{4}{3}\pi a^3$$

balances with the mass force

$$F_G = -\rho_P g \frac{4}{3}\pi a^3$$
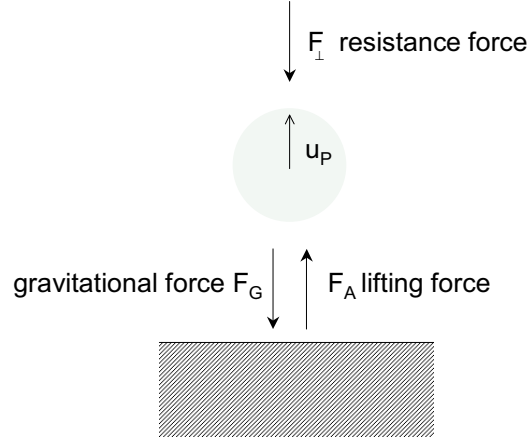
Figure 3.2: The force balance of a particle in a fluid moving transverse to a wall below

and the resistance force $F_\perp(y^*, \varphi(y^*, t))$ (equation (3.2)) (fig. 3.2). The particle velocity results from the force balance:

$$\sum F = 0$$
$$0 = F_\perp(y^*, \varphi(y^*, t)) + F_G + F_A$$
$$0 = -6\pi\eta_0((1 - \varphi(y^*, t))^{-2} + y^{*-1} + (h^* - y^*)^{-1})au_P - \rho_P g\frac{4}{3}\pi a^3 + \rho_F g\frac{4}{3}\pi a^3$$
$$0 = -6\pi\eta_0((1 - \varphi(y^*, t))^{-2} + y^{*-1} + (h^* - y^*)^{-1})au_P + (\rho_F - \rho_P)g\frac{4}{3}\pi a^3$$
$$\Rightarrow u_p(y^*, \varphi(y^*, t)) = \frac{2(\rho_F - \rho_P)ga^2}{9\eta_0}((1 - \varphi(y^*, t))^{-2} + y^{*-1} + (h^* - y^*)^{-1})^{-1} \qquad (3.8)$$

In case of the unmodified Stokes force acting the Stokes velocity would be the result:

$$u_{St} = \frac{2(\rho_F - \rho_P)ga^2}{9\eta_0} \qquad (3.9)$$

The particle flux due to gravity

$$
\begin{aligned}
N_g(y^*, \varphi(y^*,t)) &= u_P(y^*, \varphi(y^*,t))\phi(y^*,t) \\
&= \frac{2}{9}a^2(\rho_F - \rho_P)g\eta_0^{-1}((1 - \varphi(y^*,t))^{-2} + y^{*-1} + (h^* - y^*)^{-1})^{-1}\phi(y^*,t)
\end{aligned}
$$

is added to the total particle flux

$$
\begin{aligned}
N &= N_f + N_\eta + N_g \\
&= -k_f a\phi_m^2\varphi\frac{\partial}{\partial y^*}(\varphi\dot\gamma) - k_\eta a\phi_m^2\varphi^2\dot\gamma\frac{\frac{\partial}{\partial y^*}\left((1-\varphi)^{-2} + y^{*-1}\right)}{((1-\varphi)^{-2} + y^{*-1})} \\
&\quad + \frac{2}{9}a^2(\rho_F - \rho_P)g\eta_0^{-1}((1 - \varphi(y^*,t))^{-2} + y^{*-1} + (h^* - y^*)^{-1})^{-1}\phi
\end{aligned}
$$

$$(3.10)$$

and leads with (3.6) to the following diffusion equation:

$$
\begin{aligned}
\frac{\partial\varphi}{\partial t} &= -\frac{\partial}{\partial y^*}[-k_f\phi_m\varphi\frac{\partial}{\partial y^*}(\varphi\dot\gamma) - k_\eta\phi_m\varphi^2\dot\gamma\frac{\frac{\partial}{\partial y^*}((1-\varphi)^{-2} + y^{*-1} + (h^* - y^*)^{-1})}{(1-\varphi)^{-2} + y^{*-1} + (h^* - y^*)^{-1}} \\
&\quad + \frac{2}{9}a(\rho_F - \rho_P)g\eta_0^{-1}((1 - \varphi)^{-2} + y^{*-1} + (h^* - y^*)^{-1})^{-1}\varphi]
\end{aligned}
$$

$$(3.11)$$

(Here and further we use φ instead of $\varphi(y^*,t)$ for the sake of easier readability of long formulas.)

Again we obtain a nonlinear partial differential equation. A possible initial condition may be $\varphi(y^*, t = 0s) = const = \langle\varphi\rangle$ (homogenity). A possible boundary condition may be $N(y^* = 0, t) = 0$ (if two walls present $N(y^* = h^*, t) = 0$ additionally). Alternatively $\frac{1}{h^*}\int_0^{h^*}\varphi(y^*,t)d\tilde y^* = \langle\varphi\rangle \ \forall \ t$ may be demanded.

At steady state

$$\frac{\partial\varphi(y^*,t)}{\partial t} = 0$$

and thus (cp. equation (3.6))

$$\frac{\partial N}{\partial y^*} = 0 \quad \text{and} \quad N = const \quad .$$

Due to physical reasons the particle flux at a wall flanking the flow has to be zero and the following boundary condition is valid:

$$N(y^* = \text{wall position}) = 0 \tag{3.12}$$

The problem (3.11) is quasi-linear and parabolic. It cannot be solved analytically. The numerical treatment of this kind of partial differential equation

is problematic as the equation degenerates at $\varphi = 0$ and $\varphi = 1$ the second derivative becoming zero causing extreme instabilities. It did not lead to success here. Also an immensely complicated calculation of perturbations delivered no usable result. So no general solution of the problem will be presented here.

In the following chapter however special cases of sheared and non-sheared suspensions with and without wall influence as well as gravity effects are investigated basing upon the general diffusion equation (3.11).

3.2 Shear-Flowing and Non-Flowing Suspensions under Wall Influence

Generally the diffusion equation (3.11) determines the properties of shear-flowing suspensions including wall influence and gravity directed orthogonal to the flow direction and to the wall(s).

3.2.1 Shear Flow without Gravity Effect

We consider a shear flow without gravitation effects. Thus particle transport is induced solely by hydrodynamic interactions. The corresponding diffusion equation basing on (3.11) is

$$
\begin{aligned}
\frac{\partial \varphi(y^*, t)}{\partial t} &= -\frac{\partial (N_f + N_\eta)}{\partial y^*} \\
&= -\frac{\partial}{\partial y^*}\left[-k_f \phi_m \varphi \frac{\partial}{\partial y^*}(\varphi \dot\gamma) - k_\eta \phi_m \varphi^2 \dot\gamma \frac{\frac{\partial}{\partial y^*}\left((1-\varphi)^{-2} + y^{*-1} + (h^* - y^*)^{-1}\right)}{(1-\varphi)^{-2} + y^{*-1} + (h^* - y^*)^{-1}} \right]
\end{aligned}
$$
(3.13)

According to (2.8) and (2.9) the particle flux is

$$
N = 0 = k_f a \phi_m^2 \varphi \frac{\partial}{\partial y^*}(\varphi \dot\gamma) + k_\eta a \phi_m^2 \varphi^2 \dot\gamma \frac{1}{F_\perp} \frac{\partial F_\perp}{\partial y^*}
$$

which, after some rearrangements, leads to

$$
0 = k_f \frac{\partial}{\partial y^*} \ln(\varphi \dot\gamma) + k_\eta \frac{\partial \ln\left(\frac{F_\perp}{6\pi a u_P \eta_0}\right)}{\partial y^*} \quad .
$$

Integration produces

$$
\begin{aligned}
C &= k_f \ln(\varphi\dot\gamma) + k_\eta \ln \frac{F_\perp}{6\pi au_P\eta_0} \\
\Longleftrightarrow \quad e^{C/k_f} &= \varphi\dot\gamma \left(\frac{F_\perp}{6\pi au_P\eta_0} \right)^{k_\eta/k_f}
\end{aligned}
\tag{3.14}
$$

C being the integration constant.

No wall influence

Generally at steady state the mathematical description of a shear flow without walls is equivalent to that of a system with walls but without wall influence. The boundary condition is different. It refers either to the wall position or to the positional coordinate y^* approaching infinity.
The steady state of a shear flow without wall influence follows from (3.14) with

$$
F_\perp(\varphi) = 6\pi au_P\eta_0(1-\varphi)^{-2}
$$

basing on (2.10), (2.3) and (2.2). The shear stress at steady state is called τ_0. This leads to

$$
e^{\frac{C}{k_f}} = \frac{\tau_0}{\eta_0}\varphi(1-\varphi)^{2(1-\frac{k_\eta}{k_f})}
$$

with the only solution $\varphi(y^*) = const$. Therefore steady state is a homogenous suspension whereas the integration constant C is determined by the average particle concentration $\langle\varphi\rangle$.

One wall present

If we consider the case of a half-infinite shear flow with only one wall present at the position $y^* = 0$ a further boundary condition can be set up as $\varphi(y^* \to \infty) = \varphi_\infty$ at steady state determining the integration constant C with (3.14), (3.7) and (3.3):

$$
\begin{aligned}
F_\perp(\varphi = \varphi_\infty, y^* \to \infty) &= 6\pi au_P\eta_0(1-\varphi_\infty)^{-2} \\
\text{and} \quad e^{C/k_f} &= \varphi_\infty\frac{\tau_0}{\eta_0}(1-\varphi_\infty)^{2(1-k_\eta/k_f)}
\end{aligned}
$$

With (3.14), (3.7) and (3.3) follows:

$$
\begin{aligned}
F_\perp(\varphi, y^*) &= 6\pi a u_P \eta_0 (y^{*-1} + (1-\varphi_\infty)^{-2}) \\
\text{and} \qquad \varphi(1-\varphi)^2 \left(y^{*-1} + (1-\varphi)^{-2}\right)^{\frac{k_\eta}{k_f}} &= \varphi_\infty (1-\varphi_\infty)^{2(1-\frac{k_\eta}{k_f})}
\end{aligned}
$$
$$(3.15)$$

$$
\iff \quad y^* = \frac{\varphi^{\frac{k_f}{k_\eta}}(1-\varphi)^{2\frac{k_f}{k_\eta}}}{\varphi_\infty^{\frac{k_f}{k_\eta}}(1-\varphi_\infty)^{2\left(\frac{k_f}{k_\eta}-1\right)} - \varphi^{\frac{k_f}{k_\eta}}(1-\varphi)^{2\left(\frac{k_f}{k_\eta}-1\right)}} \qquad (3.16)
$$

The parameter φ_∞ is the particle concentration at infinite distance from the wall and therefore determines the average particle concentration. According to Phillips et al. [33] $k := \frac{k_f}{k_\eta}$ takes a value of approximately 0.66 (this value refers to a system with an average particle concentration $\langle \phi \rangle = 0.55$, there is no dependance from particle size or fluid viscosity according to dimensional analysis) (cp. section B.1). $k = 0.66$ will be used in all our calculations. Equation (3.16) determines the stationary particle concentration profile in a semi-finite shear flow without gravity effect including wall influence with one wall present. The shear rate profile follows from the concentration dependant viscosity (3.7). Further on the velocities $u(y^*)$ theoretically can be obtained by integration of the shear rate according to (2.1):

$$
u(y^*) = \int_0^{y^*} \dot{\gamma}(\tilde{y}^*) d\tilde{y}^* \qquad (3.17)
$$

The integration constant results from the no slip condition at the wall $u(y^* = 0) = 0$ that is assumed. In this case the function $\dot{\gamma}(y^*)$ is not available in an analytical form so the single velocity values are determined from discrete data triples $(\varphi(y^*), y^*, \dot{\gamma}(\varphi(y^*)))$ (cp. section B.2). Fig. 3.3 shows the resulting particle concentration profiles, shear rate profiles and velocity profiles at various boundary concentrations φ_∞. (The behavior very near the wall is to be seen more clearly in fig. 3.5.) The shear rate and the velocity are made non-dimensional according to:

$$
\begin{aligned}
\dot{\gamma}^* &= \dot{\gamma}\frac{\eta_0}{\tau_0} \\
u^* &= u\frac{\eta_0}{\tau_0}
\end{aligned}
$$

The concentration increases monotonously with increasing distance from the wall approaching φ_∞ at $y^* \to \infty$ at an infinite distance from the wall. Unlike shear rate and velocity the concentration field is not dependant from τ_0/η_0. At the wall there is a depletion of particles. The low particle concentration
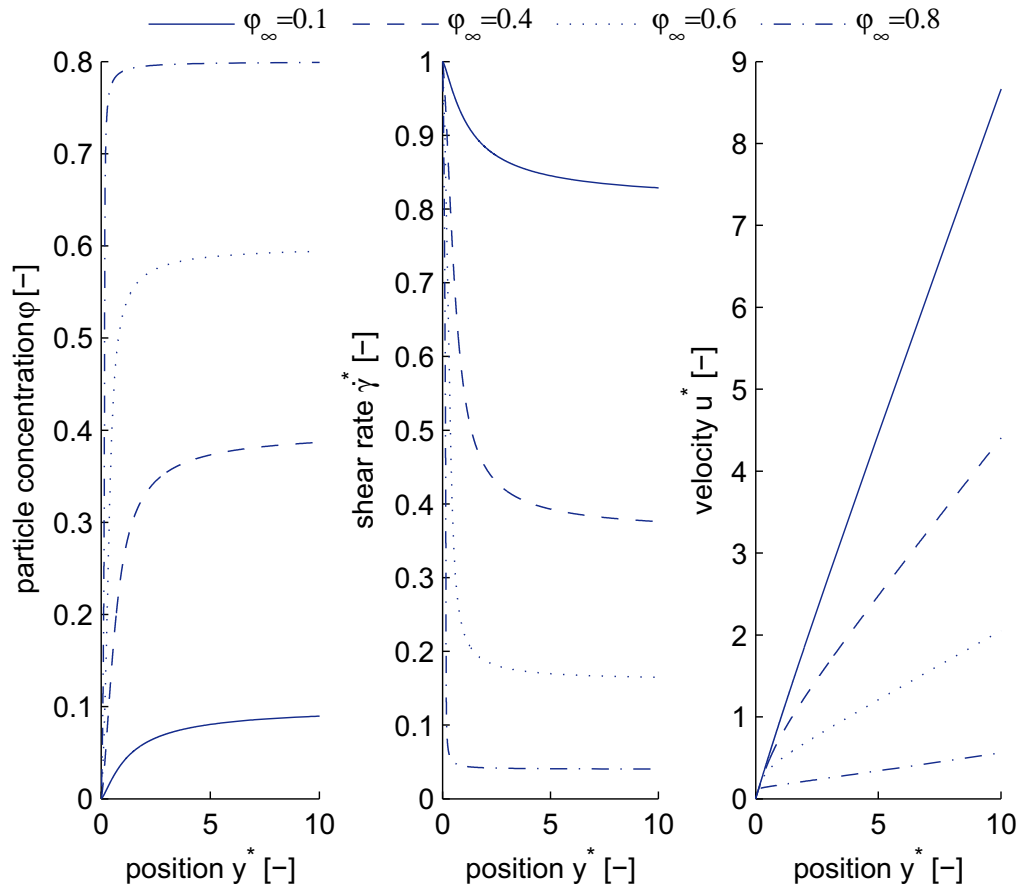
Figure 3.3: Particle concentration, shear rate and velocity profiles in a steady half-infinite shear flow (one wall) without gravity effect at various average particle concentrations

within the boundary layer implicates a low viscosity (equation (2.3)) and high shear rates. This leads to a steep velocity profile in this area leading to the phenomenon of pseudo wall slip (cp 2.1.2).

Very close to the wall If $y^* \to 0$ the leading term in the resistance force is

$$F_\perp(y^*) = 6\pi a u_P \eta_0 y^{*-1}$$

and with (3.14) and (3.7) it results

$$\varphi(1-\varphi)^2\left(y^{*-1}\right)^{1/k} = \varphi_\infty(1-\varphi_\infty)^{2(1-1/k)}$$
$$\Leftrightarrow \varphi \propto y^{*1/k}$$

meaning that the particle concentration near the wall is proportional to a power of the wall distance. With $k = 0.66$ it follows:

$$\varphi \propto y^{*-0.66}$$

The behaviour of $\varphi(y^* \to 0)$ becomes apparent in fig. 3.5.

Boundary layer   If we define a boundary layer thickness $\delta_{90}^* = \delta_{90}/a$ as the position y^* at which the particle concentration is 90% of φ_∞

$$\delta_{90}^* := y^*(\varphi(y^*) = 0.9 * \varphi_\infty) \qquad (3.18)$$

it follows with (3.16)

$$\delta_{90}^* = \frac{(0.9\varphi_\infty)^k(1-0.9\varphi_\infty)^{2k}}{\varphi_\infty^k(1-\varphi_\infty)^{2(k-1)} - \varphi^k(1-\varphi)^{2(k-1)}} \qquad . \qquad (3.19)$$

 The resulting boundary layer (fig. 3.4) is only a few particle radii thin. With decreasing total concentration φ_∞ the layer becomes wider.
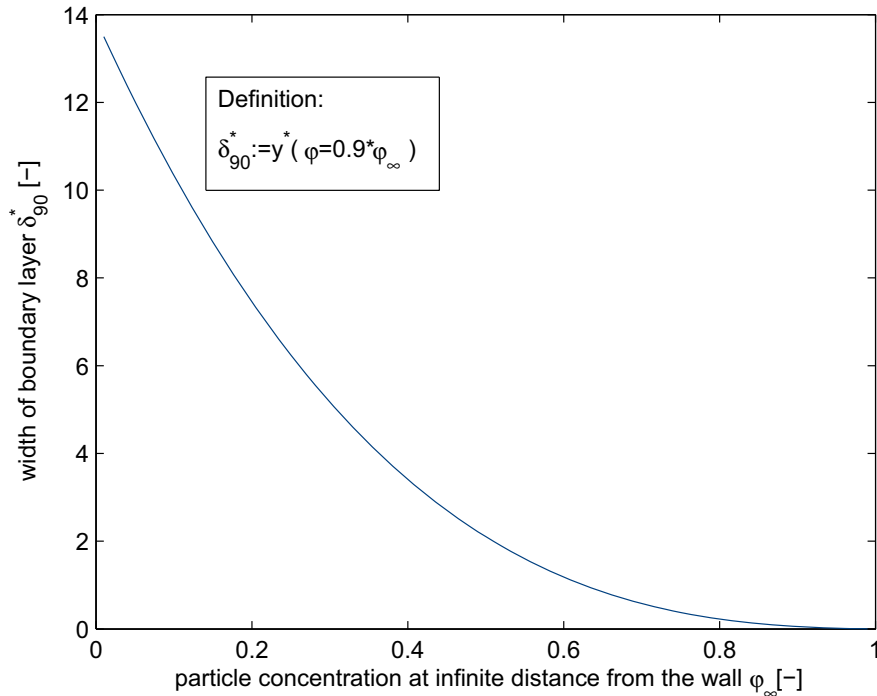
Figure 3.4: The width of the boundary layer is a function of the particle concentration at infinite distance from the wall.

Discontinuities   If we look closer at the concentration profiles at high mean concentrations we realize that the analytical solution is no injective function. At some positions more than one particle concentration is formally valid. Physically this cannot be realized. The solution is mathematical and gives the theoretical particle distribution resulting from equation (3.16). A possible explanation might be the existence of a discontinuity within the area of non-injectivity meaning concretely a step of the particle concentration. The new non-ambiguous concentration profile is another valid and physically possible solution satisfying equation (3.16) (fig. 3.5).
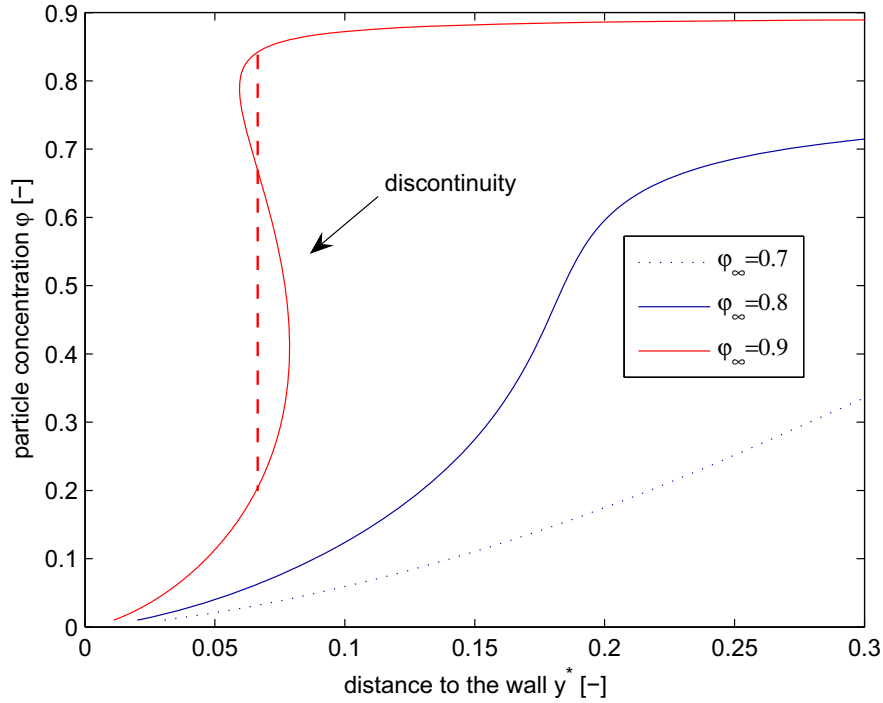
Figure 3.5: The mathematically obtained particle concentration profiles in steady half-infinite shear flow correspond to a discontinuity of the physically realized particle concentration function.

The exact location of the discontinuity respectively the phase boundary is not defined within our model. This result seems questionable as the discontinuity is positioned less than one single particle radius near the wall. This makes the macroscopic interpretation problematic. A statistical interpretation taking the particle concentrations as probabilities and the profile as a probability function is meaningless due to the geometric structuring of the particle distribution induced by the wall.

Two walls present

Considering the steady state of a Couette flow (cp. fig. 2.2) including two walls with (3.14), (3.4) and (3.7) follows:

$$
\begin{aligned}
F_\perp(\varphi, y^*) &= 6\pi a u_P \eta_0 ((1-\varphi)^{-2} + y^{*-1} + (h^* - y^*)^{-1}) && (3.20) \\
\text{and} \quad e^{C/k_f} &= \varphi \frac{\tau_0}{\eta_0}(1-\varphi)^2((1-\varphi)^{-2} + y^{*-1} + (h^* - y^*)^{-1})^{1/k} && (3.21)
\end{aligned}
$$

As for the boundary condition we set the particle concentration at the center of the gap $\varphi(y^* = h^*/2) = \varphi_0$ and obtain

$$
e^{C/k_f} = \varphi_0 \frac{\tau_0}{\eta_0}(1-\varphi_0)^2((1-\varphi_0)^{-2} + h^{*-1})^{1/k}
$$

leading with (3.21) to:

$$
\varphi(1-\varphi)^2 \left(y^{*-1} + (h^* - y^*)^{-1} + (1-\varphi)^{-2} \right)^{1/k} = \varphi_0(1-\varphi_0)^2((1-\varphi_0)^{-2} + h^{*-1})^{1/k}
$$

$$
\leftrightarrow \quad 0 = y^{*2} - h^* y^* + h^*((\varphi^{-1}(1-\varphi^{-2})\varphi_0(1-\varphi_0)^2)^k((1-\varphi_0)^{-2} + h^{*-1}) - (1-\varphi)^{-2})^{-1}
$$

Theoretically the particle concentration profiles can be determined through this equation. Here they were obtained instead by the numerical solution of the differential equation (3.14) with (3.20) and (3.7) employing a variable order multistep solver using backward differentiation formulas suitable for stiff problems. As described before the shear rate and velocity profiles follow from the concentration profiles.

Fig. 3.6 shows the results for a Couette flow with gap width $h^* = 30$. The particles tend to drift away from the walls and here also at the walls the pseudo wall slip is recognizable.

Figure 3.6: Particle concentration, shear rate and velocity profiles in a steady Couette flow without gravity effect at various average particle concentrations at $h^* = 30$

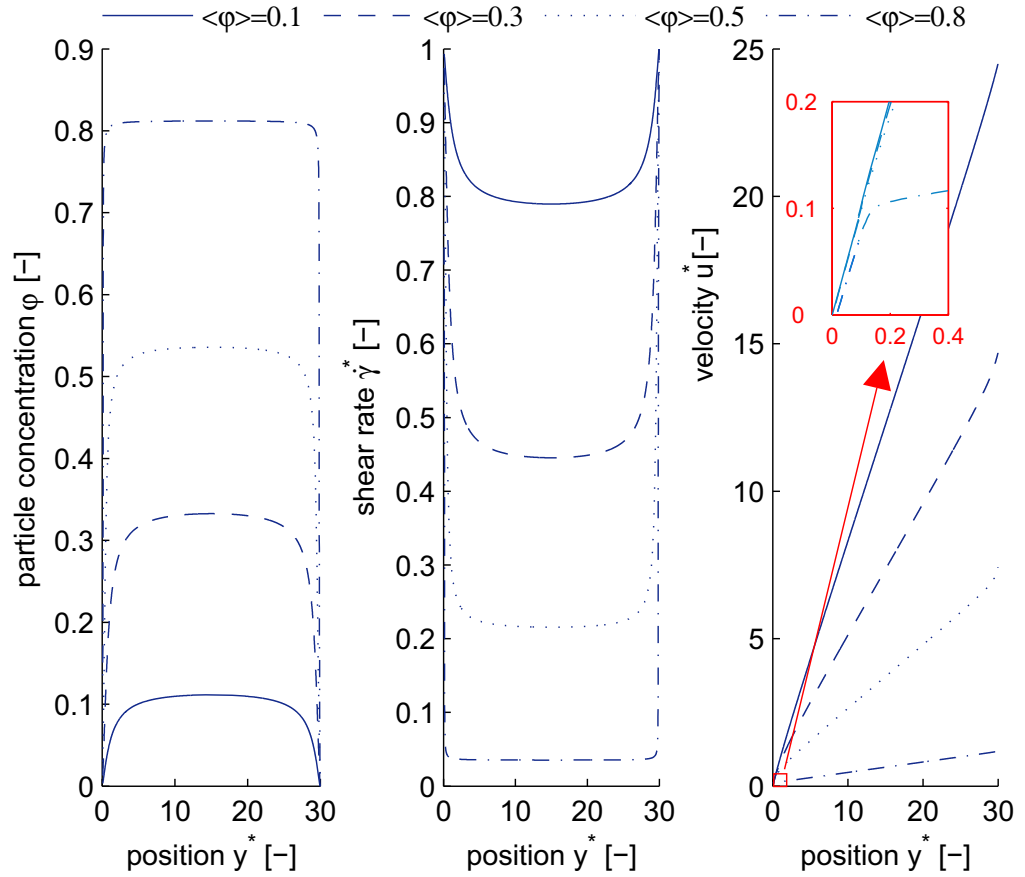### 3.2.2 Shear Flow with Gravity Effect

In a shear flow with gravitation particle drift is induced by hydrodynamic diffusion as well as gravity.

One wall present

The equation to be solved in order to obtain the instationary particle concentration distribution of semi-finite shear flow with gravity is the general diffusion equation (3.11) limiting the wall influence to only one wall:

$$
\begin{aligned}
\frac{\partial \varphi(y^*, t)}{\partial t} &= -\frac{\partial}{\partial y^*}[-k_f \phi_m \varphi \frac{\partial}{\partial y^*}(\varphi \dot{\gamma}) - k_\eta \phi_m \varphi^2 \dot{\gamma} \frac{\frac{\partial}{\partial y^*}((1-\varphi)^{-2} + y^{*-1})}{(1-\varphi)^{-2} + y^{*-1}} \\
&\quad + \frac{2}{9} a(\rho_F - \rho_P)g\eta_0^{-1}((1 - \varphi(y^*, t))^{-2} + y^{*-1})^{-1}\varphi] \qquad (3.22)
\end{aligned}
$$

At steady state with $\frac{\partial}{\partial t} = 0$ the particle concentration distribution in shear flow of a suspension along a wall including gravity effect follows from (3.22) with the boundary condition at the wall $N(y^* = 0) = 0$:

$$
\begin{aligned}
N = 0 &= -k_f a\phi_m^2 \varphi \frac{\partial}{\partial y^*}(\varphi \dot{\gamma}) - k_\eta a \phi_m^2 \varphi^2 \dot{\gamma} \frac{\frac{\partial}{\partial y^*}((1-\varphi)^{-2} + y^{*-1})}{(1-\varphi)^{-2} + (y^{*-1})} \\
&\quad + \frac{2}{9} a^2 \phi_m (\rho_F - \rho_P)g\eta_0^{-1}((1 - \varphi(y^*, t))^{-2} + y^{*-1})\varphi \qquad (3.23)
\end{aligned}
$$

from which we get:

$$
\frac{d\varphi}{dy^*} = \frac{-\varphi(1-\varphi)^2 y^{*-2} + \frac{2}{9}\frac{ag}{\phi_m \tau_0 k_\eta}(\rho_F - \rho_P)}{-k((1-\varphi)^{-2} + y^{*-1})((1-\varphi)^2 - 2\varphi(1-\varphi)) - 2\varphi(1-\varphi)^{-1}}
$$

This is an ordinary nonlinear differential equation of first order. It cannot be solved analytically but a numerical solution is possible. Fig. 3.7 shows the resulting particle concentration profiles, shear rate profiles and velocity profiles if particle flux due to gravity is directed away from the wall ($\rho_F - \rho_P > 0$) with $\frac{ag(\rho_F - \rho_P)}{\phi_m \tau_0 k_\eta} = 0.1$ at various fluid contents. Δy_F^* denotes the layer width of pure fluid ($\varphi = 0$) if $\varphi = 1$ elsewhere. For examplification we imagine a system consisting of a layer of pure fluid of width Δy_F^* between a wall and a half-infinite expanded particle ensemble with $\varphi = 1$. Hydrodynamic diffusion during shearing generates a transition zone between $\varphi = 0$ and $\varphi = 1$ at equilibrium. The velocity profile clearly shows the occurrence of pseudo wall slip. Fig. 3.8 refers to gravity driving the particles towards the wall ($\rho_F - \rho_P < 0$) with $\frac{ag(\rho_F - \rho_P)}{\phi_m \tau_0 k_\eta} = -0.1$ at various particle contents.
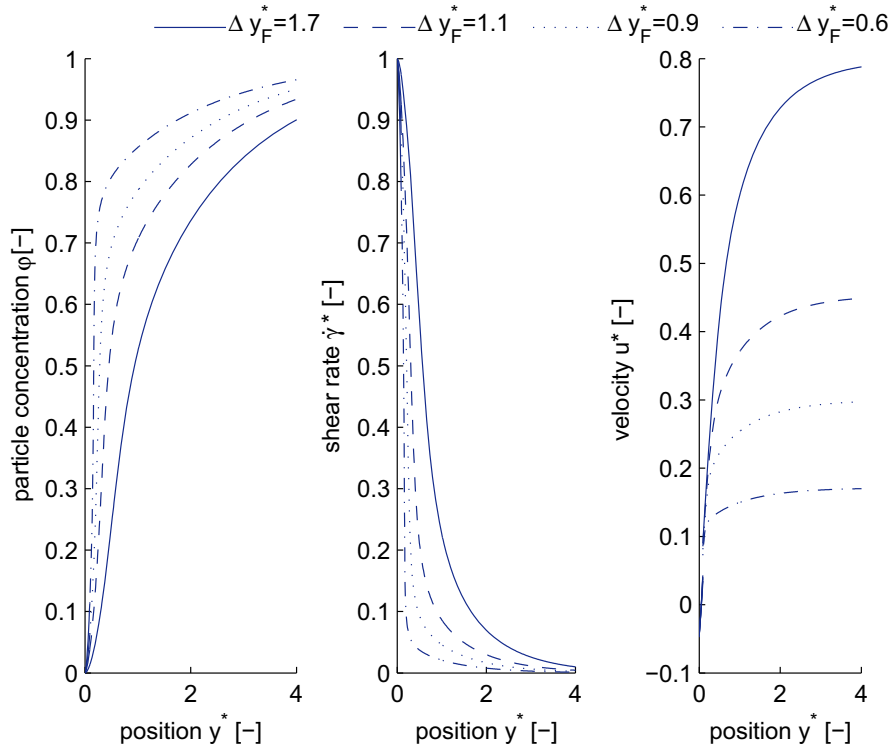
Figure 3.7: Particle concentration, shear rate and velocity profiles in a steady half-infinite shear flow with gravity flux directed away from the wall at $\frac{ag(\rho_F - \rho_P)}{\phi_m \tau_0 k_\eta} = 0.1$ and various fluid contents

Δy_P^* is the layer width with $\varphi = 1$ of the system if $\varphi = 0$ elsewhere. Wall influence is responsible for reaching $\varphi = 0$ at the wall whereas the gradually changing particle concentration at steady state is governed by the equilibrium of particle fluxes due to hydrodynamic diffusion and gravity. In this case a negative wall slip occurs.
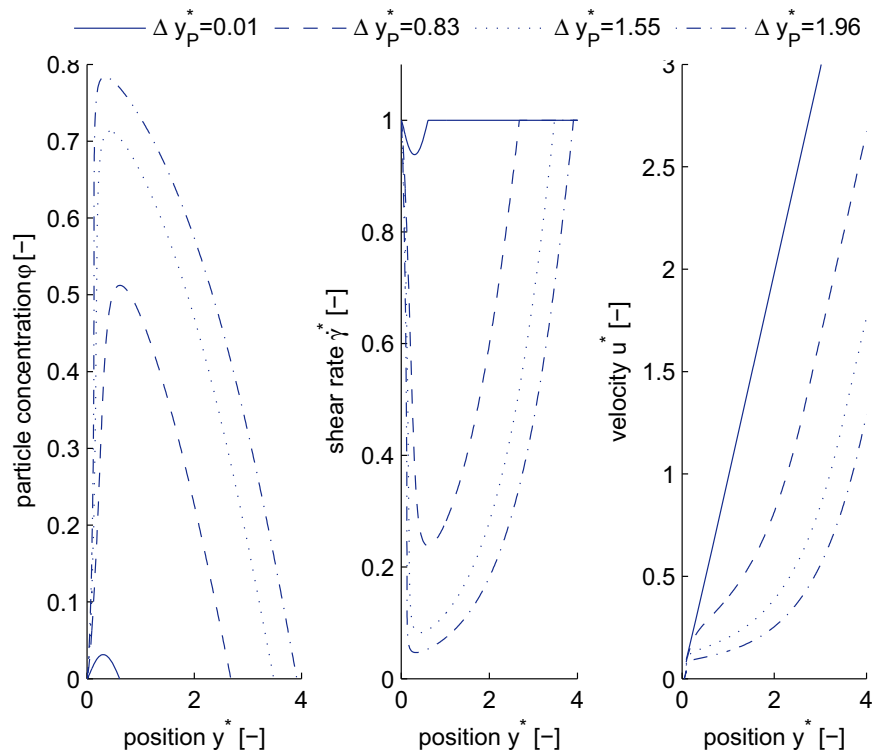
Figure 3.8: Particle concentration, shear rate and velocity profiles in a steady half-infinite shear flow with gravity flux directed towards the wall at $\frac{ag(\rho_F - \rho_P)}{\phi_m \tau_0 k_\eta} = -0.1$ and various particle contents

Two walls

The instationary particle concentration of a Couette flow with gravitation is described by equation (3.11) and cannot be solved as explained in section 3.1.2. At steady state it is $N = 0$ and $\frac{\partial}{\partial t} = 0$ leading to:

$$
\begin{aligned}
0 &= -k_f a \phi_m^2 \varphi \frac{\partial}{\partial y^*}(\varphi \dot{\gamma}) - k_\eta a \phi_m^2 \varphi^2 \dot{\gamma} \frac{\frac{\partial}{\partial y^*}\left((1-\varphi)^{-2} + y^{*-1}\right)}{(1-\varphi)^{-2} + y^{*-1}} \\
&\quad + \frac{2}{9} g a^2 \phi_m (\rho_F - \rho_P) g \eta_0^{-1}\left((1-\varphi(y^*,t))^{-2} + y^{*-1} + (h^* - y^*)^{-1}\right)\varphi
\end{aligned}
$$

and

$$
\frac{\partial \varphi}{\partial y^*} = \frac{-\varphi(1-\varphi)^2(y^{*-2} - (h^* - y^*)^{-2}) - \frac{2}{9}\frac{(\rho_F - \rho_P)g}{\phi_m \tau_0 k_\eta}(1-\varphi)}{-k((1-\varphi)^{-2} + y^{*-1} + (h^* - y^*)^{-1})((1-\varphi)^2 - 2\varphi(1-\varphi)) - 2\varphi(1-\varphi)^{-1}}
$$

In order to obtain the concentration profiles the differential equation was solved numerically. The particle concentration profiles, shear rate profiles and velocity profiles with $h^* = 30$ and $\frac{2}{9}\frac{(\rho_F - \rho_P)ag}{\phi_m \tau_0 k_\eta} = -1$ are shown in fig. 3.9 at different average concentrations. Fig. 3.10 shows the profiles with $h^* = 30$, $\langle \varphi \rangle = 0.3$ and $\frac{ag}{\phi_m \tau_0 k_\eta} = 1\text{m}^3/\text{kg}$ varying $(\rho_F - \rho_P)$. The particles have gone towards one wall (depending on the direction of gravity) but not reached the wall totally because of the wall influence. Again, the transition between pure liquid and particle-laden area is determined by the equilibrium of particle fluxes.
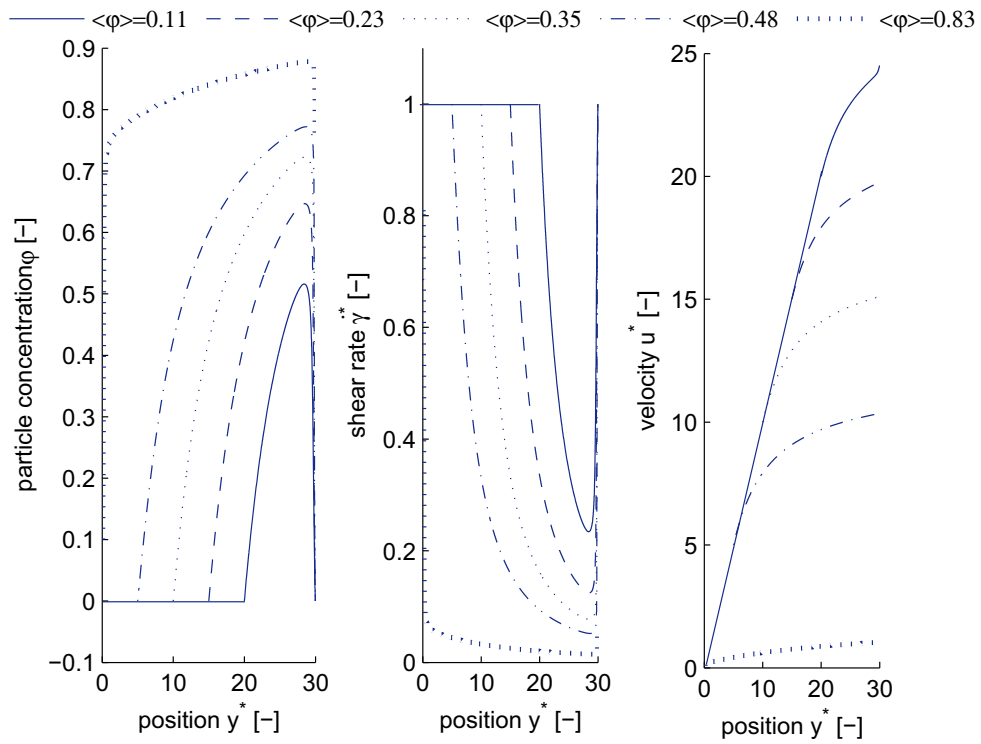
Figure 3.9: Particle concentration, shear rate and velocity profiles in a steady Couette flow, gap width $h^* = 30$, including gravity effect at $\frac{2}{9} \frac{ag(\rho_F - \rho_P)}{\phi_m \tau_0 k_\eta} = 1$ and various average particle concentrations
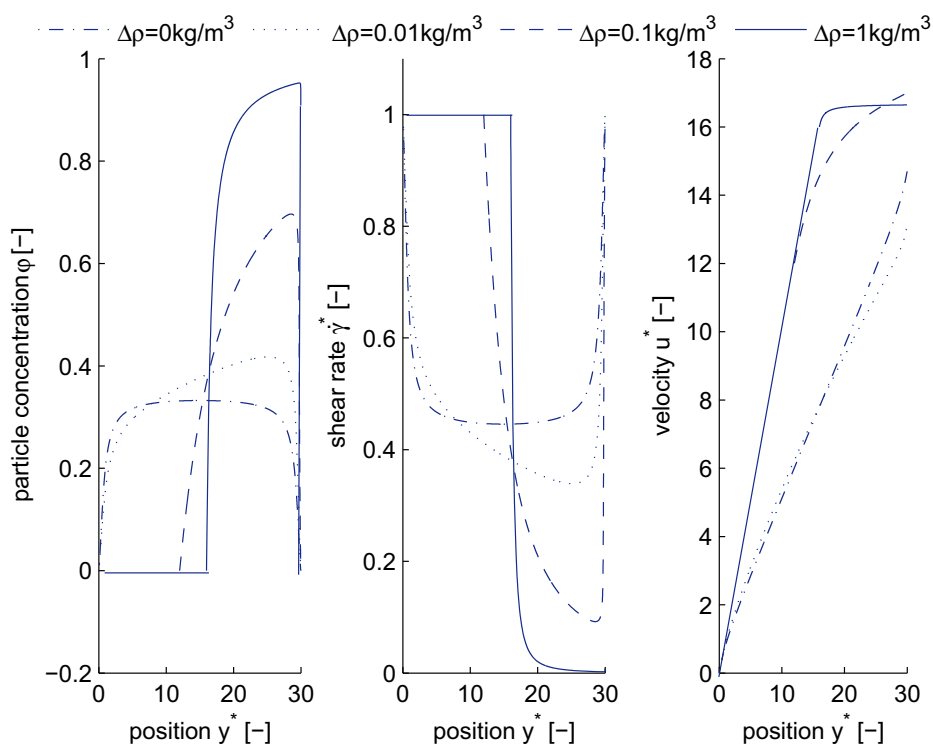
Figure 3.10: Particle concentration, shear rate and velocity profiles in steady Couette flow, gap width $h^* = 30$, including gravity effect at $\frac{2}{9}\frac{ag}{\phi_m \tau_0 k_\eta} = 1 m^3/kg$, $\langle \varphi \rangle = 0.3$ and various density differences

3.2.3 Time Dependant Gravity Effect, no Flow

In a non-flowing suspension the particles go up if particle density is lower than fluid density (buoyancy) or down if particle density is higher than fluid density (sedimentation). Particle transport is only due to gravity.

One wall present

Particle flux directed away from the wall We consider a diluted suspension with gravity-induced particle movements directed away from a single wall. That could be a suspension above a wall with particles going up or sedimentation in a suspension under a wall. Such according to (3.8) the velocity of a particle orthogonal to the wall leaving out the concentration dependance with one wall present is

$$u_p = \frac{2(\rho_F - \rho_P)ga^2}{9\eta_0}(1 + y^{*-1})^{-1} \quad .$$

(3.24)

From the general definition of a velocity follows

$$u_p(y^*) = a\frac{dy^*}{dt}$$

(3.25)

and further on assuming that at the time $t_0 = 0$s particles are located at positions y_0^* with (3.24) and (3.9):

$$\frac{1}{a}\int_{\tilde{t}=0s}^{\tilde{t}=t} d\tilde{t} = \int_{\tilde{y}^*=y_0^*}^{\tilde{y}^*=y^*} \frac{1}{u_p(y^*)}d\tilde{y}^*$$

$$\Leftrightarrow \quad \frac{t}{a} = \frac{1}{u_{St}}\int_{y_0^*}^{y^*}(1 + \tilde{y}^{*-1})d\tilde{y}^*$$

$$\Rightarrow \quad t = \frac{a}{u_{St}}\left(y^* - y_0^* + \ln\frac{y^*}{y_0^*}\right)$$

(3.26)

This equation indicates how long it takes a particle to move from a certain position y_0^* to a position y^*.

A particle volume balance of a layer of width dy^* and area A yields:

$$\frac{\partial}{\partial t}(Ady^*\varphi) = A\varphi(y^*)u_P(y^*) - A\varphi(y^* + dy^*)u_P(y^* + dy^*) \quad (3.27)$$

$$\Leftrightarrow \quad \frac{\partial(\varphi u_P)}{\partial t} = -u_P\frac{\partial(\varphi u_P)}{\partial y^*}$$

$$\Leftrightarrow \frac{\partial(\varphi u_P)}{\partial t} + u_P \frac{\partial(\varphi u_P)}{\partial y^*} = 0$$

$$\Leftrightarrow \frac{DN}{Dt} = 0$$

This is the substantial derivative of the particle flux $N = N_g = u_P \phi_m \varphi$. Thus the particle flux is constant for an 'observing' particle moving with velocity $u_P(y^*)$ as time goes by. At a position y_0^* at the time t_0 the particle flux is the same as the particle flux at the time t at the corresponding position y^* the particle (having been positioned at y_0^* before) is located at a the time t:

$$N(y^*, t) = N(y_0^*, t_0)$$
$$\varphi(y^*, t)u_P(y^*) = \varphi(y_0^*, t_0)u_P(y_0^*) \tag{3.28}$$

With (3.24) and an initial homogenous particle distribution $\varphi(y_0^*, t_0 = 0s) = \varphi_0 = const$ follows:

$$(1 + y^{*-1})^{-1}\varphi(y^*, t) = (1 + y_0^{*-1})^{-1}\varphi_0$$
$$\Leftrightarrow y_0^* = \frac{1}{\frac{\varphi_0}{\varphi(y^*,t)}(1 + y^{*-1}) - 1} \tag{3.29}$$

(3.26) and (3.29) lead to:

$$t = \frac{a}{u_{St}}\left(y^* - \frac{1}{\frac{\varphi_0}{\varphi(y^*,t)}(1 + y^{*-1}) - 1} + \ln\left(y^*\left(\frac{\varphi_0}{\varphi(y^*,t)}(1 + y^{*-1}) - 1\right)\right)\right)$$

$$\Leftrightarrow \frac{t}{t_{St}} = \frac{1}{2}\left(y^* - \frac{1}{\frac{\varphi_0}{\varphi(y^*,t)}(1 + y^{*-1}) - 1} + \ln\left(y^*\left(\frac{\varphi_0}{\varphi(y^*,t)}(1 + y^{*-1}) - 1\right)\right)\right)$$

This is an implicit equation describing $\varphi(y^*, t)$ with $\varphi(y_0^*, t_0 = 0s) = \varphi_0$. The Stokes time $t_{St} := \frac{2a}{u_{st}}$ is defined as the time a particle with Stokes velocity needs to cross the distance of one particle diameter that is two particle radii ($2a$) (cp. equation (3.9)). Fig. 3.11 shows the resulting start-up particle concentration development at various locations in a non-flowing suspension with gravity driving particles away from a wall. The initial particle distribution is homogenous ($\varphi_0 = 0.1$). The closer to the wall, the faster the decrease of particle concentration. As the particle ensemble moves away particles are hold back by the wall: the closer a particle is situated to a wall the lower its velocity. Thus particle movements due to gravity are slowed down by walls. As the particles move away from the wall the particle ensemble is stretched. If $\varphi(y^*) \equiv 1$ the particles form an infinitely expanded block and a steady states persists as $u_P \equiv 0$ (cp. equation (3.24)).
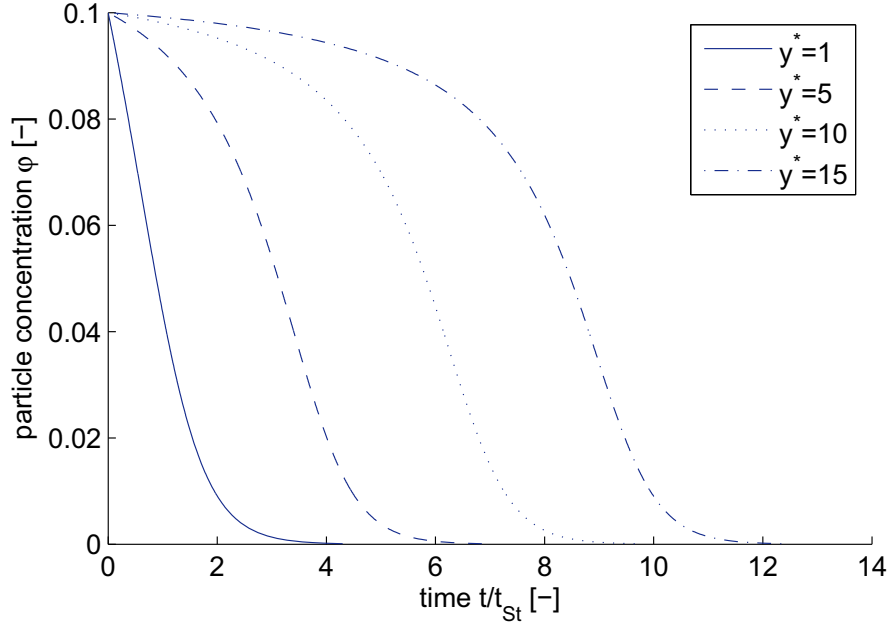
Figure 3.11: Start-up particle concentrations in a non-flowing suspension at various positions with gravity driving the particles away from the wall at an initially homogenous particle distribution $\varphi = \langle \varphi \rangle = 0.1$

Two walls present

In a diluted suspension with gravitation and two walls present with gap width $h^* = 30$ according to (3.8) the velocity of a particle leaving out the concentration dependance for simplicity is

$$u_p = \frac{2(\rho_F - \rho_P)ga^2}{9\eta_0}(1 + y^{*-1} + (h^* - y^*)^{-1})^{-1}. \qquad (3.30)$$

The calculation proceeds similarly to the one before including only one wall. Through (3.25) we obtain

$$t = \frac{a}{u_{St}}\left(y^* - y_0^* + \ln\frac{y^*(h^* - y_0^*)}{y_0^*(h^* - y^*)}\right).$$
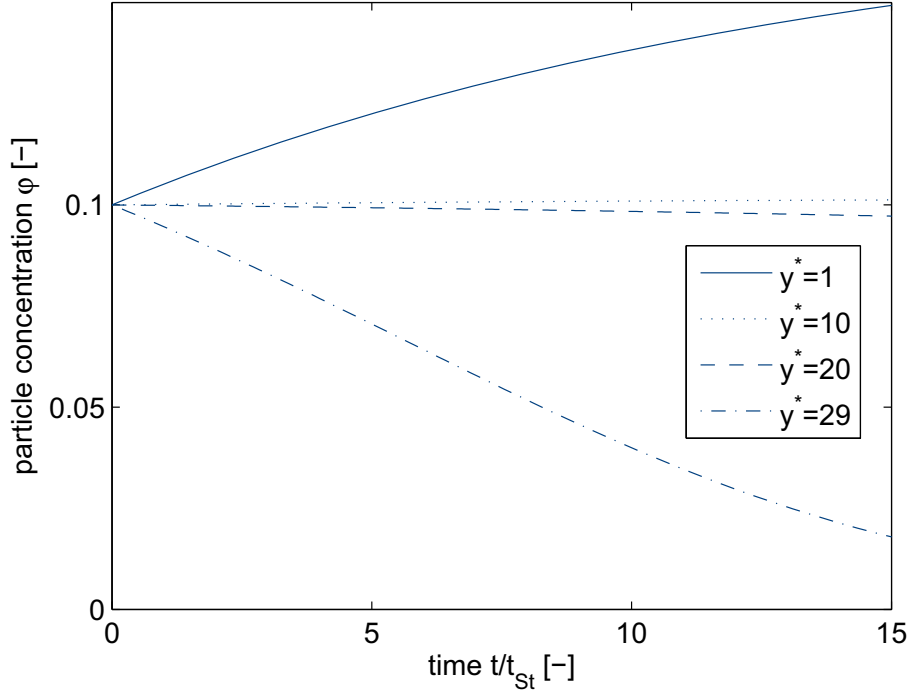
Figure 3.12: Start-up particle concentrations in a suspension at various positions during buoyancy/sedimentation, gap width $h^* = 30$, at an initially homogenous particle distribution $\varphi = \langle \varphi \rangle = 0.1$

(3.27) and therefore (3.28) are also valid here and lead with (3.30) at homogenous initial particle distribution to

$$(1 + y^{*-1} + (h^* - y^*)^{-1})^{-1} \varphi(y^*, t) = (1 + y_0^{*-1} + (h^* - y_0^*)^{-1})^{-1} \varphi_0 \quad .$$

This equation describes only the very start-up of gravity drift in a diluted suspension between two walls as the equation (3.30) is valid only for low particle concentrations. The influence of wall and gravity are opposed at some locations whereas elsewhere they enforce each other. The particle concentration at some positions increases whereas at other positions it decreases (fig. 3.12).

3.2.4   Characteristic Time Scales

In order to assess the time scales on which the demixing activities are taking place we define calculable characteristic times. The characteristic time related to the wall effect caused by shear flow is independant from the characteristic time related to gravity effect.

Characteristic time regarding gravitation   The characteristic time related to the sedimentation or buoyancy of particles due to gravity is defined as the time it takes a particle moving with Stokes velocity u_{St} (equation (3.9)) to cover the distance of $y_t^* = 2$ particle radii:

$$t_g = \frac{a y_t^*}{u_{St}}$$

Characteristic time regarding wall influence   In order to get a property that characterizes the time it needs the wall effect to develop we consider a Couette flow including two walls with an initially homogenous particle distribution without gravity. The characteristic time regarding wall effect is defined as the time after which the particle concentration at the position $y_t^* = 2$ has decreased to half its amount assuming a linear decrease:

$$t_c = \frac{\langle \varphi \rangle - 0.5 \langle \varphi \rangle}{\frac{\partial \varphi}{\partial t}(t = 0, y_t^* = 4)}$$

with (according to (3.11))

$$\frac{\partial \varphi}{\partial t}(t = 0s, y^* = y_t^*)) =$$

$$\frac{2}{9}a(\rho_F - \rho_P)g\eta_0^{-1}\langle \varphi \rangle((1 - \langle \varphi \rangle)^{-2} + y_0^{*-1} + (h^* - y_t^*)^{-1})^{-2}(-y_t^{*-2} + (h^* - y_t^*)^{-2}))$$

$$+ \quad k_\eta \phi_m \frac{\tau_0}{\eta_0}\langle \varphi \rangle^2(1 - \langle \varphi \rangle)^2((1 - \langle \varphi \rangle)^{-2} + y_t^{*-1} + (h^* - y_t^*)^{-1})^{-1}(-y_t^{*-2} + (h^* - y_t^*)^{-2})$$

The tables 3.1 and 3.2 show some examplary values of t_c and t_g with $h^* = 30$, $a = 0.00035$m, $\eta_0 = 32$Pas, $k_\eta \tau_0 = 10$Pa at varying density differences and average particle concentrations. The emphasized data corresponds to the experimental situation described in chapter 4 and in section C.4. In this case t_c and t_g are of the same order of magnitude. A shearing time of several hours at least is needed to obtain a significant demixing effect.

average concentration $\langle\varphi\rangle$ [-]	characteristic time regarding wall effect t_c [s]
0.3	166
0.4	**218**
0.5	343
0.6	669

Table 3.1: Characteristic times regarding wall effect at different average particle concentrations (emphasized data corresponds to experimental situation)

difference of densities $\rho_F - \rho_P$ [g/cm^3]	characteristic time regarding gravity t_g [s]
0.01	8388
0.1	839
0.27	**311**

Table 3.2: Characteristic times regarding gravity effect at different density differences (emphasized data corresponds to experimental situation)

Chapter 4

Experimental Investigation

4.1 Suspension

Various demands are made on the particle-fluid system. Particle size, density and viscosity of the fluid determine together with the shear rate the Reynolds number (equation (3.1)) that has to be low in order to keep the flow creeping. The densities of particles and fluid, the particle size, the viscosity of the fluid, and the particle concentration influence the gravitation effect on the particle drift (equation (3.8)). Thus a suitable balance between these relevant parameters had to be found. In order to make optical recording possible, particles and fluid had to be transparent or at least translucent. The fluid was desired to be newtonian, the particles were requested to possess a spherical shape, a smooth surface, a monodisperse distribution and they were to be non-toxic and large enough to render the brownian motion insignificant. Also homogenous mixing had to be possible. Last, but not least, both phases had to be providable.
A literature research (for example Biederbick [9]) and own tests with water, sugar solution, glycerine, silicone oil, Al_2O_3 spheres and PMMA (polymethylmethacrylate) spheres have shown that the best possible combination for our purposes is invert sugar solution and PMMA spheres.

4.1.1 Fluid Phase: Sugar Solution

As for the fluid phase we use sugar solution of the Südzucker company that consists of dissolved invert sugar and water. Invert sugar is fructose and dextrose in equal shares obtained by hydrolysis of saccharose ($C_{12}H_{22}O_{11}$). The sugar mass concentration of the available solution is $c_{S,0} = 72.7 \pm 0.2\%$. Its density is $\rho_{F,0} = 1.358\text{g/cm}^3$. Thus the density of the dissolved invert

sugar is $\rho_S = 1.59\text{g/cm}^3$ (cp. section C.1). The dynamic viscosity of the solution is $\eta_{0,0} = 450\text{mPas}$ (data at $\theta = 20°\text{C}$).

4.1.2   Disperse Phase: PMMA Spheres

As for the disperse phase we chose PMMA (poly<u>m</u>ethyl<u>m</u>eth<u>a</u>crylate) spheres, density $\rho_p = 1.118 \pm 0.04\text{g/cm}^3$, obtained from the Brace GmbH in Alzenau. An analysis of the particle size distribution with the laser diffraction spectrometer ′HELOS′ at the institute of mechanical process engineering and mechanics in Karlsruhe showed a particle diameter distribution of $100 - 500\mu\text{m}$ (fig. 4.1). Narrowing the distribution was not possible since dry sieving did not work as due to the strong electrostatic charging of the particles immediate agglomeration and blocking of the sieve occurred whereas wet sieving did not work as then particles would get stuck in the pores and and clog the sieve.
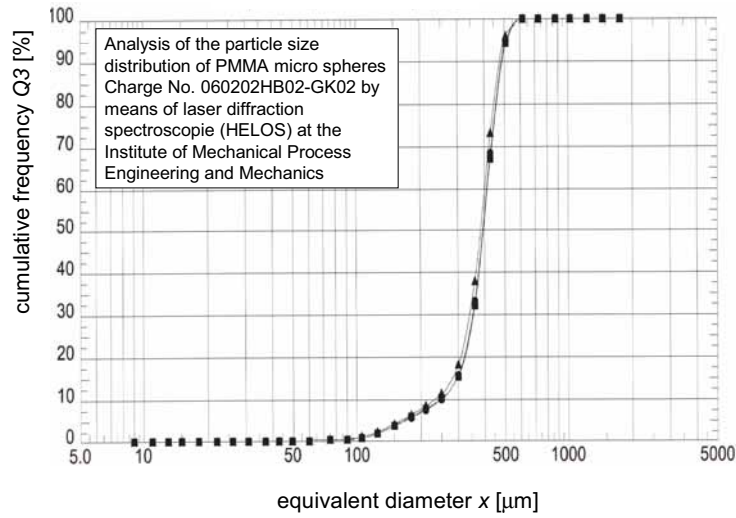
Figure 4.1: Particle size distribution of the disperse phase

4.1.3   Preparation

In order to reach a suitable fluid density and fluid viscosity water was evaporated to increase the sugar concentration, that is to increase the viscosity

and the density of the fluid. A suitable method of evaporating and mixing had to be found. Tests with drying ovens proved to be unsatisfying as the required evaporating time would be too long and also unpredictable. Tests with vacuum chambers also turned out to be inappropriate as mixing with the particles after evaporation would lead to air bubbles and inhomogenities in the suspension. Mixing before evaporating also leads to inhomogenities. Furthermore during the evaporation sedimenting or ascending of the particles takes place what makes the suspension inhomogenous again. Homogenious mixing was possible with a rotary evaporator type 'Laborota 4010 digital' from Heidolph Instruments. Fluid and particles were filled in before evaporation and simultaneous rotation of the flask. The device had no built-in vacuum pump. Instead it worked with a water jet pump at differing water pressure what made operating difficult to control. Therefore an additional vacuum pump with adjustable pressure difference was built in. If the set temperature is too high, the 'Maillard reaction' takes place and the sugar solution is destroyed as the sugar decomposes. Within our experiments we noticed that the reaction started already at an approximate temperature of $\theta = 80°$C although the critical temperature found in literature are significantly higher. So we chose $\theta = 70°$C for the evaporation procedure. At $\theta = 70°$C combined with a certain rotation rate air bubbles became eliminated and a homogenous suspension was produced. The suspension had to be prepared freshly before the experiments because after some days sugar starts crystallizing and particles start swelling.

By setting the amount of evaporated water (density ρ_{H_2O}) the new fluid density ρ_F respectively the sugar concentration c_S (being associated with a certain viscosity η_0) are adjustable as the sugar concentration $c_{S,0}$ of the original sugar solution and the density $\rho_{F,0}$ are known. The desired average concentration $\langle \varphi \rangle$ is determined by the amount of particles added (cp. section C.1). Within our tests the available information table relating sugar concentration of our Südzucker solution to its viscosity turned out to be incorrect. According to our own rheometrical data at high sugar concentrations the viscosity of the solution shows a high sensitivity regarding concentration changes. A suspension containing sugar solution with sugar concentration $c_S = 88\%$ leading to the density $\rho_F = 1.45$g/cm^3 and the viscosity $\eta_0 \approx 35$Pas and PMMA with a concentration $\langle \phi \rangle = 0.4$ proved to be a good combination for experiments with the RheoScope and our self-constructed capillary shearing device. In the flow line to be investigated by NMR the original sugar solution with sugar concentration $c_{S,0} = 72.7\%$ was used. The suspension concentration was $\langle \phi \rangle \approx 0.33$.

4.2 NMR in Combination with a Capillary Shearing Device

As the investigation with nuclear magnetic resonance methods proved to be more suitable than employing an optical parallel plate rheometer the description of the experiments with the Rheoscope is found in the appendix only (section C.4). All NMR measurements took place in the NMR[1] laboratory of the University of Karlsruhe under the direction of Dr. E.H. Hardy.

4.2.1 Experimental Setup

Both the suspension and a pure sugar solution are sheared in a tube that is a removable part of a special capillary shearing device. Inserting the tube in a NMR tomograph the magnetic resonance of ^{1}H is detected allowing for instance the determination of the particle distribution.

Marvin - A Special Capillary Shearing Device
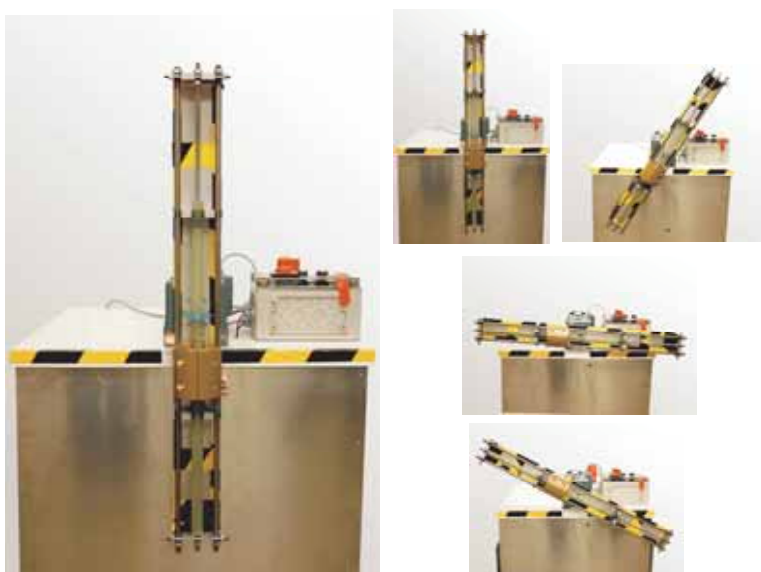
Figure 4.2: The capillary shearing device

---

[1]Nuclear Magnetic Resonance

The used capillary shearing device (fig. 4.2) was constructed meeting the special demands in consequence of the NMR investigation. The suspension in a tube (inner diameter 22mm, length approximately 40mm) is positioned between two bulbs. In vertical position the tube together with an attached weight glides downwards slowly due to gravity whereas the bulbs and the overall volume holding the fluid remain fixed. Thus a laminar tube flow is generated. The arrival of the tube below activates a magnetic position switch that starts rotating the tube by the in-build engine at a fixed angular velocity. After rotating 180° another vertical position is reached the weight being at the top activating a second switch that stops the rotation. The weight
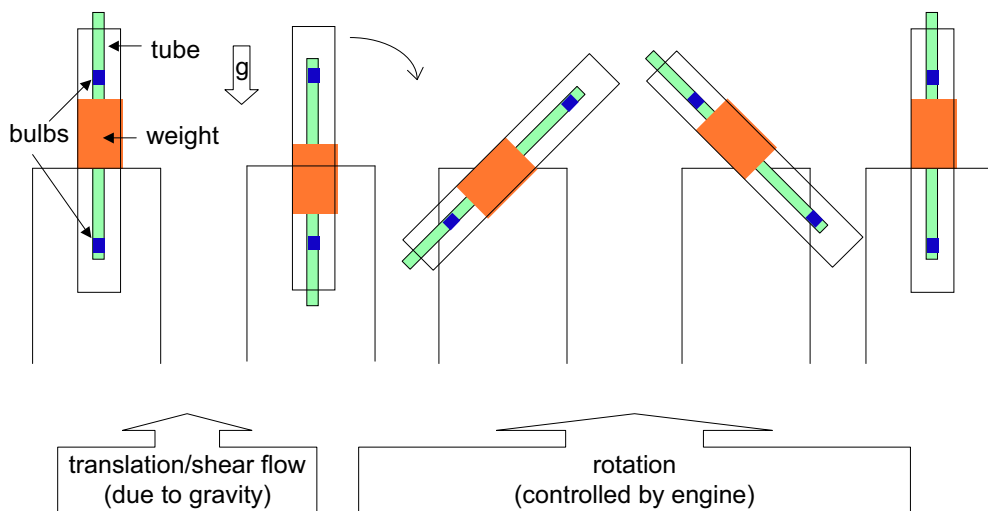
Figure 4.3: Shearing principle of the capillary shearing device

starts coming down again and the described process begins anew (fig. 4.3). The engine is a spur gear motor from the company SEW with the following characteristics:

number of revolutions: 1380/min

power: 0.12kW

frequency: 50Hz

voltage: 230V While the resulting oscillatory movement of the tube generally means a recurrent reversal of the shear flow no turning back of the particle diffusion is involved. The particle drift orthogonal to flow accumu-

lates during the oscillatory shear process as the flow direction is irrelevant regarding the relevant gradients. At the turning point the structure is fixed since no Brownian motion occurs. A suspension with average particle concentration $\langle \varphi \rangle = 0.4$ and a sugar concentration of $c_S = 88\%$ as well as a pure $c_S = 88\%$ sugar solution were chosen. The particles ascend slow enough (cp. table 3.2) not to override the hydrodynamic diffusion. While shearing the particle rise is directed parallel to the flow direction and orthogonal to diffusion. The rotation time during which gravity and diffusion have common direction components is much shorter than the characteristic time regarding gravity. Overall the gravitation effect does not disturb the diffusion process significantly.

NMR Spectrometer

The employed Bruker spectrometer is based on a super-wide-bore cryo magnet of Bruker Spektrospin/Oxford Instruments. The bore is 150mm wide. The console is an Avance 200. The diameters of the gradient system are 40mm (inner) and 72mm (outer). We used a wide-bore Micro 2.5 (inner diameter 25mm) probe. The induction of the electromagnetic field is 4.7Tesla. The gradient sensitivity was 0.025T/m/A and the maximum gradient was 1T/m. As for data processing the Paravision Software was applied. The pulse sequences used were a multi slice multi echo (msme) and an imaging sequence supplemented by a gradient coding the velocity (sevi) both provided by the Bruker company.

4.2.2 Results

Demixing As the relaxation times of the protons in the aqueous sugar solution differ from the one in the particles the spin density and hence the intensity of the NMR signal corresponds to the particle distribution. Due to the shorter T_2 time of PMMA compared to the matrix fluid it is possible to visualize the particle distribution in the suspension by MRI[2] methods. Up to five contiguous slices at a time perpendicular to the tube axis were analyzed the slice thickness being 5mm, 10mm or 20mm. The field of view was 25mm × 25mm. The cross-sectional multi slice spin echo images of the tube filled with suspension before and after shearing with Marvin (fig. 4.4) show that indeed a demixing took place. After shearing a lower signal at the axis of the tube means an increased particle concentration there (cp. the paragraph about the pure sugar solution and C2). This result is also visible

---

[2]Magnetic Resonance Imaging
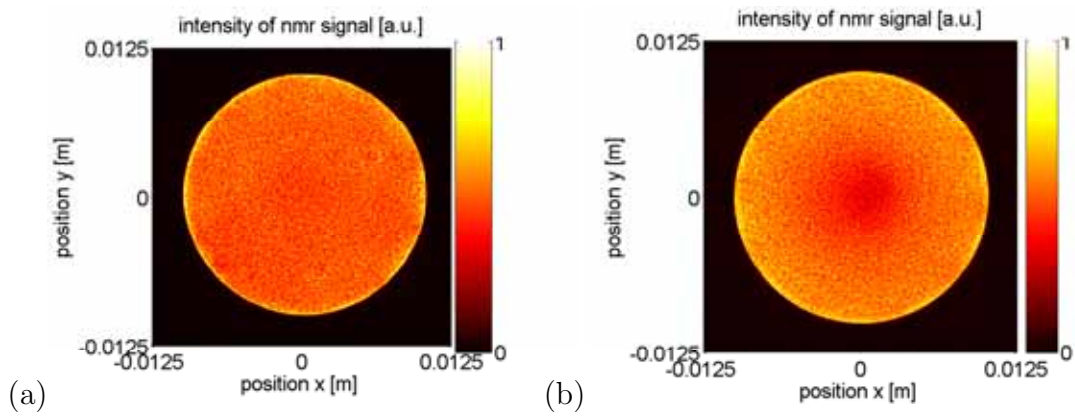
Figure 4.4: MRI images of a suspension containing 88% sugar solution and particles in a tube before (a) and after (b) shearing
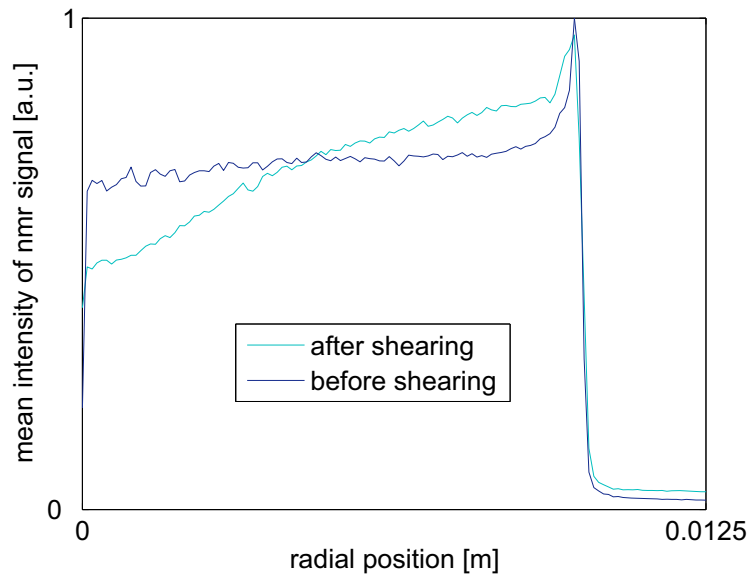
Figure 4.5: Intensity of the NMR signal of a suspension in a tube

in fig. 4.5 showing the average signals (summation over annuli) as a function of the radial coordinate of the rotation-symmetrical system. By calculating the average function the fluctuation originating in the particle distribution is eliminated. At the circumference of the cross section the twelve equidistant points of high intensity are artifacts due to the legs of the bird cage (more
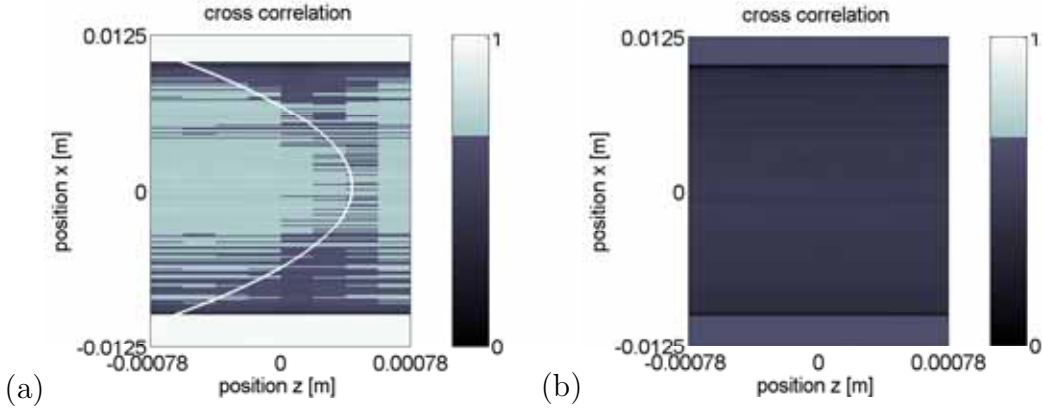
Figure 4.6: Cross correlation of the suspension with 84% (a) and 88% (b) solution, in each case 10 minutes elapsed between the correlated states (white parable added for clarification)

clearly visible in fig. 4.11).

Cross correlation   In order to be sure that while taking the NMR data the suspension in the vertically positioned tube does not change its particle distribution significantly we investigate the correlation of the measured signal intensities $\vec{I}_1(z) = (I_{1,1}(x_1, z), I_{1,2}(x_2, z), ..., I_{1,n}(x_n, z))$ and $\vec{I}_2(z) = (I_{2,1}(x_1, z), I_{2,2}(x_2, z), ..., I_{2,n}(x_n, z))$. The NMR signals are taken at an interval of 10 minutes. We apply the cross correlation function defined as

$$\vec{I}_1(z) \star \vec{I}_2(z) = \int_{-\infty}^{\infty} \overline{\vec{I}_1}(\tilde{z})\vec{I}_2(z + \tilde{z})d\tilde{z} = \mathcal{F}[\overline{\mathcal{F}^{-1}(\vec{I}_1(z))}\mathcal{F}^{-1}(\vec{I}_2(z))] \quad .$$

In this case the minimum value of the cross correlation gives the most probable position at which the structure of the signal being positioned before at $z = 0$ can be found within $\vec{I}_2$. We calculate the cross correlations of the MRI images before and after the measuring procedure of suspensions with differing fluid viscosities. The result of the cross correlation using a suspension containing a 84% sugar solution and particles shows a vertical parabolic translation (a white parable was added for clarification) (fig. 4.6a). This means that the particle – fluid structure in the tube has moved parable-like per approximately 800μm. This value is comparable with the translation Δz of a particle moving with Stokes velocity u_{St} (cp. equation (3.9)):

$$\Delta z = u_{St}600s = 1350\mu\text{m}$$

Most likely the ascension of particles due to gravity is represented here. Near the wall the particle velocity is lower as there is a higher resistance to displacement of the fluid. The fluid viscosity of this system is lower than the fluid viscosity of the 88% solution that was used for the NMR measurement. The suspension containing a 88% sugar solution shows no significant structure shift (fig. 4.6b). Thus recording the NMR data is not affected by particle ascension due to gravity in the suspension.

Geometrical structuring In highly concentrated suspensions a certain geometrical ordering due to the restriction imposed by the walls might take place. It is expected to be similar to the geometrical structure established
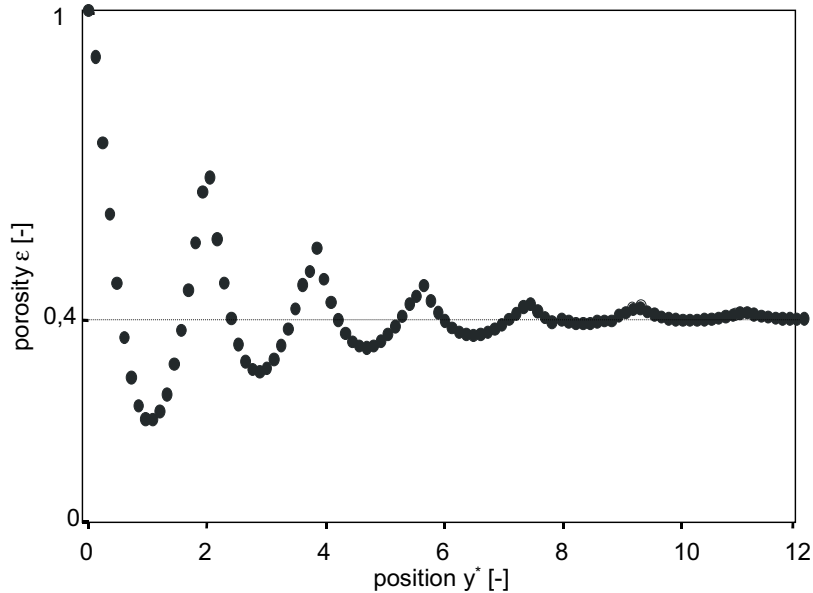
Figure 4.7: Porosity in a sphere packing with $\langle\phi\rangle = 0.6$ calculated by Rottschäfer [39]

in sphere packings calculated by Rottschäfer [39] (fig. 4.7). The oscillating structure starts at the wall with zero particle concentration. With increasing distance to the wall the particle concentration oscillates with fading amplitude. The distance between two peaks is slightly smaller than one particle
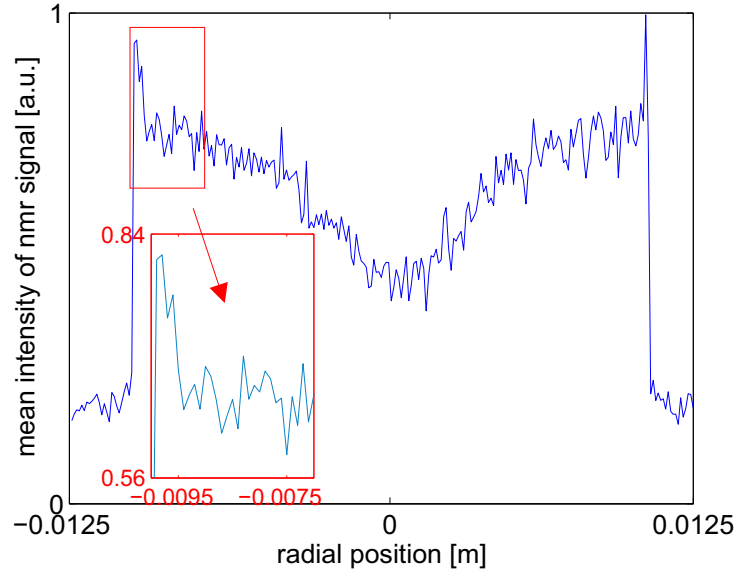
Figure 4.8: Intensity of the NMR signal of a suspension in a tube after shearing

diameter. Near the wall the average intensity of a NMR signal of a suspension in a tube representing the particle distribution shows similar peaks also being spaced at intervals of one diameter (fig. 4.8). As the inherent noise was eliminated by averaging we assume that the shape of the curve represents the geometrical structure of the suspension.

Simulation Simulating the NMR signal of a suspension (spin density of PMMA set to zero) with randomly distributed particles of quadratic shape determined by the Monte Carlo method again demonstrates artifacts at the phase boundaries near the wall and at the particle contours (fig. 4.9). The simulation of discrete signal responses makes the identification of artifacts generated by the fast Fourier transformation into reciprocal space possible. The Gibbs artifacts develop around steps of the spin density function [17]. Here the NMR signal resulting from an ideal measurement was simulated. In case of a tube (spin density set to zero) containing a pure solution (spin density 1) the result (fig. 4.10) shows peaks being spaced at $\approx 200\mu$m being close to the average particle diameter. Hence also artifacts might be the origin of the measured peaks of the suspension in fig. 4.8. To find out if that is the

(a)   (b)
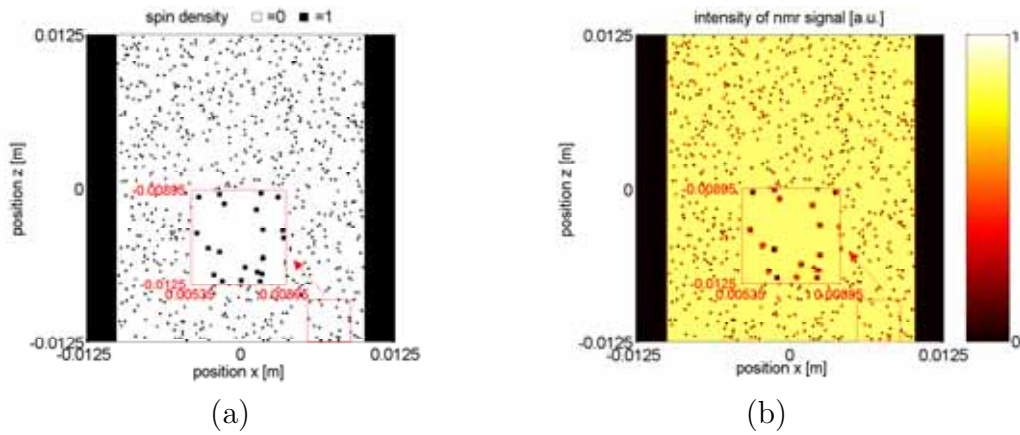
Figure 4.9: Simulated spin density (a) and NMR signal (b) of a suspension in a tube with randomly distributed particles of quadratic shape: the NMR signal (b) shows artifacts at the phase boundaries near the wall and at the particle contours

(a)   (b)
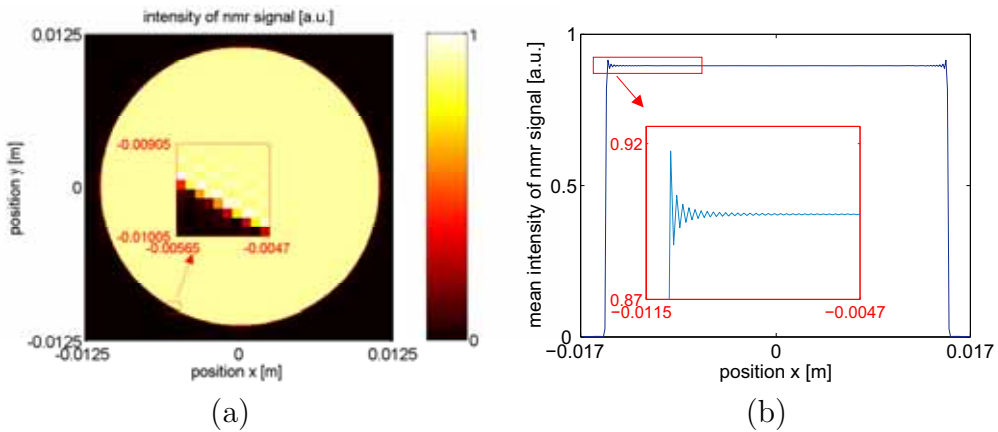
Figure 4.10: The simulation of a NMR signal of a pure solution (spin density 1) in a tube (spin density 0) shows artifacts at the tube wall: (a) axial cross-section of the tube (b) average intensity

case further measurements will be necessary. The distance between peaks of the signal intensity distribution of suspensions containing particles with a different average particle diameter would behave approximately proportional to the particle diameter if the effect results from the geometric structure. If

the oscillation of the signal intensity are Gibbs artifacts the distances are not dependant on the particle diameter. Comparisons between the simulation of the spin density and the NMR signal of a suspension with the average concentration $\langle \varphi \rangle = 0.4$ (not possible here due to the restricted computation time) to the measured signal (fig. 4.8) might render interesting conclusions.

Pure sugar solution   The spin echo of a pure sugar solution before and after shearing reveals that the intensity of the NMR signal at the tube axis also decreases while shearing (figs. 4.11 and 4.12). Here the signal difference

(a)   (b)
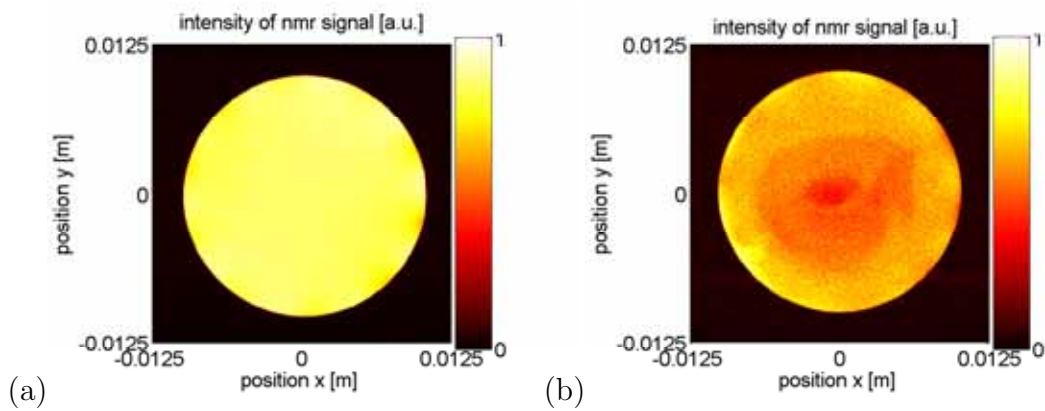
Figure 4.11: MRI images of a 88% sugar solution in a tube before (a) and after shearing (b) (axial cross-section of the tube)

(a)   (b)
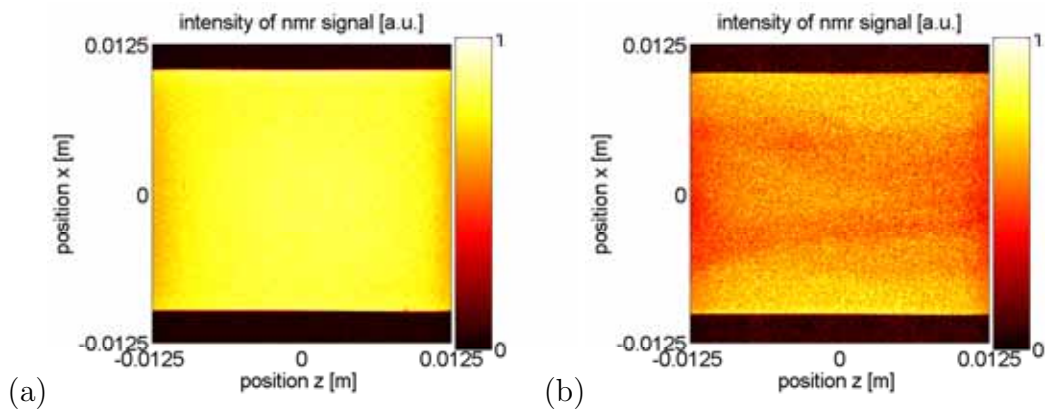
Figure 4.12: MRI images of a 88% sugar solution in a tube before (a) and after shearing (b) (radial cross-section of the tube)

apparently originates in a relaxation contrast (T_2). There are several possible explanations. The relaxation contrast might be generated by a crystallization of the sugar whereas crystallization occurs only at the axis of the tube since crystallization at the wall is prevented by high shear rates. Alternatively the crystallization might occur in the whole tube creating a suspension consisting of sugar solution and sugar crystals (average volume concentration $\langle \varphi_S \rangle$) that arranges according to the principle of minimum energy dissipation in tube flow as follows. The viscosity of a homogenous suspension is with (2.3):

$$\eta = \frac{\eta_0}{(1 - \langle \varphi_S \rangle)^2} \tag{4.1}$$

Considering on the other hand a plane Couette flow with inhomogenous crystal distribution (along the gap) with the same average crystal concentration $\langle \varphi_S \rangle$ the crystal concentration can be described as $\varphi_S(y^*) = \langle \varphi_S \rangle + \delta \varphi_S(y^*)$ with $\int_0^{h^*} \delta \varphi_S(\tilde{y}^*) d\tilde{y}^* = 0$. In this case the average viscosity defined as

$$\langle \eta \rangle = \frac{\int_0^{h^*} \eta(y^*) d\tilde{y}^*}{h^*}$$

is

$$\langle \eta \rangle = \frac{\eta_0}{h^*} \int_0^{h^*} \frac{d\tilde{y}^*}{(1 - (\langle \varphi_S \rangle + \delta \varphi_S(\tilde{y}^*)))^2} \tag{4.2}$$

from which we get:

$$\begin{aligned}
\langle \eta \rangle &= \frac{\eta_0}{h^*} \int_0^{h^*} \frac{d\tilde{y}^*}{(1 - \langle \varphi_S \rangle)^2 - 2\langle \varphi \rangle (\delta \varphi_S(y^*)) + (\delta \varphi_S(y^*))^2} \\
&= \frac{\eta_0}{h^*} \int_0^{h^*} \frac{d\tilde{y}^*}{(1 - \langle \varphi_S \rangle)^2 + (\delta \varphi_S(y^*))^2}
\end{aligned}$$

Since $(\delta \varphi_S(y^*))^2 \geq 0$ the macroscopical viscosity of a non-homogenous system is the lower the more inhomogenous the crystal distribution. Thus the maximum energy dissipation comes along with a homogenous distribution and the signal distribution in figs. 4.11 and 4.12 might correspond approximately to a minimum energy dissipation.

Another cause of the low NMR signal at the axis might be inhomogenities of the sugar solution characterized by differing sugar concentrations that arrange again according to the described principle of minimum energy dissipation. (Hereby it is assumed that here also the macroscopical viscosity increases with decreasing homogenity.) The distinct areas of low signal visible left and right in fig. 4.12 are artifacts resulting from inhomogenities of the B_1 field most likely. Since the ratio of the signal difference between wall

area and axis-area related to the average signal is considerably lower than the corresponding value regarding the suspension it can be assumed that the origin of the signal difference in the suspension is not a crystallization effect but actual demixing (cp. section C.2).

4.3 NMR in Combination with a Flow Line

4.3.1 Experimental Set-Up

The NMR measurements were performed using the equipment described in section 4.2.1. A gravity-driven tube flow is led through the spectrometer allowing to measure the spin density and the velocity profile of the suspension during flow.

The Flow Line

The suspension is flowing out of a reservoir through a rubber hose passing vertically through the tomograph into a second reservoir that is lower positioned than the first one (fig. 4.13). A peristaltic pump sends suspension

$$(a) \qquad\qquad\qquad (b)$$
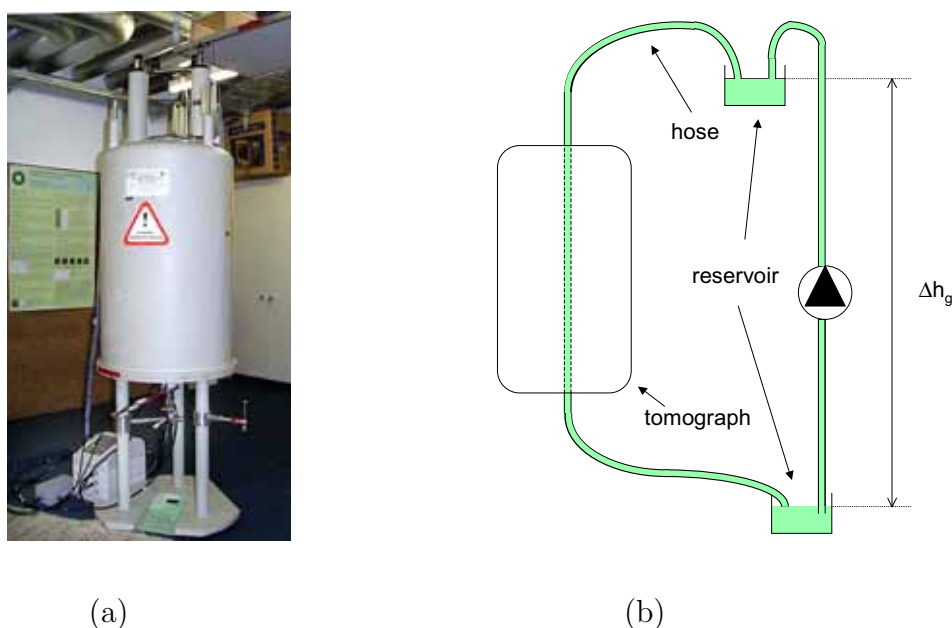
Figure 4.13:
Principle of the tube flow (b) leading through the spectrometer (a)

from the downward reservoir to the upper reservoir through another tube. In the tube over the measuring volume a mechanical mixing device is positioned. The inner diameter of the tube leading through the tomograph is 20mm. The flow rate is controlled by adjusting the pressure difference determined by the

difference of altitude regarding the two reservoirs. We did not generate the flow through the tube with the pump directly due to the unwanted pulsation of the generated flow. We used a suspension containing a 72% sugar solution and PMMA with an average particle concentration $\langle\varphi\rangle = 0.4$.

4.3.2 Results

In order to determine the spin density and the velocity profile of the flowing suspension the spin echos in response to the msme respective sevi pulse sequence were measured. The image matrix was 256×256. The results for differing flow rates are shown in fig. 4.14. The particle concentration near
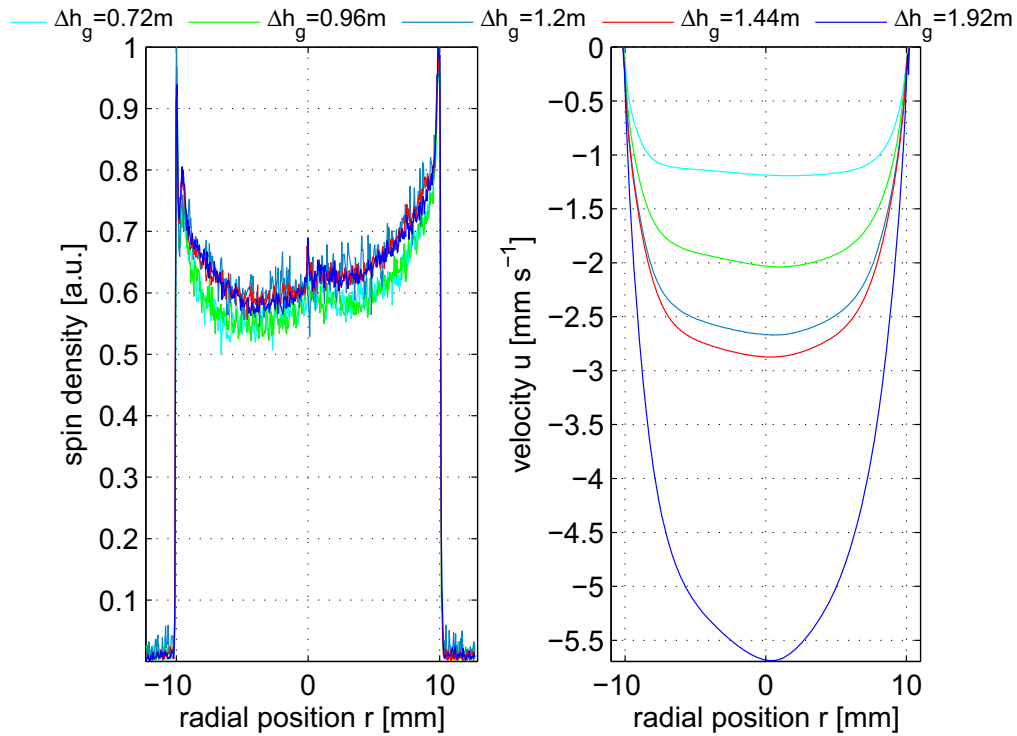
Figure 4.14: Spin density and velocity profile in Poiseuille flow of a suspension determined by NMR

the tube wall is lower than along the axis of the tube. The velocity profile is flater than the parabolic shape that is typical for Poiseuille flow. This is to be expected as the inhomogenous particle distribution results in decreased

shear rates at the center and increased shear rates near the wall. The faster
the flow the more pronounced are these characteristics of the velocity profile.
The asymmetry of the profiles and the artifacts at the centerline of the tube
may be caused by the imprecise centering of the tube related to the spec-
trometer opening. The shear rate profile of the flow is determined from the
velocity profile by equation (2.1). From the pressure loss

$$\frac{\partial p}{\partial x} = \frac{\rho g \Delta h_g}{L}$$

(Δh_g being the effective difference (cp. fig. 4.13) of altitude and L being the
total length of the hose) the shear stress in laminar tube flow follows:

$$\tau(r) = \frac{\partial p}{\partial x} r$$

Additionally we take into account a further pressure loss that is proportional
to the difference of altitude (cp. section C.5) while calculating the viscosity
from shear rate and shear stress with (2.2). Considering the fluidity $f = 1/\eta$
instead of the viscosity η minimizes the artifacts caused by $\dot{\gamma}(r = 0) = 0$
and $\tau(r = 0) = 0$ at the axis of the tube (fig. 4.15). Finally we obtain the
particle concentration profile from the viscosity that is a function of the con-
centration (equation (2.3)). The result agrees with the particle concentration
represented by the spin density (4.16). Furthermore it exhibits the theoret-
ically predicted depletion of particles near the wall (fig. 3.6). Whereas the
spin density results from the raw resonance data the alternative determina-
tion of the particle concentration profile is based on the rheological properties
of the system derived from the velocity profile. That way two independent
fields that are NMR and rheology are connected offering great multifaceted
potential so far not utilized.
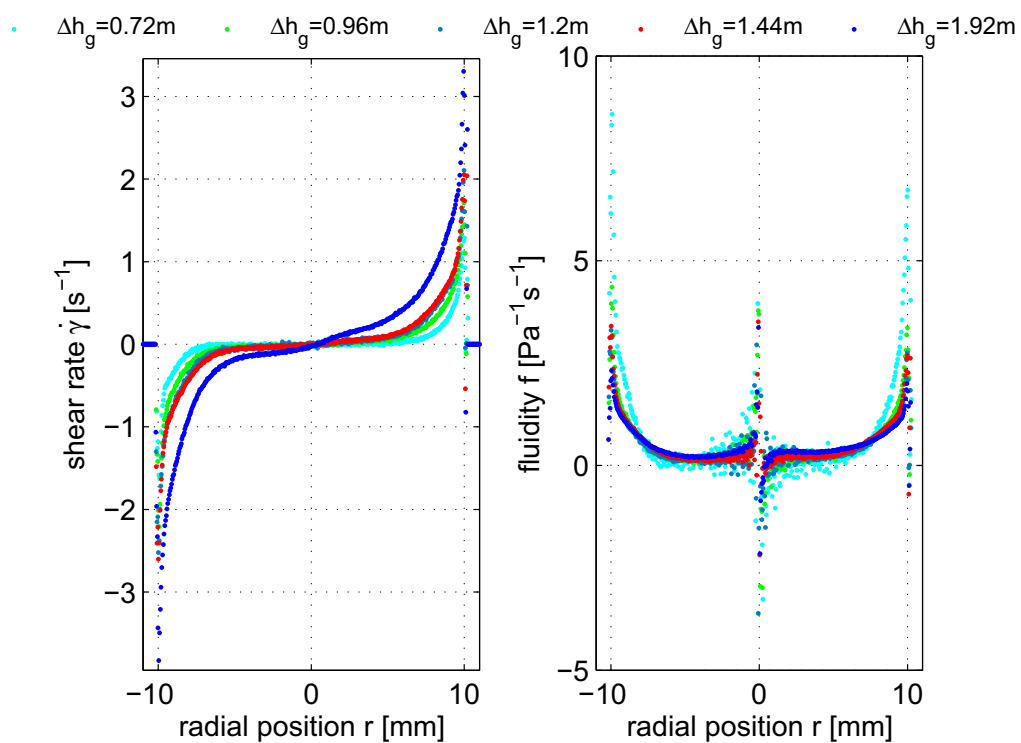
Figure 4.15: The shear rate and the fluidity in tube flow of a suspension calculated from the velocity profile
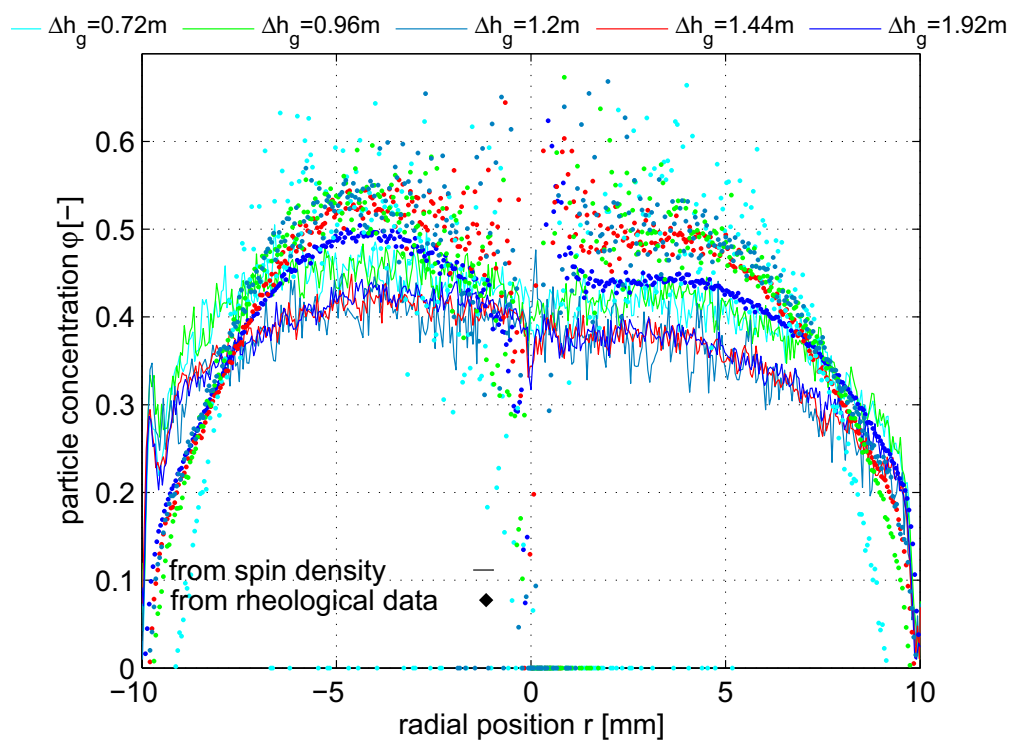
Figure 4.16: The particle concentration in Poiseuille flow of a suspension determined from the spin density and alternatively from the rheological properties following from the velocity profile

Chapter 5

Numerical Simulation

5.1 Method

At the Institute of Computational Fluid Dynamics of the University of Stuttgart simulations of sheared suspensions took place under the direction of Prof. Herrmann [2]. For this a modified lattice-Boltzmann method was used. The lattice Boltzmann method connects the Navier-Stokes equations with the dynamics of a diluted gas resulting in the Boltzmann equation transferred to a discrete form. The phase interface between fluid and particles is defined by a boundary condition that is a 'link-bounce-back' collision rule. The particle motion is described by the Newton equation. Certain special cases involving lubrication interactions or particles coming very near each other have to be treated separately. In order to reduce the computing time the desired system sizes are represented by a smaller size in combination with periodic boundary conditions. Simulations of a homogenous sheared suspension between two walls experiencing gravity and hydrodynamic diffusion varying the Reynolds number, the total particle concentration and the fluid viscosity were conducted.

5.2 Results

The simulated particle concentration profile of a sheared suspension at steady state with parameters corresponding to $\langle \varphi \rangle = 0.4$, $h^* = 30$, $a = 100 \mu$m and $\rho_F - \rho_P = 0.27$g/cm^3 (fig. 5.1) shows that the particle concentration oscillates with a decreasing amplitude. The maxima are spaced at one particle diameter. This result is similar to the geometrical structuring in sphere packings (fig. 4.7) and also to the concentration profile of a suspension determined by NMR (fig. 4.8). Near the wall a particle-free region and the resulting pseudo
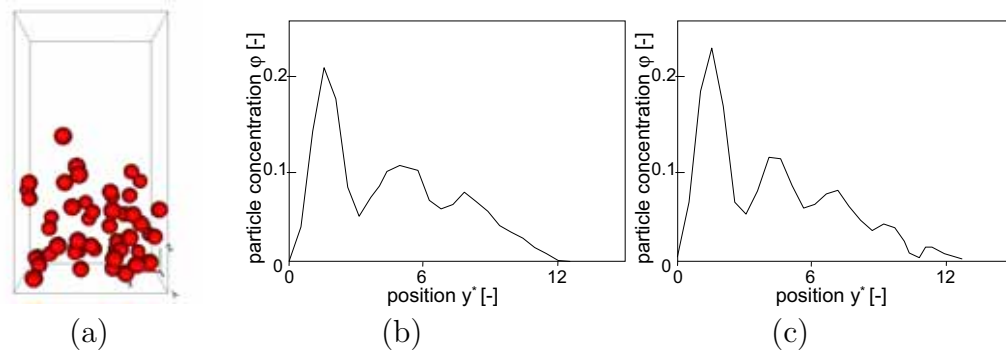
Figure 5.1: Example of a simulated system (volume $V = 11.3025 * 10^{-9} \text{m}^3$) consisting of 50 sedimenting spheres sheared with a shear rate $\dot{\gamma} = 0.03375$ Pas^{-1} (a) and the particle concentration profile of a sheared suspension with an average particle concentration $\langle \varphi \rangle = 0.4$ and gap width $h^* = 30$ sheared with shear rate $\dot{\gamma} = 10\text{s}^{-1}$ (b) and $\dot{\gamma} = 1\text{s}^{-1}$ (c) with particle radius $a = 1.125\mu\text{m}$, particle density $\rho_P = 1176\text{kg/m}^3$, fluid viscosity $\eta_F = 0.45\text{Pas}$ and fluid density $\rho_F = 1446\text{kgm}^{-3}$ at the time $t = 729\text{s}$

wall slip corresponding to the theoretically determined boundary layer is present. The shear flow with the higher shear rate (fig. 5.1b) and therefore with the higher shear strain at the given time shows a concentration profile that is more distinct. Also the simulated distribution functions of the particle-particle distances, of the particle-wall distances and of the particle velocities in flow direction show these phenomena [2]. Particle velocity functions in all spatial directions were determined. The distribution of velocities perpendicular to the walls exhibits a greater width than the velocities parallel to the walls and perpendicular to the flow direction. This is a consequence of the hydrodynamic diffusion across the flow direction. The particle migration due to hydrodynamic interactions parallel to the wall and perpendicular to the flow direction is approximately zero as the gradients of concentration, shear rate and resistance force in these directions. The particle distribution is a function of the shear strain as predicted by the theoretical model.

Chapter 6

Comparison and Outlook

As from the model certain properties of a Couette flow with and without gravity and of a non-flowing suspension were determined the NMR experiments deal with the tube flow of a suspension. Thus a comparison of experimental and theoretical results is limited to qualitative tendencies. Both model and experiments exhibit a demixing of an initially homogenous suspension during shearing whereas the particle drift always is directed away from the walls leading at steady state to a maximum particle concentration at the position farthest from the walls and a low particle concentration near the wall.

The calculated characteristic time scale of demixing due to wall influence agrees with the decrease of the time-dependant viscosity function of a suspension measured with a parallel plate rheometer.

The calculated characteristic time regarding demixing due to gravity corresponds quasi exactly to the ascending time of the particles in the tube within the NMR experiments.

So far the functional relation between NMR signal and particle concentration in the was known only qualitatively. Performing additional NMR measurements with pure sugar sirup and a solid PMMA brick to calibrate are recommended. Thereby the sugar concentration of the solution has to be identical to the one of the solution in the suspension.

In order to evaluate the geometrical ordering experimentally NMR experiments with other particle size might be carried out or the NMR signal noise and the Gibbs artifacts have to be filtered out.

Chapter 7

Abstract

The object of this work was the analysis of wall effects in shear flow of suspensions. The development of a new phenomenological model describing the wall influence was combined with an experimental investigation.

In shear-flowing suspensions demixing processes and particle transport take place due to hydrodynamic diffusion. Particle-particle interactions lead to statistical fluctuations of the particle velocities. Shear rate gradients and particle concentration gradients as well as viscosity gradients orthogonal to the flow direction might generate an overall particle drift orthogonal to the flow direction. A gradient of interaction frequency consisting of shear rate and particle concentration gradients makes the particles tend to drift away from the areas of higher interaction frequency. The viscosity affects the average distance a particle translates orthogonal to the flow direction induced by an interaction – the particles tend to drift towards the areas of lower viscosity being connected with a lower resistance force acting on the particle. The macroscopic effect of a systematic shear-induced particle drift results in inhomogenities of the suspension. Phillips et al. [33] have set up a diffusion equation concerning these transport processes. The phenomenon of pseudo wall slip might originate in the mechanism of hydrodynamic diffusion. An area with low particle concentration near the wall leads to high shear rates and a steep velocity increase. Macroscopically observed the flow seems to slip along the wall.

A solid boundary wall also affects the particle drift. The new approach is basing on the fact that the resistance force acting on particles very near the wall moving orthogonal to the wall is increased as the liquid in the gap between particle and wall has to be pushed out of or pulled into the gap. The new approximation of the resistance coefficient being a function of the

distance to the wall matches very well the findings of Happel and Brenner
[12] concerning the resistance force under the described circumstances. The
new model allows to set up a new diffusion equation including wall influence.
A further addition is made taking into account sedimentation or buoyancy
directed parallel to the particle drift. The constitutive equation describes
the particle concentration as a function of time and position in the gap of
a suspension (Couette flow) accounting for wall effect and gravity. The de-
termination of further flow properties either analytically or numerically is
possible. The particle concentration profiles, shear rate profiles and velocity
profiles of half-infinite and two-wall Couette flows at steady state with and
without gravity were calculated as well as the start-up particle concentration
development of a non-flowing suspension with one and with two walls expe-
riencing gravity.
In general the following points can be stated regarding the results:

- In a shear flow the wall generates a particle drift directed away from
  the wall.

- As a consequence at steady state the particle concentration near the
  wall is a monotone function that approximates zero at the wall and
  rises with increasing distance to the wall (except the area contains no
  particles at all due to gravity).

- A boundary layer of low particle concentration can be found at the wall
  leading to a pseudo wall slip.

- Even if gravity steers the particles towards the wall this is still the case.

- At initial homogenous particle distribution the establishment of the
  boundary layer needs only a very low strain and happens thus very
  fast.

- The boundary layer becomes more narrow with increased average par-
  ticle concentration.

- The non-injectivity of the mathematical solution defines a discontinuity
  of the physically occuring particle concentration.

- During an experiment without gravity at a fixed initial particle concen-
  tration in a pure shear flow the particle concentration is dependant on
  the total strain and not on the occuring shear rates or shear stresses.
  This is valid in half-infinite flow as well as if two walls are present.

- The process of sedimenting or rising of particles in a suspension (no flow) is slowed down by the wall.

In order to analyze the particle distributions in shear-flowing suspensions experimentally the method of nuclear magnetic resonance was employed basing on the detection of protons serving as sensors (H-NMR). Differing NMR signal intensities of matrix fluid and particles deliver makes it possible to distinguish between matrix fluid and particles.

With regard to that a special shearing device realizing an oscillating tube flow of unlimited shearing time was designed and constructed. After shearing the removable tube can be taken out and inserted into the nuclear magnetic resonance tomograph. In this way the spin density distributions of suspensions and pure solutions were determined. The viscosity of the substance was high enough to prevent further rearranging of the particles during measuring time. This was verified checking cross correlations. To find out NMR-specific artifacts appearing at the discontinuities of the spin density function the NMR signals of a pure solution in a tube and of a suspension were simulated. The spin density distribution of the suspension was set by the Monte Carlo method.

In addition the gravity-driven tube flow of a suspensioncontaining an in-build mechanical blending device was analyzed insitu whereas a hose was leading directly through the NMR spectrometer. Spin density profiles (representing the particle concentration) and velocity profiles were measured. From the velocity profiles shear rate profiles and viscosity profiles could be determined. The viscosity again leads to a particle concentration profile refering to the equation of Krieger and Dougherty (2.3). Additionally the viscosity function of the suspension was measured with a parallel-plate rheometer.

The experimental findings follow.

NMR measurements offline:

- The magnetic resonance images of the suspension before and after shearing show that an accumulation of particles in the initially homogenous suspension formed in the centre of the tube. At the tube wall the particle concentration is low in agreement with the theoretical results (pseudo wall slip).

- The oscillatory structure with fading amplitude of the NMR signal intensity near the wall corresponds with the porosity function calculated by Rottschäfer [39] representing a geometrical ordering induced by the restrictions being imposed by the wall. The distance between two neighbored maxima is slightly less than one particle diameter.

- This structure also appears in the lattice Boltzmann simulation of the shear flow of a suspension by Herrmann et al. [2].

- The NMR signal of a tube containing pure solution obtained by simulation shows artifacts (Gibbs phenomenon) that resemble the oscillatory structure.

- The NMR signal of a pure sugar solution being homogenous at beginning shows after shearing also a reduced spin density at the center of the tube. This corresponds to the state of minimum energy dissipation according to which the areas with higher viscosity that might consist of crystallized sugar are found in the middle of the tube.

- Directly after the blending device the particle concentration is homogenous whereas some centimeters farther the decreased spin density at the center of the tube shows that a demixing has taken place.

- At this position the stationary velocity profile (slightly flatter than parabola-like) has established.

- From the measured velocity profile the viscosity profile and the particle concentration follow.

- The particle concentration profile determined from the spin density distribution agrees well with the particle concentration derived from the velocity profile.

Measurements with a parallel-plate rheometer:

- The start-up short-term increase of the viscosity corresponds to an initial homogenization.

- The short descent of the viscosity might represent a demixing connected to the wall influence. The time scale approximately shows the same order of magnitude as the calculated characteristic time regarding wall influence.

- The superposed longer enduring decrease of the viscosity might be attributed to the gravity drift of the particles the time scale matching the theoretical considerations.

List of Symbols

Latin Symbols

symbol	dimension	meaning
a	m	particle radius
a_ϕ	1	increase factor
A	m^2	area
A	m^2	auxiliary function
A	1	factor
A'	1	factor
b	1	exponent
B	1	factor
$\vec{B}$	T	magnetic field
$\vec{B}_0$	T	static magnetic field
$\vec{B}_1$	T	radiofrequency magnetic field
c_S	1	sugar mass concentration of fluid
$c_{S,0}$	1	sugar mass concentration of original sugar solution
C	s^{-1}	integration constant
d	1	NMR signal difference related to average signal
E	J	energy
E	1	NMR signal
E_{m_I}	J	energy of a nucleus occupying state m_I
f	Pa^{-1}s^{-1}	force
F	N	force
F_A	N	lift force
F_G	N	mass force
F_{St}	N	Stokes resistance force
$F_\perp$	N	resistance force related to movement orthogonal to flow direction
$F_\parallel$	N	resistance force related to movement parallel to flow direction

symbol	dimension	meaning
g_i	Pa	storage modulus belonging to relaxation time λ_i
G	Pa	shear modulus
$\vec{G}$	T/m	magnetic field gradient
G'	Pa	shear storage modulus
G''	Pa	shear loss modulus
h	m	gap width
h^*	1	gap width related to particle radius
Δh_g	m	difference of height
H	m	gap width (Couette flow)
I	1	spin quantum number
I	1	intensity of signal
$\vec{I}$	1	intensity of signal
$\vec{I}$	kg m/s	angular momentum
k	Pa s^n	factor
k	1	ratio of diffusion constants $k := k_f/k_\eta$
k_f	1	diffusion coefficient related to interaction frequency
k_η	1	diffusion coefficient related to resistance force
$\vec{k}$	1/m	reciprocal space referring to magnetic field gradient $\vec{k} = \frac{\gamma \int_0^t \vec{G}(t)dt}{2\pi}$
K	1	abbreviation $K := \varphi_\infty(1 - \varphi_\infty)^{2(1-1/k)}$
L	m	length of tube or capillary
m	1	exponent
m_I	1	magnetic quantum number
m_F	kg	mass of fluid
m_{H_2O}	kg	mass of H_2O
m_P	kg	mass of particles
M	Nm	torque
$\vec{M}$	J/T m^3	macroscopic magnetization
n	1	exponent
N	Pa	normal stress difference
N	m^3/m^2	volume particle flux through area element
N_α	1	number of spins occupying state α
N_β	1	number of spins occupying state β
$\vec{N}$	m^3/m^2	volume particle flux through area element
$\vec{N}_f$	m^3/m^2	volume particle flux through area element related to interaction frequency
$\vec{N}_\eta$	m^3/m^2	volume particle flux through area element related to interaction frequency

symbol	dimension	meaning
p	Pa	pressure
p	1	exponent
$\overline{p}$	Pa	isotropic pressure
$\vec{I}$	N m s	angular momentum
$\bar{P}$	k s	mean propagator
$\vec{q}$	1/m	reciprocal space referring to displacement of spins $\vec{q} = \frac{\gamma \delta \vec{G}}{2\pi}$
$Q3$	1	cumulative frequency
r	m	radial coordinate
$\vec{r}$	m	position vector
R	m	radius of tube or capillary
$\vec{R}$	m	translational displacement
S	1	NMR signal
t	s	time
t_0	s	time $t_0 = 0s$
t_c	s	characteristic time related to wall effects
t_g	s	characteristic time related to gravity
t_P	s	duration of magnetic pulse
t_{St}	s	the time a particle with Stokes velocity u_{St} needs to cross the distance of one particle diameter $t_{St} = 2a/u_{St}$ (Stokes time)
T	K	temperature
T	1	dimensionless time
T_1	s	longitudinal relaxation time
T_2	s	transversal relaxation time including effect of inhomogenity of magnetic field $\vec{B}_0$
T_2^*	s	transversal relaxation time excluding effect of inhomogenity of magnetic field $\vec{B}_0$
u	m/s	velocity
u_P	m/s	velocity of particle (orthogonal to flow direction)
$u_{P,||}$	m/s	velocity of particle parallel to flow direction
u_{St}	m/s	Stokes velocity of particle
u_W	m/s	slip velocity
u^*	1	non-dimensional velocity
U	m/s	velocity

symbol	dimension	meaning
V	m^3	volume
$\dot{V}$	m^3/s	flow rate
$\dot{V}_S$	m^3/s	flow rate due to inner shear
$\dot{V}_W$	m^3/s	flow rate due to slip transport
x	m	volume equivalent diameter
X	m	distance (Couette flow)
y	m	position in shear gap
y^*	1	position in shear gap related to particle radius
		steady Couette flow with gravitation effect
Δy_F^*	1	layer width of pure liquid ($\varphi = 0$) if $\varphi = 1$ elsewhere
		(related to particle radius)
Δy_P^*	1	layer width of particles ($\varphi = 1$) if $\varphi = 0$ elsewhere
		(related to particle radius)
y_0^*	1	position of a particle at time $t_0 = 0$ related to particle radius
y_t^*	1	fixed position used to calculate characteristic times
Δz	m	fixed position used to calculate characteristic times

Greek Symbols

symbol	dimension	meaning
α	°	cone angle
α	1	rotation angle of magnetization
α	1	spin orientation of a spin$\frac{1}{2}$ nucleus
β	1	spin orientation of a spin$\frac{1}{2}$ nucleus
γ	Hz/T	gyromagnetic constant
γ	1	shear strain
γ_H	Hz/T	gyromagnetic constant of hydrogen
γ_T	1	shear strain related to transformed time scale
$\dot{\gamma}$	s^{-1}	shear rate (of fluid)
$\dot{\gamma}_i$	s^{-1}	inner shear rate
$\dot{\gamma}_m$	s^{-1}	macroscopical shear rate
$\dot{\gamma}_P$	s^{-1}	shear rate of particle system
$\dot{\gamma}_T$	1	shear rate related to transformed time scale
$\dot{\gamma}^*$	1	non-dimensional shear rate
$\hat{\gamma}$	1	shear amplitude
δ	1	shear angle
δ	1	phase difference
δ_{90}	m	width of boundary layer
δ_{90}^*	1	width of boundary layer related to particle radius
ϵ	1	porosity
η	Pa s	dynamic viscosity
$\langle\eta\rangle$	Pa s	average viscosity
η_0	Pa s	dynamic viscosity of the fluid
$\eta_{0,0}$	Pa s	dynamic viscosity of sugar solution
η_r	1	relative viscosity
θ	°C	temperature
λ_i	s	relaxation time
$\vec{\mu}$	J/T	nuclear magnetic moment

symbol	dimension	meaning
ϕ	m^3/m^3	particle volume concentration
ϕ_m	m^3/m^3	maximum particle volume concentration in steady Couette flow
$\Delta\phi$	1	shift angle
φ	1	relative particle volume concentration (related to particle volume maximum concentration ϕ_m
φ_0	1	relative particle volume concentration at center of gap in Couette flow ($y^* = h^*/2$)
φ_S	1	relative volume concentration of sugar crystals
φ_∞	1	relative particle volume concentration at infinite distance from the wall ($y^* \to \infty$)
φ_{max}	1	maximum relative particle volume concentration in steady Couette flow
Ψ	Pas^2	normal stress coefficient
ρ	$1/m^3$	spin density
ρ_F	kg/m^3	density of fluid
$\rho_{F,0}$	kg/m^3	density of original sugar solution
ρ_{H_2O}	kg/m^3	density of H_2O
ρ_P	kg/m^3	density of particle
ρ_S	kg/m^3	density of invert sugar in solution
$\rho_{S(solid)}$	kg/m^3	density of invert sugar
σ	Pa	normal stress
τ_0	Pa	constant shear stress
τ	Pa	shear stress
τ_F	Pa	shear yield stress
$\hat{\tau}$	Pa s	shear stress amplitude
τ_W	Pa	shear stress at wall
ω	s^{-1}	angular velocity
ω	s^{-1}	frequency
ω	s^{-1}	frequency referring to $\vec{B}_0$
ω_L	s^{-1}	Larmor frequency
ω_{RF}	s^{-1}	radiofrequency
Ω	s^{-1}	angular velocity

Mathematical Symbols, Physical Constants and Dimensionless Numbers

Mathematical Symbols

symbol	dimension	meaning
Δa	$[a]$	difference $\Delta a = a_1 - a_2$
$\langle a \rangle$	$[a]$	average value of a
$\vec{e}_i$	1	unit vector
a_i	$[\vec{a}]$	ith component of vector $\vec{a}$
x, y, z	m	cartesian coordinates
∇	1	divergence operator (nabla): $\nabla = \left(\frac{\partial}{\partial x}, \frac{\partial}{\partial y}, \frac{\partial}{\partial z} \right)$
$\mathbf{E}$	1	unit tensor
$\mathbf{S}$	Pa	stress tensor
$\mathbf{T}$	Pa	extra-stress tensor
$\imath$	1	imaginary number $\imath = \sqrt{-1}$
$\Re(c)$	$[c]$	real part of a complex number
$\Im(c)$	$[c]$	imaginary part of a complex number
$\bar{c}$	$[c]$	complex conjugate
$\mathcal{F}$	1	Fourier Transformation
$f(a) \star g(a)$	$[a][f][g]$	cross correlation

Physical Constants

$g = 9.81 \mathrm{m/s}$	gravity constant
$h = 6.626068 * 10^{-34} \mathrm{m^2\ kg/s}$	Planck's constant
$\hbar = h/2\pi$	Planck's constant divided by 2π
$k_B = 1.38066 * 10^{-23} \mathrm{J/K}$	Boltzmann constant

Dimensionless Numbers

Péclet number $Pe = \frac{\eta_0 \dot{\gamma} (2a)^3}{k_B T}$	ratio of shear stresses and brownian forces (cp. section 3.1.1)
Reynolds number $Re = \frac{\rho_F \dot{\gamma} (2a)^2}{\eta_0}$	ratio of inertia and friction (cp. section 3.1.1)

Appendix A

Phenomenological Approach

A.1 Approximation and Data from Happel and Brenner

Within the approach

$$F_\perp(y) = 6\pi a u_P \eta_0 \left(1 + A \left(\frac{a}{y} \right)^m \right)$$

it is $A = 1$ assumed. With $m = 1$ and A' derived from the data of Happel and Brenner according to

$$(F_\perp/F_{St})_{HB}(y) = 1 + A' \frac{a}{y}$$

it follows

$$A = A'(y^* \to 0) \quad .$$

Since the factor A refers to wall influence wall vicinity is relevant. The values of A' (tab. A1) show that $A'(y^* \to 0) = 1$ and thus $A = 1$ is justified. The approximation $F_\perp/F_{St} = y^{*-1} + 1$ and the data of Happel and Brenner $(F_\perp/F_{St})_{HB}$ agree (tab. A2).

A.2 Wall Effects on Particle Movements Parallel to the Flow Direction

Goldman [18] has determined the slip factor $u_P(y)/u(y)$ (u is the velocity of the fluid) at different wall distances related to particle movements parallel to the wall (ratio of the velocity of a sphere moving parallel to the wall to the

y^*	$A'(y^*)$
0.001	1.00233312
0.01	1.01896147
0.02	1.03521446
0.05	1.0792908
0.1	1.1459156

Table A.1: Values of $A'(y^*)$

y^*	$(F_\perp/F_{St})_{HB}$ from [12]	$F_\perp/F_{St} = y^{*-1} + 1$	deviation $\frac{F_\perp/F_{St} - (F_\perp/F_{St})_{HB}}{(F_\perp/F_{St})_{HB}}$
0.1	11.459156	11	4.00 %
0.1276260	9.2517663	8.835394	4.5 %
0.2	6.340886	6	5.38 %
0.5	3.205390	3	6.41 %
0.5430806	3.0360641	2.841347306	6.41 %
1	2.125536	2	5.91 %
1.3524096	1.8374749	1.73942	5.34 %
2	1.569205	1.5	4.41 %
2.7621957	1.4128629	1.362031	3.60 %

Table A.2: Comparison of approximation (3.2) and data of Happel and Brenner [12]

velocity of the fluid). As for the shear rate of the particle system we set up the approximation function

$$\dot{\gamma}_P(t, y^*) \quad = \quad \frac{\tau(t)}{\eta_0} \frac{1}{B y^{*b} + 1}$$

or in concentrated suspensions $\quad \dot{\gamma}_P(t, y^*, \varphi) \quad = \quad \frac{\tau(t)}{\eta_0} \frac{1}{B y^{*b} + (1 - \varphi)^{-2}} \quad .$

The velocity of a particle in a diluted suspension is

$$\begin{aligned} u_{P,||}(t, y^*) \quad &= \quad a \int_0^{y^*} \dot{\gamma}_P(t, \tilde{y}^*) d\tilde{y}^* \\ &= \quad \frac{\tau(t)}{\eta_0} a \int_0^{y^*} \frac{1}{B \tilde{y}^{*b} + 1} d\tilde{y}^* \end{aligned}$$

whereas the velocity function of the suspension is

$$\begin{aligned} u(t, y^*) \quad &= \quad a \int_0^{y^*} \dot{\gamma}(t, \tilde{y}^*) d\tilde{y}^* \\ &= \quad \frac{\tau(t)}{\eta_0} a y^* \quad . \end{aligned}$$

The data given by Goldman [18] valid for diluted suspensions lead to the values of b and B. Goldman has reported discrete slip velocities $\frac{u_{P,||}(y^*)}{u(y^*)}$. With (A.1) and (A.1) our approximation leads to

$$\frac{u_{P,||}}{u}(y^*) = \frac{1}{y^*} \int_{\tilde{y}^*=0}^{y^*} \frac{\tilde{y}^{*b}}{B + \tilde{y}^{*b}} d\tilde{y}^* \quad .$$

A comparison of numerically obtained values of that with the values of Goldman shows agreement if $B = 0.012$ and $b = 1$. Therewith the shear rate of the particle system is

$$\dot{\gamma}_P(t, y^*, \varphi) = \frac{\tau(t)}{\eta_0} \frac{1}{0.012 y^{*-1} + (1 - \varphi)^{-2}} \tag{A.1}$$

and the velocity is

$$\begin{aligned} u_{P,||}(t, y^*) \quad &= \quad a \int_0^{y^*} \dot{\gamma}_P(t, \tilde{y}^*) d\tilde{y}^* \\ &= \quad a \frac{\tau(t)}{\eta_0} \int_0^{y^*} \frac{1}{0.012 \tilde{y}^{*-1} + 1} d\tilde{y}^* \\ &= \quad a \frac{\tau(t)}{\eta_0} \left(y^* - 0.012 \ln(y^* + 0.012) \right) \end{aligned}$$

Taking into account additionally the wall influence on the particle movements in flow direction (3.14), (3.3) and (A.1) lead to the following diffusion equation (analogous to (3.15)):

$$\varphi \left(y^{*-1} + (1-\varphi)^{-2}\right)^{\frac{k\eta}{k_f}} = \varphi_\infty(1-\varphi_\infty)^{2\left(1-\frac{k\eta}{k_f}\right)} \left(0.012 y^{*-1} + (1-\varphi)^{-2}\right)$$

$$\Longleftrightarrow \quad \frac{\varphi \left(y^{*-1} + (1-\varphi)^{-2}\right)^{1/k}}{0.012 * y^{*-1} + (1-\varphi)^{-2}} = \varphi_\infty(1-\varphi_\infty)^{2(1-1/k)} =: K \qquad (A.2)$$

As analytical solving with $k = 0.66$ (the value of Phillips et al. [33]) is not possible we solve the equation for $k = 0.5$ and for $k = 1$ (encircling $k = 0.66$) being of the same order.

For $k = 1$ with (A.2) follows:

$$\frac{\varphi \left(y^{*-1} + (1-\varphi)^{-2}\right)}{0.012 * y^{*-1} + (1-\varphi)^{-2}} = K$$

$$\Longleftrightarrow \quad y^* = \frac{(\varphi - 0.012K)(1-\varphi)^2}{K - \varphi}$$

$$\text{and} \quad K = \varphi_\infty(1-\varphi_\infty)^{2(1-1/k)}$$

For $k = 0.5$ with (A.2) follows:

$$\frac{\varphi \left(y^{*-1} + (1-\varphi)^{-2}\right)^2}{0.012 * y^{*-1} + (1-\varphi)^{-2}} = K$$

$$\Longleftrightarrow \quad y^{*-2} + y^{*-1}\left(-\frac{0.012K}{\varphi} + 2(1-\varphi^{-2})\right) + (1-\varphi)^{-4} - \frac{K}{\varphi}(1-\varphi)^{-2} = 0$$

The physically reasonable solution of this equation with $K = \varphi_\infty(1-\varphi_\infty)^{-2}$ is:

$$y^{*-1} = \frac{0.012K}{2\varphi} - (1-\varphi)^{-2} + \sqrt{\frac{0.012^2 K^2}{4\varphi^2} + (1-\varphi)^{-2}\frac{K}{\varphi}(1-0.012)}$$

$$\Leftrightarrow \quad y^* = \left(\frac{0.012K}{2\varphi} - (1-\varphi)^{-2} + \sqrt{\frac{0.012^2 K^2}{4\varphi^2} + (1-\varphi)^{-2}\frac{K}{\varphi}(1-0.012)}\right)^{-1}$$

A Comparison with the results not taking into account wall influence on particle movements in flow direction setting $k = 1$ and $k = 0.5$ shows that the profiles differ only slightly (fig. A1). So disregard of this influence is justified most probably also if $k = 0.66$. Consistently figure A2 shows that the effect of the wall on the force acting on a particle moving orthogonal to the wall ($F_\perp$) is much stronger than on the force acting on a particle moving parallel to the wall ($F_\parallel$).
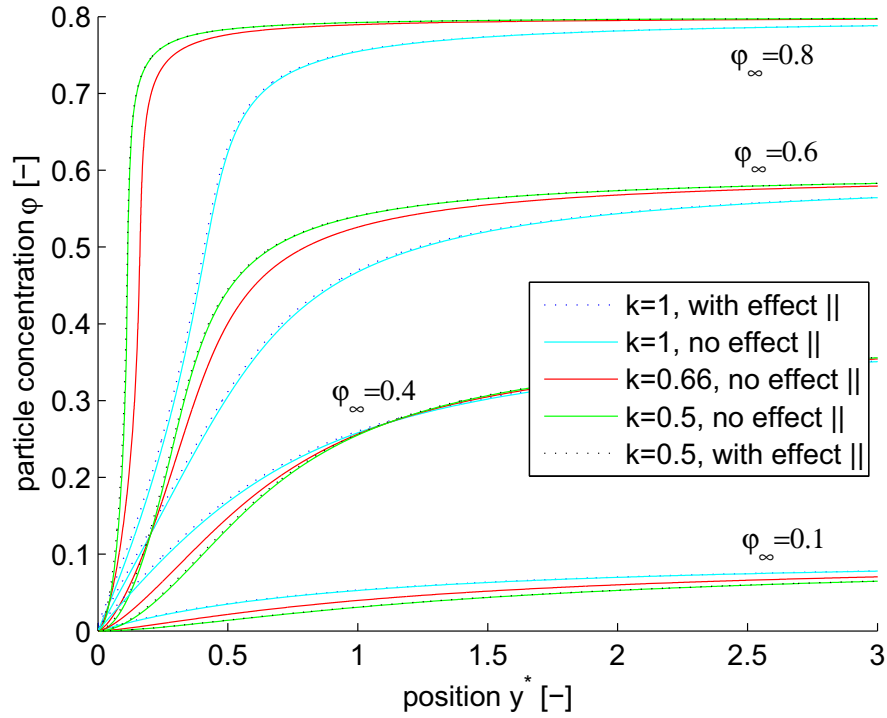
Figure A.1: Particle concentration profiles in a steady half-infinite shear flow with and without taking into account the wall influence on particle movements parallel to flow direction (in legend denoted as 'effect ||')
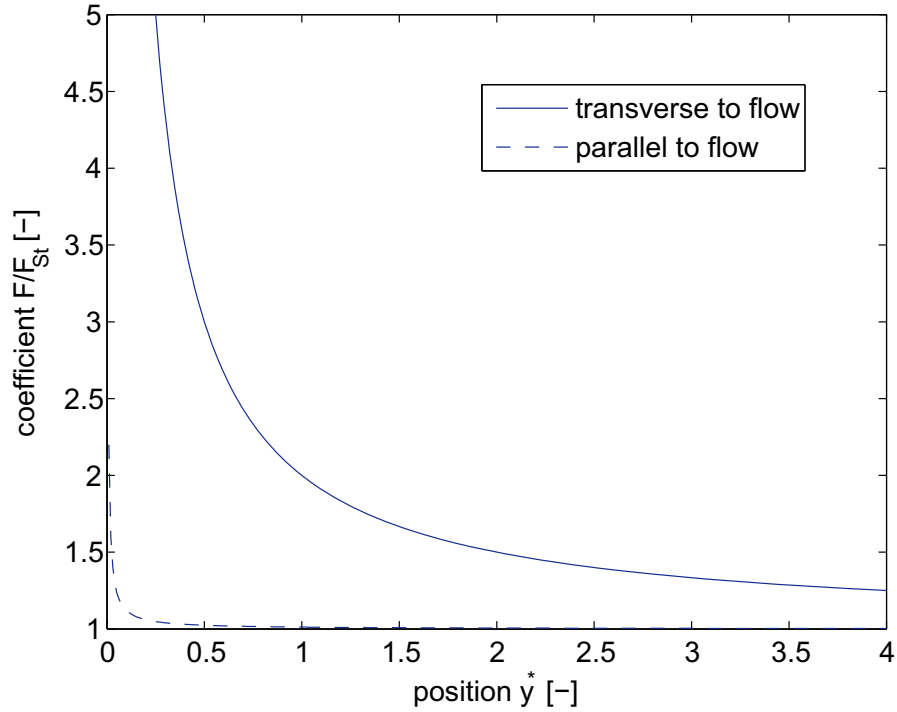
Figure A.2: The wall influence on the force acting on a particle moving orthogonal $(F_\perp)$ and parallel $(F_{||})$ to the wall

Thus the particle concentration profiles and the velocity profiles taking into account velocity slip should correspond approximately to the results excluding velocity slip and we conclude that leaving it out will not produce significant errors.

Appendix B

Properties of Shear Flowing Suspensions

B.1 Dependency of the Particle Concentration Profile on the Diffusion Factors

The ratio of the diffusion constants $k = k_\eta/k_f$ that was determined by Phillips et al as $k \approx 0.66$ influences the resulting particle concentration profiles according to the diagram in fig. B.1 (no gravity effect, one wall). At the intersection point $y^* \approx 1.2$ and $\varphi \approx 0.27$ the particle concentration does not change if one of the two diffusion factors k_η and k_f changes. Since the corresponding particle fluxes N_η and N_f increase linearly with the diffusion factors ($N_f \propto k_f$ and $N_\eta \propto k_\eta$ according to (2.8) and (2.12)) the particle fluxes both must be zero at this position.

B.2 Numerical Determination of Velocity Profiles from Discrete Data

According to (3.17) the velocity profile is calculated from discrete data triples $(y_i^*, \dot{\gamma}_i, \varphi_i)$:

$$u_i(y_i^*) = \frac{y_2^* - y_1^*}{2}\dot{\gamma}_1(\varphi_1(y_1^*)) + \sum_{j=2}^{i-1} \dot{\gamma}_j(\varphi_j(y_j^*))\frac{y_{j+1}^* - y_{j-1}^*}{2} + \frac{y_i^* - y_{i-1}^*}{2}\dot{\gamma}_i(\varphi_i(y_i^*))$$

(Mostly $y_1^* = 0$.)
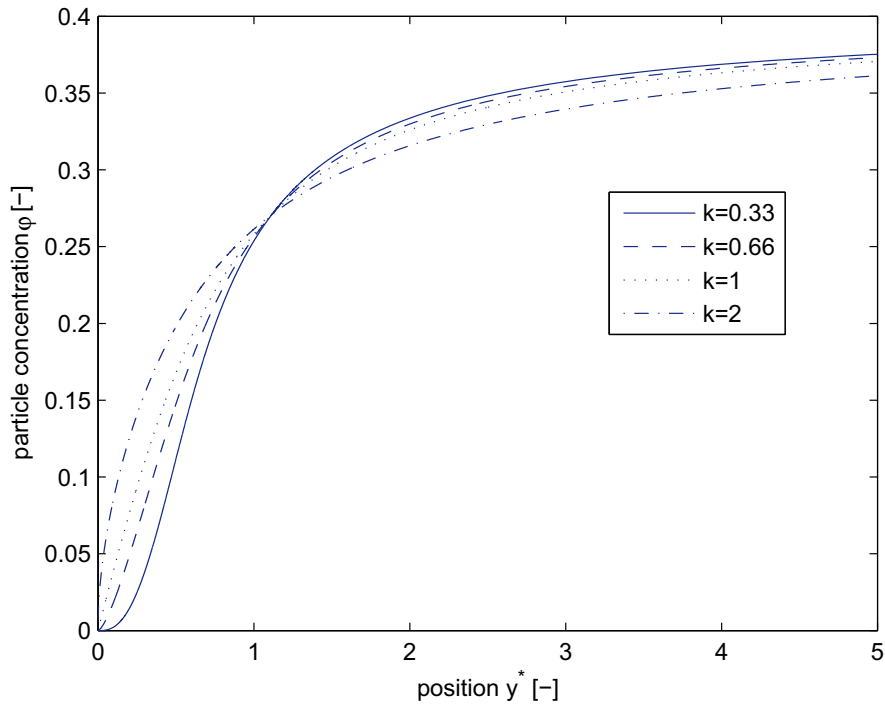
Figure B.1: Particle concentration in a steady half-infinite shear flow (one wall) without gravity effect at $\langle \varphi \rangle = 0.4$ and $\frac{\tau_0}{\eta_0} = 1\mathrm{s}^{-1}$ varying the diffusion factor k

Appendix C

Experimental Investigation

C.1 Calculating Suspension Properties

We assume that the densities respectively the specific volumes in the sugar solution are linearly superpositionable.

Density of Dissolved Invert Sugar

The density of invert sugar in solution ρ_S is calculated from the density of the original solution $\rho_{F,0} = 1.39\text{g/cm}^3$ and its mass concentration $c_{S,0} = 72.7\%$:

$$
\begin{aligned}
c_{S,0}\rho_S^{-1} + (1 - c_{S,0})\rho_{H_2O}^{-1} &= \rho_{F,0}^{-1} \\
\Leftrightarrow \rho_S &= \left(\rho_{F,0}^{-1} - (1 - c_{S,0})\right)^{-1} c_{S,0}
\end{aligned}
$$

With $\rho_{H_2O} = 1\text{g/cm}^3$ it results $\rho_S = 1.59\text{g/cm}^3$. (The density of invert sugar (solid state) found in literature gives $\rho_{S(solid)} = 1.65\text{g/cm}^3$).

Average Particle Concentration, Density and Sugar Concentration of Sugar Solution after Evaporating

Water (mass m_{H_2O}) is evaporated from a 72.7% sugar solution (mass m_F) containing or not containing particles. The new sugar concentration c_S is calculated as

$$
\begin{aligned}
m_F c_{S,0} &= (m_F - m_{H_2O})c_S \\
c_S &= m_F \left(1 - \frac{c_{S,0}}{c_S}\right)
\end{aligned}
$$

relative signal difference	$d = \frac{I_{wall\,area} - I_{axis\,area}}{I_{average}}$ [1]
Solution after shearing	0.4
Suspension after shearing (> 1 min)s	0.75
Suspension after shearing (30 min)	1.1

Table C.1: The relative signal differences d of a suspension and of a pure solution after shearing

and the new density ρ_F as

$$\begin{aligned} \rho_F^{-1} &= \rho_S^{-1} c_S + \rho_{H_2O}^{-1}(1 - c_S) \\ \rho_F &= \left(\rho_S^{-1} c_S + \rho_{H_2O}^{-1}(1 - c_S)\right)^{-1} \qquad . \end{aligned}$$

(As the particles had to be added before evaporating a determination of density using a density hydrometer was not possible.)
The following average particle (volume) concentration results:

$$\langle \phi \rangle = \frac{m_P \rho_P^{-1}}{m_P \rho_P^{-1} + m_F \rho_{F,0}^{-1} - m_{H_2O} \rho_{H_2O}^{-1}}$$

C.2 Comparison of the NMR Data in a Suspension and in a Pure Sugar Solution

In order to determine if the signal difference in the magnetic resonance image of a suspension after shearing (fig. 4.4) is representing a demixing of the suspension indeed a relative signal difference is defined (I is the intensity of the NMR signal):

$$d = \frac{I_{wall\,area} - I_{axis\,area}}{I_{average}}$$

The relative signal difference of a suspension after shearing is compared to that of a pure solution after shearing (fig. C.1, tab. C.1). The relative signal difference of a pure solution is considerably lower than the one of a suspension. This suggests that the signal difference in the suspension is the result of a demixing at least partially.
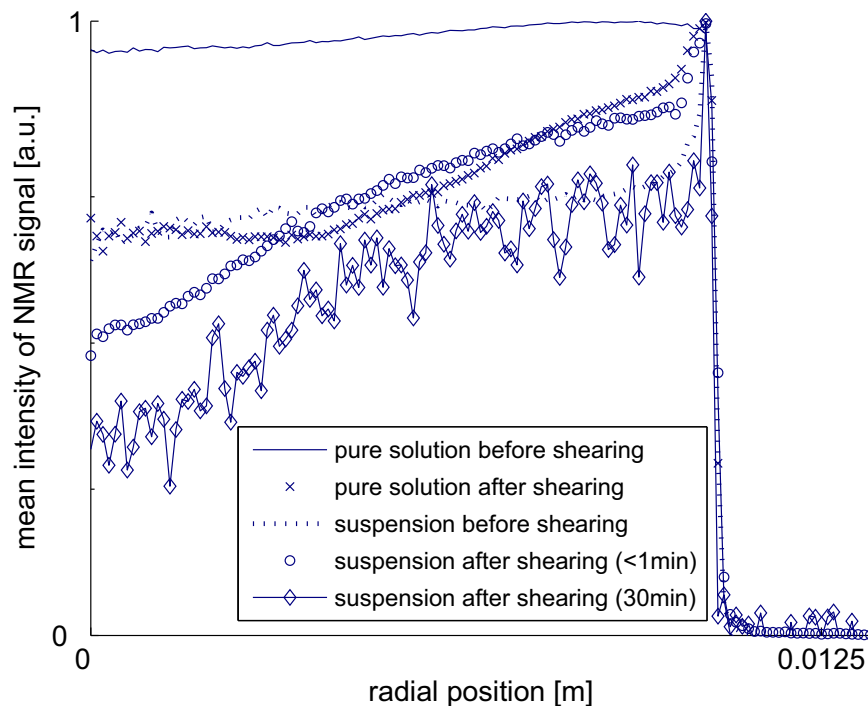
Figure C.1: Intensity of the NMR signal of a suspension and of a pure sugar solution before and after shearing

C.3 The RheoScope

C.3.1 The Device

To perform rheological and optical investigation of a suspension we used a special optical torsion rheometer of the company Thermohaake (fig. C2). The ′RheoScope′ is a modified version of the ′RheoScope 1′. Operating the RheoScope for instance as a cone plate or a parallel plate rheometer the usual types of rheological shear tests including shear stress and shear rate controlling are possible. The special feature of the RheoScope is the ability of realizing simultaneous rheological and optical measurements. The optical set up allows the production of snapshots as well as the recording of videos of the filled-in substance. The lower plate is transparent and covers an optical system. The display window is $920 \times 685 \mu$m wide. Its position can be

varied within a radial length of 18mm starting at the centre. The depth of focus is variable whereas the focus reference point is fixed. The RheoScope is controlled through the software 'Rheowin' provided by Thermohaake. It allows data processing ('Data Manager') as well as designing of chronologically structured measuring procedures ('Job Manager') combining several elements specifying rheological measurements, optical recording and general functions like lift control or data output. For further data on the RheoScope look at the instruction manual of the RheoScope [20].

Figure C.2: The RheoScope

C.3.2 Theoretical Description of the Shear Flow in the RheoScope

We choose a parallel plate setup. A plane Couette flow is assumed neglecting horizontal flow due to shear rate gradients in radial direction. After one rotational turn the particles are redispersed in the circumferential direction [27] and the particle concentration is not a function of the $x-$coordinate that is flow direction. The differing local shear rates are with (2.2) and (2.3):

$$\dot{\gamma}(y^*, r) = \frac{\tau(r)}{\eta(\varphi(y^*, r))} = \frac{\tau(r)}{\eta_0}(1 - \varphi(y^*, r))^2$$

(If performing shear rate controlled tests the set shear rate $\dot{\gamma}(r) = r\frac{\omega}{h}$ is 'distributed' across the shear gap so that the resulting local shear stress values $\tau(r)$ fulfill torque balance.) The viscosity value registered by the Rheoscope is a function of the particle distribution and therefore might give indications concerning demixing processes. Due to the curved streamlines at high shear rates centrifugal forces act on the particles. As the centrifugal forces are maximum at the rotating upper plate and zero at the fixed lower plate the particles near the upper plate are pushed outward and a current away from

the center is generated under the upper plate. At the center the resulting low pressure makes fluid flow upwards. That in turn causes flow inwards above the lower plate. In this way a circular secondary flow is generated. As we deal with low shear rates the centrifugal forces are weak and will not disturb the Couette flow. Curved streamlines also cause a particle drift across flow direction. According to Shauly et al. [3] the drift is directed towards decreasing curvature. At polydisperse particle distribution bigger particles are to be found at the outer areas of the flow, smaller particles tend to be situated within the interior zone (Altobelli et al. [19]). A particle drift out of the gap due to a shear rate step at the circumference analogous as described in [27] might occur. The last effects are not relevant here as this is not the drift direction to be investigated.

C.3.3 The Rheoscope Does not Meet our Demands Perfectly

The RheoScope is not entirely appropriate for determining particle distributions in suspensions due to deficits of the optical system. Figs. C.3 and C.4 show images recorded by the RheoScope at different depth of focus.
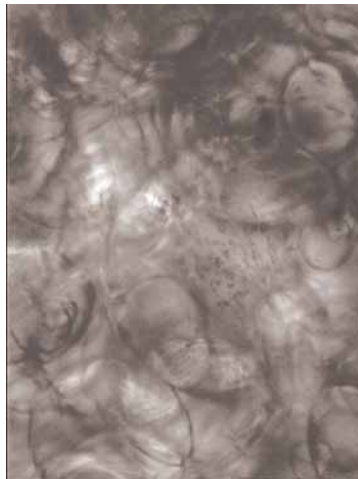
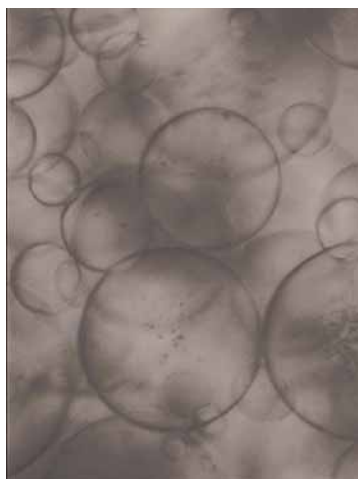Figure C.3: Image of the suspension during shearing at high depth of focus

Figure C.4: Image of the suspension during shearing at low depth of focus

First of all even in combination with our optimized particle-fluid system and a polished plate the entry of light is not sufficient by far. This makes automatic image processing difficult as most image processing tools operate with the distinction of different gray scales these being barely distinguishable within images recorded the RheoScope. As explained more detailed in [8] a different illumination principle would make the optical recordings significantly clearer and therefore much easier to analyze. Another disadvantage of the optical set up is the fixed point of focus whereas the depth of focus can be varied. Especially with regard to the fact that our intentions include the analysis of particle concentration distributions requiring optical recordings at different axial positions this means a drastic limitation. The construction of the RheoScope easily would have allowed the integration of a translational mobile objective. Further the low size of the observation window restricts the possibilities of statistical image processing extremely. The images display most particles incompletely and a great number of those images would be needed to provide a statistical reliability.

C.4 Shear Tests

C.4.1 Optical Test Measurements

Hartmann [22] tested the RheoScope first. Bender [8] conducted further experiments and found that a particle depletion in a shear plane near the wall is not excluded. Due to the fixed observation plane he could not investigate other planes. For a more detailed description of these measurements see [22] and [8]. The installing of an improved optical system as proposed in [8] was not possible here. Due to the given time frame only the rheological side was pursued.

C.4.2 Conceptual Design of the Experiments

Due to device-specific reasons all measurements were conducted shear rate controlled to guarantee creeping flow. The determination of the exact shear rates during the start-up of shear stress controlled experiments was problematic. The particle size of PMMA provides high Péclet numbers what justifies excluding the Brownian motion (cp. section 3.1.1). The particle concentration is to be high enough in order to provide a sufficient amount of interactions related to a reasonable time scale. Shear tests with different shear rates, total particle concentrations, gap widths and matrix viscosities (fluid densities) were performed. Mostly PMMA was used possessing its

original distribution. A small amount of PMMA of a narrowed distribution containing only particles with radii from 150 to 300μm was available as well (obtained before sieve was irreversibly clogged).

In general shear tests featuring different shear rates may allow to find out if the diffusion-controlled particle distribution correlates with the shear strain solely but not with the shear rate as predicted by the theoretical model (section 3.1.2). The particle drift due to gravity is not related to the shear strain, though. Variation of the shear rate additionally involves variation of the centrifugal forces helping to decide if they are irrelevant as assumed before. Variation of the fluid density and thus the matrix viscosity influence the time scale regarding gravity effect. The viscosity registered by the Rheo-Scope being a function of the particle distribution may show a short term viscosity increase due to homogenizational processes [27] and further effects caused by demixing due to wall and gravity.

C.4.3 Experimental Setup

Operating the RheoScope as a parallel plate rheometer a polished plate of platinum with a diameter of 60mm was chosen as a sensor. An aluminium ring screwed on the glass plate was used to prevent the suspension from flowing away. Also it was necessary to put a plexiglass plate on the aluminium ring to avoid further evaporating causing undesirable concentration and viscosity changes.

The typical steps of a measurement with the RheoScope are (chronological order):

- preparation of suspension

- setting the gap width control ('zero point determination')

- filling in suspension

- positioning of upper plate

- starting previously defined job controlling shear test with optical recording and saving data

- analysis of the suspension in shear volume (for example to determine $\langle\varphi\rangle$) (upper plate does not cover the whole suspension volume)

- analysis of image date

- analysis of rheological data

C.4.4 Results

Exemplarily we show the measured viscosity functions at shear rate $\dot{\gamma}_m = 0.1\text{s}^{-1}$ and gap width $h^* = 30$ of a suspension with sugar concentration $c_S = 88\%$ ($\rho_F = 1.45\text{g/cm}^3$) and average particle concentration $\langle\varphi\rangle = 0.4$ (figs. C.5 and C.6) as well as the viscosity of a 88% sugar solution without particles (fig. C.7). (At certain times the data was taken more frequently in

Figure C.5: Viscosity of 88% sugar solution with average particle concentration $\langle\varphi\rangle = 0.4$ at $\dot{\gamma} = 0.1\text{s}^{-1}$ measured by the RheoScope

order to investigate the viscosity development at a short time scale (visible in figs. C.6 and C.7)). The measured viscosities $\langle\eta_{0,88}\rangle \approx 42\text{Pas}$ (pure fluid), $\langle\eta\rangle \approx 90\text{Pas}$ (suspension) approximately relate with equation (2.3). Due to the high sensitivity of the viscosity of the matrix fluid regarding sugar concentration although the concentration is known approximately the viscosity is not. As the particles are added during the process of concentration adjustment the exact matrix viscosity of the suspension cannot be determined experimentally. Using the measured data of the stationary suspension viscosity it is calculated from (2.3) as $\eta_0 \approx 32.4\text{Pas}$. The characteristic times calculated according to section 3.2.4 are $t_c = 218\text{s}$ and $t_g = 311\text{s}$. According to section 4.2.2 the viscosity of a non-homogenous suspension decreases with increasing inhomogenity of the particle distribution. Thus the initial increase of the viscosity function till the maximum at $t \approx 2500\text{s}$ (fig. C.6) overlayed
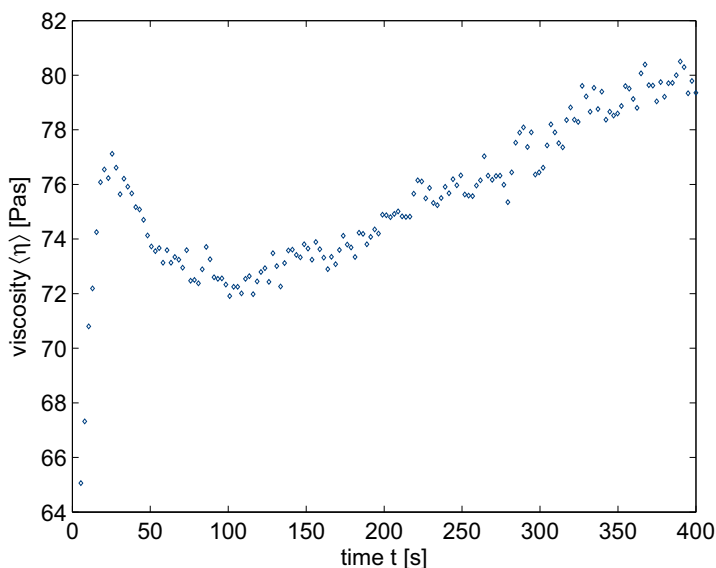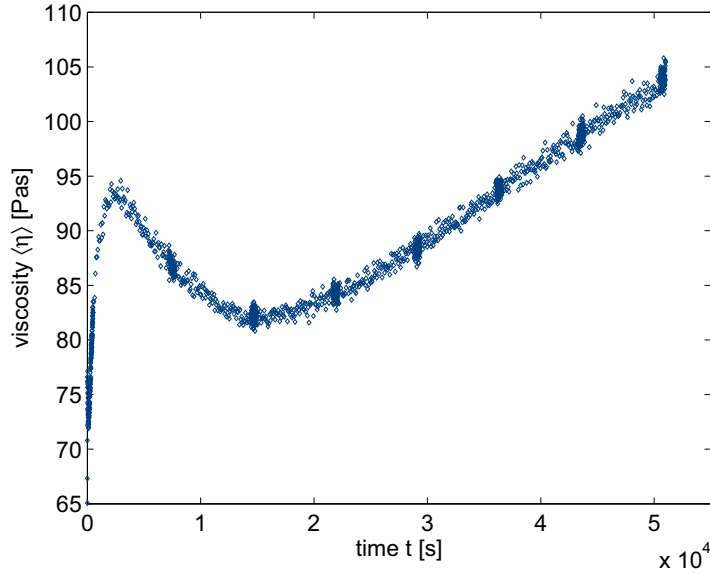
Figure C.6: Viscosity of 88% sugar solution with average particle concentration $\langle\varphi\rangle = 0.4$ at $\dot{\gamma} = 0.1$ s^{-1} measured by the RheoScope

by a slight decrease at the very beginning of the shear test at $t \approx 100$s (start-up time range enlarged in fig. C.5) might correspond to the short-term viscosity increase due to homogenizational processes described in [27] and the demixing at the wall lowering the viscosity. The following decrease suggests a further demixing possibly due to gravity drift. A rough estimation of the time taking a particle to cross the distance from the wall to the phase boundary at steady state (with (3.9)) gives

$$t = \langle\varphi\rangle h^* u_{St} \approx 8000\text{s}$$

The order of magnitude is in line with the data in fig. C.6. The final slightly upward tendency most probably is due to evaporation or to the crystallization of sugar. In contrast the shear test of the pure sugar solution (fig. C.7) shows no decline of the viscosity and no decrease at the beginning supporting our assumptions.
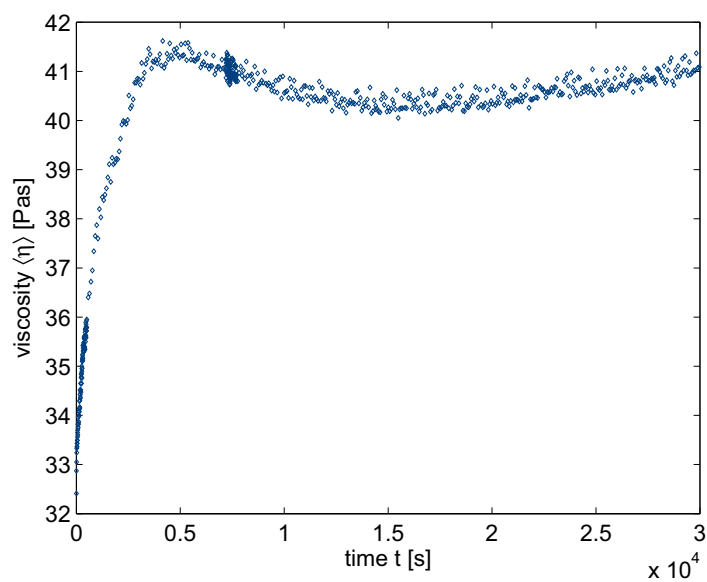
Figure C.7: Viscosity of pure 88% sugar solution at $\dot{\gamma} = 0.1\mathrm{s}^{-1}$ measured by the RheoScope

C.5 Evelution of the NMR Signal Data (Matlab Code)

C.5.1 Simulation of the Spin Density Distribution of a Suspension in a Tube

```
C:\Programme\MATLAB701\work\calc_dens.m                        Page 1
16. Februar 2006                                              16:19:44


% calc_dens distributes hard discs (squares) in a plane(random
% distribution)
%
% Usage:        dens = calc_dens(spaceSize,radius);
%
% spaceSize      =    räumliche Diskretisierung
% radius         =    "Kugel"-Radius in m


%=========================================================================
%
%  Name:         calc_dens.m
%
%  Author:       Silke Muckenfuss and Edme H. Hardy
%  Date:         2005/02/23
%
%  Modifications on 2005/00/00 by EH:
%
%  Bugs, suggestions, remarks: Kugelform besser nähern, Dichte
%  kontrollieren, Radienverteilung, räumliche Verteilung, Porosität vorgeben ...
%
%=========================================================================


function [dens] = calc_dens(spaceSize,radius)

FOV=.025; %Sichtfenster in m
ID=.020; %Rohrinnendurchmesser in m
radius=round(radius*spaceSize/FOV)
porosity=0.98
maxIt=1e5; %maximale Zahl von Iterationen, ggf erhöhen, falls Porosität nicht↙
erreicht
if radius<=0
    disp 'Der Radius ist zu klein für die räumliche Diskretisierung'
    dens=0;
    return
end

dens=zeros(spaceSize);
count=0;

leftLimit=(FOV-ID)/2; %Linker Rand in m
leftLimit=max(round(leftLimit/.025*spaceSize),1) %Linker Rand in Space-Einheiten >0
rightLimit=spaceSize-leftLimit %< spaceSize

dens(:,leftLimit:rightLimit)=1;
totVol=sum(sum(dens)); %Gesamtfläche im Rohr
solidVol=(1-porosity)*totVol; %Gesamtkugelfläche
maxNumber=round(solidVol/(2*radius+1)^2);


for n=1:maxIt %maximale Anzahl von Versuchen
    x=round(rand(1)*spaceSize); %random x coordinate
    y=round(rand(1)*spaceSize); %random y coordinate
```

```matlab
    if (x-radius>0)&(x+radius<=spaceSize)&(y-radius>0)&(y+radius<=spaceSize)
        if sum(sum(dens(x-radius:x+radius,y-radius:y+radius)))==(2*radius+1)^2
            dens(x-radius:x+radius,y-radius:y+radius)=0;
            count=count+1;
            if count==maxNumber
                disp 'kodierte Porosität ist erreicht'
                break
            end
        end
    end
end
count
```

C.5.2   Simulation of the NMR Signal

```
C:\Programme\MATLA...\SilkePhaseReadGradEcho2D_sag_spheres.m        Page 1
16. Februar 2006                                                  16:54:18
```

```matlab
%  Simuliert die Datenaufnahme nach unterschiedlichen
%  Phasengradienten unter einem Lesegradienten-Echo
%
%  Usage:      [orig,rawData]=SilkePhaseReadGradEcho2D_sag_spheres;
%  orig ist die berechnete (zufällige) Verteilung
%  rawData ist das Ergebnis einer idealen Messung (Rohdaten, für
%  Darstellung abs(fftshift(fft2(rawData)))).
%


%=========================================================================
%
%  Name:        SilkePhaseReadGradEcho2D_sag_spheres.m
%
%  Author:      Edme H. Hardy
%  Date:        2004/04/14
%
%  Modifications on 2005/02/25 by EH: Graphikausgabe und fft
%  herausgenommen, Ausgabe in Dateien
%               on 2004/00/00 by
%
%  Ruft calc_dens auf
%
%  Bugs, suggestions, remarks:
%  Ausgangssituation: Schnitt durch ein Rohr. Innerhalb einer
%  Schicht sind nach einem idealen pi/2-Puls alle Magnetisierungsvektoren
%  entlang der x-Achse des rotierenden Koordinatensystems.
%
%  Bemerkung:
%  Rechenzeit mit spaceSize=100 und MTX=64
%  Auf mvme129 (PentiumIII 733 MHz 512 Mb Win2000 SP4) 64 Sekunden
%  Auf mvme126 (AMD Athlon x GHz 5xy Mb Win2000) 40 Sekunden
%  Auf mvme5 (Pentium m4 2 GHz 512 Mb Win2000 SP4) 31 Sekunden
%
%=========================================================================

function [dens,rawData]=SilkePhaseReadGradEcho2D_sag_spheres;

tic

%Wichtiger experimenteller Parameter:
MTX = 256 %Größe der Bildmatrix
spaceSize = 700 %räumliche Diskretisierung, i.A. ungleich Bildmatrixgröße MTX↙
(größer!)
dens = calc_dens(spaceSize,0.00007); %Spindichte für Marvin
if dens==0 %Falls Marvin-Spindichte versagt
    dens=0;
    rawData=0;
    return
end
%Erzeugung einer Matrix mit ideal gleichmäßigen Magnetisierungsbeträgen
%innerhalb eines Kreises (Spindichte):
%spaceSizeHalf = spaceSize/2; %used in spin density loop
%sqRadius = (0.88*spaceSize/2)^2; %Quadrat des Reagenzglasradius  %Rohr ist↙
```

```
C:\Programme\MATLA...\SilkePhaseReadGradEcho2D_sag_spheres.m      Page 2
16. Februar 2006                                            16:54:39
```

```
dünner!!!!!!!SILKE
%Radius = 0.88*spaceSize/2; %Radius wird benötigt wegen Sag.-Schnitt SILKE
%dens = zeros(spaceSize,spaceSize); %Initialisierung der Spindichte mit Null
%for x = 1:spaceSize; %Hier ist x noch nicht in einer Längeneinheit
%   for y = 1:spaceSize; %Hier ist y noch nicht in einer Längeneinheit
 %       if (y < (spaceSizeHalf+Radius)) & (y > (spaceSizeHalf-Radius)) %neue↙
Aufteilung Sag.-Schnitt! SILKE
  %            dens(y,x)=1;
   %     end
  % end
%end


%Berechnung von Phasen- und Lesegradienten aus den experimentellen Parametern
FOV = 0.025  %Sichtfeld in m
SWH = 101010 %Bandbreite in Hz = Samplingrate
DW = 1/SWH; %"dwell time" = Samplingintervall
gammaGx=2*pi*SWH/FOV; %Lesegradient mal dem gyromagnetischem Verhältnis
Gx=gammaGx/2.675e8  %Lesegradient in T/m für die Bildschirmausgabe
gammaDeltaGy_delta = 2*pi/FOV;  %gamma x Phasengradienteninkrement mal Dauer,
                                %aus FOV = 2pi / k-Inkrement

%matrix oriented definitions
yMat = zeros(spaceSize,spaceSize);
for n=1:spaceSize
    yMat(n,:)=-FOV/2 + n*FOV/spaceSize;  %Matrix mit den y Koordinaten der Raumpunkte
end                                      %Beachte: y entspricht 1. Index
xMat = zeros(spaceSize,spaceSize);
for m=1:spaceSize
    xMat(:,m)=-FOV/2 + m*FOV/spaceSize;  %Matrix mit den x Koordinaten der Raumpunkte
end                                      %Beachte: x entspricht 2. Index

%Zunahme der Magnetisierungsphase durch den Lesegradienten während einer
%"dwell time":
readPhaseInc=gammaGx*xMat*DW; %spaceSize-Matrix, wie xMat

tE = MTX*DW  %Dauer der Datenaufnahme, bei Echoexperiment u.U. gleich Echozeit

%Definition des Ausgangszustandes für die Phasen:
phase = zeros(spaceSize,spaceSize); %Erst sind alle Magnetisierungsvektoren entlang x

echoR = zeros(MTX,MTX); %Initialisiere Realteil des "Echos"
Mr = zeros(spaceSize,spaceSize); %Initialisiere Magn.-Realteil an allen Raumpunkten
echoI = zeros(MTX,MTX); %Initialisiere Imaginärteil des "Echos"
Mi = zeros(spaceSize,spaceSize); %Initialisiere Magn.-Imagteil an allen Raumpunkten

%Simulation der Spindynamik während des Experimentes
echoR(:,:)=nan; %für eine schönere Darstellung während der Messung
echoI(:,:)=nan; %für eine schönere Darstellung während der Messung
for n=1:MTX  %Phasen-Schleife, experimentell jeweils nach der "repetition time"
    phase = (n-MTX/2)*gammaDeltaGy_delta*yMat; %Setzen der y-abhängigen Phase,
    %beginnend mit dem kleinsten Wert (negativ, d.h. größter Betrag)
    phase=phase-readPhaseInc*MTX/2;  %Lese-Kompensationsgradient, Dauer=Lesezeit/2
    for t=1:MTX %Daten-Leseschleife, Einheit der Zeit in readPhaseInc enthalten
```

```
C:\Programme\MATLA...\SilkePhaseReadGradEcho2D_sag_spheres.m     Page 3
16. Februar 2006                                              16:55:02
```

```
        Mi=dens.*sin(phase); %Magnetisierungsimaginärteil an jedem Raumpunkt
        echoR(n,t)=sum(sum(Mr)); %Signalrealteil ist Summe alle Magnetisierungs-
                                 %Realteile
        echoI(n,t)=sum(sum(Mi)); %Signalimagteil ist Summe alle Magnetisierungs-
                                 %Imagteile
        phase=phase+readPhaseInc; %Phasen werden für das Samplingintervall
                                  %inkrementiert
    end
end

rawData=echoR+i*echoI; %Spektrum/Bild

firstPart1='rawData_';
firstPart2='orig_';
namePart=datestr(now,'yymmdd_HHMMSS');
name1=[firstPart1, namePart]
name2=[firstPart2, namePart '.mat']
save 'rawData' rawData
save 'dens' dens

toc
```

C.5.3 Analysis of the NMR Data

```
% shearCalc evaluates shear rates from 1D sevi data. Rohdaten liegen in
% /opt/data/Z/nmr/sm_050718.Bei den Daten in diesem Verzeichnis wurde die
% Temperatur am UWK auf 23 Grad Celsius gestellt, Raumtemperatur ca 26 Grad
% Celsius. Weitere Rohdaten liegen in /opt/data/Z/nmr/sm_050629. Für diese
% war der UWK auf 17 Grad Celsius gestellt.
%
% Usage:  [] = shearCalc(fname);
%


%========================================================================
%
%  Name:        shearCalc.m
%
%  Author:      EH / SM
%  Date:        2005/07/20
%
%  Modifications on 2005/07/20 by EH: Festlegung auf Auswertung mit
%  Rohdaten, beide Varianten unter shearCalcAlt
%
%  Bugs, suggestions, remarks: check threshold influence, Rohr ist nicht
%  ganz zentriert, ausserdem ist der Scheitel des Strömungsprofils nicht in
%  der Rohrmitte. Bereich für die v-Auswertung beachten. Axis für Visko
%  noch von Hand.
%
%========================================================================


function [] = shearCalc(fname);

g=9.81;         %Erdbeschleunigung in m/s**2
h=.24;          %Höhendifferenz für eine Stufe
L=12;            %Gesamtlänge der Flussstrecke für Delta_p / L
rho=1300;       %Dichte der Zuckerlösung in kg/m**3
dp_2LpS=rho*g*h/2/L;   %Druckverlust pro Stufe
dpV=dp_2LpS; %ca Berücksichtigung von Verlusten
FOV=25; %Field of View in mm, hier für alle gleich!
printOpt=0;

spaceMTX=512;
flowMTX=64;
FOF=16;

%------------------------------------------------------------------------
fname='fid0629_198'; %Fünf Stufen Höhenunterschied
dp_2L=5*dp_2LpS-4.4*dpV;   %Druckverlust
[dens198,velo198,rAx198]=rawVeloCalc(fname,spaceMTX,flowMTX,FOF,FOV);
[shearRate198]=shearRateCalc(velo198,rAx198);
[eta198,phi198,shearStress198]=...
    etaPhiCalc(shearRate198,dp_2L,rAx198);
%------------------------------------------------------------------------
fname='fid0629_201'; %Sechs Stufen Höhenunterschied
dp_2L=6*dp_2LpS-5.4*dpV;   %Druckverlust
[dens201,velo201,rAx201]=rawVeloCalc(fname,spaceMTX,flowMTX,FOF,FOV);
```

```
[shearRate201]=shearRateCalc(velo201,rAx201);
[eta201,phi201,shearStress201]=...
    etaPhiCalc(shearRate201,dp_2L,rAx201);
%-------------------------------------------------------------------------
fname='fid0629_203'; % Acht Stufen Höhenunterschied, andere Gradententemp.
dp_2L=8*dp_2LpS-6.7*dpV;   %Druckverlust
[dens203,velo203,rAx203]=rawVeloCalc(fname,spaceMTX,flowMTX,FOF,FOV);
[shearRate203]=shearRateCalc(velo203,rAx203);
[eta203,phi203,shearStress203]=...
    etaPhiCalc(shearRate203,dp_2L,rAx203);
%-------------------------------------------------------------------------
fname='fid0629_205'; % Zwei Stufen Höhenunterschied, andere Gradententemp.
dp_2L=2*dp_2LpS-dpV;   %Druckverlust
[dens205,velo205,rAx205]=rawVeloCalc(fname,spaceMTX,flowMTX,FOF,FOV);
[shearRate205]=shearRateCalc(velo205,rAx205);
[eta205,phi205,shearStress205]=...
    etaPhiCalc(shearRate205,dp_2L,rAx205);
%-------------------------------------------------------------------------
fname='fid0718_2'; %Acht Stufen Höhenunterschied
dp_2L=8*dp_2LpS-dpV;   %Druckverlust
[dens2,velo2,rAx2]=rawVeloCalc(fname,spaceMTX,flowMTX,FOF,FOV);
[shearRate2]=shearRateCalc(velo2,rAx2);
[eta2,phi2,shearStress2]=...
    etaPhiCalc(shearRate2,dp_2L,rAx2);
%-------------------------------------------------------------------------
fname='fid0718_4'; %Vier Stufen Höhenunterschied
dp_2L=4*dp_2LpS-3.6*dpV;   %Druckverlust
[dens4,velo4,rAx4]=rawVeloCalc(fname,spaceMTX,flowMTX,FOF,FOV);
[shearRate4]=shearRateCalc(velo4,rAx4);
[eta4,phi4,shearStress4]=...
    etaPhiCalc(shearRate4,dp_2L,rAx4);
%-------------------------------------------------------------------------
fname='fid0718_5'; % Drei Stufen Höhenunterschied
dp_2L=3*dp_2LpS-2.85*dpV;   %Druckverlust
[dens5,velo5,rAx5]=rawVeloCalc(fname,spaceMTX,flowMTX,FOF,FOV);
[shearRate5]=shearRateCalc(velo5,rAx5);
[eta5,phi5,shearStress5]=...
    etaPhiCalc(shearRate5,dp_2L,rAx5);
%-------------------------------------------------------------------------

figure(1) %Spindichten -> Partikelvolumenkonzentration für verschiedene↙
Geschwindigkeiten
plot(rAx205,dens205/max(dens205),'y.-')
hold on;
% plot(rAx2,dens2/max(dens2),'k.-')
plot(rAx5,dens5/max(dens5),'c.-')
plot(rAx4,dens4/max(dens4),'g.-')
plot(rAx198,dens198/max(dens198),'m.-')
plot(rAx201,dens201/max(dens201),'r.-')
plot(rAx203,dens203/max(dens203),'b.-')
hold off;grid, axis tight
title('Spindichte bei Stufen: 2 (stehend?) (y), 3 (c), 4 (g), 5 (m), 6 (r), 8↙
(blue)')
```

```
ylabel('spin density / arb. units')
if printOpt==1
    set(1,'PaperPosition',[0.63 6.3 15 10])
    print -dtiff -r300 spinDensity
end

figure(2) %v-Profile für verschiedene Geschwindigkeiten
vmin=min([velo198 velo201 velo203 velo205 velo2 velo4 velo5]);
plot(rAx5,velo5,'c.-') %3
hold on;
plot(rAx4,velo4,'g.-') %4
plot(rAx198,velo198,'m.-') %5
plot(rAx201,velo201,'r.-') %6
plot(rAx203,velo203,'b.-') %8
% plot(rAx205,velo205,'y.-') %2
% plot(rAx2,velo2,'k.-') %8
hold off;grid, axis([-11 11 vmin 0])
title('Geschwindigkeit bei Stufen:  3 (c), 4 (g), 5 (m), 6 (r), 8 (blue)')
xlabel('r / mm')
ylabel('v / mm/s')
if printOpt==1
    set(2,'PaperPosition',[0.63 6.3 15 10])
    print -dtiff -r300 veloProfiles
end

figure(3) %Scherraten für verschiedene Geschwindigkeiten
srmin=min([shearRate198 shearRate201 shearRate203 shearRate205 shearRate2 shearRate4↙
shearRate5]);
srmax=max([shearRate198 shearRate201 shearRate203 shearRate205 shearRate2 shearRate4↙
shearRate5]);
plot(rAx5,shearRate5,'c.-')
hold on;
plot(rAx4,shearRate4,'g.-')
plot(rAx198,shearRate198,'m.-')
plot(rAx201,shearRate201,'r.-')
% plot(rAx205,shearRate205,'y.-')
% plot(rAx2,shearRate2,'k.-')
plot(rAx203,shearRate203,'b.-')
hold off;grid, axis([-11 11 srmin srmax])
title('Scherrate bei Stufen: 3 (c), 4 (g), 5 (m), 6 (r), 8 (blue)')
xlabel('r / mm')
ylabel('kappa / 1/s')
if printOpt==1
    set(3,'PaperPosition',[0.63 6.3 15 10])
    print -dtiff -r300 kappaProfiles
end

figure(4) %Viskositäten für verschiedene Geschwindigkeiten
plot(rAx5,1./eta5,'c.')
hold on;
plot(rAx4,1./eta4,'g.')
plot(rAx198,1./eta198,'m.')
plot(rAx201,1./eta201,'r.')
```

```
% plot(rAx205,1./eta205,'y.')
% plot(rAx2,1./eta2,'k.')
hold off;grid, axis tight %, axis([-11 11 -10 20])
title('1/Viskosität bei Stufen: 3 (c), 4 (g), 5 (m), 6 (r), 8 (blue)')
xlabel('r / mm')
ylabel('1/eta / 1/(Pas)')
if printOpt==1
    set(4,'PaperPosition',[0.63 6.3 15 10])
    print -dtiff -r300 viscoProfiles
end
% figure(4) %Viskositäten für verschiedene Geschwindigkeiten
% plot(rAx5,eta5,'c.')
% hold on;
% plot(rAx4,eta4,'g.')
% plot(rAx198,eta198,'m.')
% plot(rAx201,eta201,'r.')
% plot(rAx203,eta203,'b.')
% % plot(rAx205,eta205,'y.')
% % plot(rAx2,eta2,'k.')
% hold off;grid, axis([-11 11 -10 20])
% title('Viskosität bei Stufen: 3 (c), 4 (g), 5 (m), 6 (r), 8 (blue)')
% xlabel('r / mm')
% ylabel('eta / Pa s')
% if printOpt==1
%     set(4,'PaperPosition',[0.63 6.3 15 10])
%     print -dtiff -r300 viscoProfiles
% end

figure(5) %Partikelvolumenkonzentrationen für verschiedene Geschwindigkeiten
phiMin=0.01;          %Partikelvolumenkonzentration für max. NMR-Signal, geraten
plot(rAx5,phi5,'c.') %aus Viskosität
hold on;
plot(rAx5,(1-dens5/max(dens5))*(1-phiMin)+phiMin,'c-')
% plot(rAx205,phi205,'y.') %aus Viskosität
% plot(rAx205,(1-dens205/max(dens205))*(1-phiMin)+phiMin,'y-')
% plot(rAx2,phi2,'k.') %aus Viskosität
% plot(rAx2,(1-dens2/max(dens2))*(1-phiMin)+phiMin,'k-')
plot(rAx4,phi4,'g.') %aus Viskosität
plot(rAx4,(1-dens4/max(dens4))*(1-phiMin)+phiMin,'g-')
plot(rAx198,phi198,'m.') %aus Viskosität
plot(rAx198,(1-dens198/max(dens198))*(1-phiMin)+phiMin,'m-') %aus Spindichte
plot(rAx201,phi201,'r.') %aus Viskosität
plot(rAx201,(1-dens201/max(dens201))*(1-phiMin)+phiMin,'r-')
plot(rAx203,phi203,'b.') %aus Viskosität
plot(rAx203,(1-dens203/max(dens203))*(1-phiMin)+phiMin,'b-')
hold off;grid, axis([-10 10 0 .7])
title('Partikelkonzentration bei Stufen: 3 (c), 4 (g), 5 (m), 6 (r), 8 (blue)')
xlabel('r / mm')
ylabel('phi / -')
if printOpt==1
    set(5,'PaperPosition',[0.63 6.3 15 10])
    print -dtiff -r300 concProfiles
end
```

```
figure(6) %Viskositäten für verschiedene Scherraten
plot(shearRate5,eta5,'c.')
hold on;
plot(shearRate4,eta4,'g.')
plot(shearRate198,eta198,'m.')
plot(shearRate201,eta201,'r.')
plot(shearRate203,eta203,'b.')
% plot(shearRate205,eta205,'y.')
% plot(shearRate2,eta2,'k.')
hold off;grid, axis([srmin srmax -10 20])
title('Viskosität bei Stufen: 3 (c), 4 (g), 5 (m), 6 (r), 8 (blue)')
xlabel('Scherrate / 1/s')
ylabel('eta / Pa s')
if printOpt==1
    set(6,'PaperPosition',[0.63 6.3 15 10])
    print -dtiff -r300 viscoFunction
end

figure(7) %Fließfunktion
plot(shearRate5,shearStress5,'c.')
hold on;
plot(shearRate4,shearStress4,'g.')
plot(shearRate198,shearStress198,'m.')
plot(shearRate201,shearStress201,'r.')
plot(shearRate203,shearStress203,'b.')
% plot(shearRate205,shearStress205,'y.')
% plot(shearRate2,shearStress2,'k.')
hold off;grid, axis tight
title('Fließfunktionen bei Stufen: 3 (c), 4 (g), 5 (m), 6 (r), 8 (blue)')
xlabel('Scherrate / 1/s')
ylabel('shearStress / Pa')
if printOpt==1
    set(7,'PaperPosition',[0.63 6.3 15 10])
    print -dtiff -r300 flowFunction
end


%=========================================================================
%  Subroutine:   rawVeloCalc
%                Ein: Dateiname, Dateigröße, FOF, FOV
%                Aus: Spindichte, Geschwindigkeit und Ortsachse
%  Author:       Silke S. Muckenfuß / Edme H. Hardy
%  Date:         2005/07/19
%  Modifications on 2005/00/00 by EH:
%  Bugs, suggestions, remarks: bisher keine FID BC (DQD!), check threshold,
%  Bereich für die v-Auswertung beachten
%=========================================================================
function [dens,velo,rAx]=rawVeloCalc(fname,spaceMTX,flowMTX,FOF,FOV);

fid=read_raw(fname,spaceMTX,flowMTX,1);

fid=fftshift(fft(fid,[],1),1); %FFT in Ortsraumrichtung
```

```
densAvgThres=0.5*mean(dens(spaceMTX/4:3*spaceMTX/4));   %Für die Bestimmung
for i1=1:spaceMTX/2                                     %der Ränder
    if dens(i1)>densAvgThres
        i1Left=i1;
        break
    end
end
for i1=spaceMTX:-1:spaceMTX/2
    if dens(i1)>densAvgThres
        i1Right=i1;
        break
    end
end
i1Middle=i1Left+(i1Right-i1Left)/2;  %Index für die Mitte
rAx=((1:spaceMTX)-i1Middle)*FOV/spaceMTX; %r axis, 0 at i1Middle

thres=0.1*max(dens); %Schwellwert für zu betrachtende Orte

velo=zeros(1,spaceMTX);
q=1:flowMTX-20;
q=q*2*pi/FOF; %q-Schlange Vektor, verschoben (Null nicht i.d. Mitte), egal
% figure(99)
for i1=1:spaceMTX
    if dens(i1)>thres
        y = squeeze(phase(fid(i1,11:54)))';
%          if mod(i1,10)==0
%              plot(y-y(1)),hold on,pause(.1)
%          end
        X = [ones(size(q'))  q'];
        a = X\y;
        velo(i1)=a(2);
    end
end
% hold off

% i1Middle=find(velo==min(velo));  %Index für die Mitte
% rAx=((1:spaceMTX)-i1Middle)*FOV/spaceMTX; %r axis, 0 at i1Middle

%=========================================================================
%  Subroutine:   shearRateCalc
%                Ein: Geschwindigkeitsvektor, Ortsvektor
%                Aus: Scherratenvektor
%  Author:       Silke S. Muckenfuß / Edme H. Hardy
%  Date:         2005/07/19
%  Modifications on 2005/00/00 by EH:
%  Bugs, suggestions, remarks:
%=========================================================================
function [shearRate]=shearRateCalc(velo,rAx);

dr=rAx(2)-rAx(1);

i1End=length(rAx);
```

```
% for i1=1:i1End-1
%     shearRate(i1)=(velo(i1+1)-velo(i1))/dr;
% end
for i1=2:i1End-1
    shearRate(i1)=(velo(i1+1)-velo(i1-1))/2/dr;
end
shearRate(i1End)=0;


%========================================================================
%  Subroutine:  etaPhiCalc
%               Ein: Scherrate, Druckverlust, Ortsvektor
%               Aus: Viskositätsvektor, Partikelvolumenkonzentrationsvektor
%  Author:      Silke S. Muckenfuß / Edme H. Hardy
%  Date:        2005/07/20
%  Modifications on 2005/00/00 by EH:
%  Bugs, suggestions, remarks:
%========================================================================
function [eta,phi,shearStress]=...
    etaPhiCalc(shearRate,dp_2L,rAx);

phiM = 0.68; %Max. Partikelvolumenkonzentration
eta0 = .45;   %Viskosität ohne Partikel
rAx=rAx/1000; %mm -> m, negativ, damit eta positiv

i1End=length(rAx);
eta=zeros(1,i1End);
phi=zeros(1,i1End);
shearStress=zeros(1,i1End);

for i1=1:i1End
    if shearRate(i1)~=0
        shearStress(i1)=dp_2L*rAx(i1);
        eta(i1)=shearStress(i1)/shearRate(i1); %Viskosität
        if eta(i1)>0
%               phi(i1)=phiM*(1-(eta0/eta(i1))^.5); %↙
Partikelvolumenkonzentrationsvektor
            phi(i1)=phiM*(1-(eta0/eta(i1))^(1/1.82)); %↙
Partikelvolumenkonzentrationsvektor
        end
    end
end
```

Bibliography

[1] A. Nir A. Averbakh, A. Shauly and R. Semiat. Slow viscous flows of highly concentrated suspensions. *Int. J. Multiphase Flow.*

[2] J. Harting A. Komnik and H.J. Herrmann. Transport phenomena and structuring in shear flow of suspensions near solid walls. *J. Stat. Mech.*

[3] A. Nir A. Shauly, A. Wachs. Shear-induced particle migration in a polydisperse concentrated suspension. *J. Rheol.*, 42(6):1329–1348, 1998.

[4] A. Wachs A. Shauly and A. Nir. Shear-induced particle migration in a polydisperse suspension. *J. Rheol.*

[5] J.H. Iwamiya A.W. Chow, S.W. Sinton and T.S. Stephens. Shear-induces particle migration in couette and parallel-plate viscometers: Nmr-imaging and stress measurements. *Phys. Fluids.*

[6] H.A. Barnes. A review of the slip (wall depletion) of polymer solutions, emulsions and particle suspensions in viscometers: Its cause, character, and cure. *Journal of Non-Newtonian Fluids.*

[7] Georg Barthelmes. *Theoretische Untersuchungen zum Einfluss der Agglomeration auf die Rheologie konzentrierter Suspensionen.* Dissertation, Universität Karlsruhe, Karlsruhe, 2000.

[8] C. Bender. *Experimentelle Untersuchungen der Partikeldrift in Suspensionen unter Scherung.* Diplomarbeit, Universität Karlsruhe, Karlsruhe, 2003.

[9] K. Biederbick. *Kunststoffe.* Vogel-Verlag, 1977.

[10] G. Bossis and J.F. Brady. Self-diffusion of brownian particles in concentrated suspensions under shear. *J. Chem. Phys.*

[11] Victor Breedveld. *Shear-Induced Self-Diffusion in Concentrated Suspensions.* Thesis, University of Twente, Enschede, 2000.

[12] H. Brenner and J. Happel. *Low Reynolds Number Hydrodynamics*. Noordhoff International Publishing, Leyden, 1973.

[13] P. Hookham C.J. Koh and L.G. Leal. An experimental investigation of concentrated suspension flows in a rectangular channel. *J. Fluid Mech.*

[14] D.G. Bailey E.C. Eckstein and A.H. Shapiro. Self-diffusion of particles in shear flow of suspension. *J. Fluid Mech.*

[15] B. Khusid G. Drazer, J. Koplik and A. Acrivos. Deterministic and stochastic behaviour of non-brownian spheres in sheared suspensions. *J. Fluid Mech.*

[16] F. Gadala-Maria and A. Acrivos. Shear induced structure in concentrated suspensions of solid spheres. *J. Rheol.*

[17] J.W. Gibbs. Fourier series. *Nature.*

[18] A.J. Goldman. *Investigation in Low Reynolds Numbers Fluid Particle.* Ph.d.thesis, New York University, New York, 1966.

[19] A.L. Graham and S.A. Altobelli. Nmr imaging of shear-induced diffusion and structure in concentrated suspensions. *J. Rheol.*, 35:191–201, 1991.

[20] Fa. Thermo Haake. *Manual of the RheoScope.* Handbook, Ettlingen, Germany.

[21] S. Haber and H. Brenner. Inhomogenous viscosity fluid flow in a wide-gap couette apparatus: Shear-induced migration in suspensions. *Phys. Fluids.*

[22] M. Hartmann. *Beobachtung der Partikelbewegungen in Suspensionen unter Scherung.* Studienarbeit, Universität Karlsruhe, Karlsruhe, 2002.

[23] B.P. Ho and L.G. Leal. Inertial migration of rigid spheres in two-dimensional unidirectional flows. *J. Fluid Mech.*, 65:365, 1974.

[24] A.L. Graham S.A. Altobelli E. Fukushima L.A. Mondy J.R. Abbott, N. Tetlow and T.S. Stephens. Experimental observations of particle migration in concentrated suspensions. *J. Rheol.*

[25] D.F. McTigue J.T. Jenkins. Transport processes in concentrated suspensions: The role of particle fluctuations. *Two Phase Flows and Waves*, 42(6):70–79, Springer Verlag, New York 1998.

[26] I. M. Krieger and T.J. Dougherty. A mechanism for non-newtonian flow in suspensions of rigid spheres. *Transactions of the Society of Rheology*, 3:137–152, 1959.

[27] D. Leighton and A. Acrivos. The shear-induced migration of particles in concentrated suspensions. *J. Fluid Mech.*, 181:415–439, 1987.

[28] M.K. Lyon and L.G. Leal. An experimental study of the motion of concentrated suspensions in two-dimensional channel flow. part 1. monodisperse systems. *J. Fluid Mech.*

[29] H.-M. Laun M. Pahl, W. Gleissle. *Praktische Rheologie der Kunststoffe und Elastomere.* VDI Verlag, Dsseldorf, 1991.

[30] M Navier. Slow viscous flow past a sphere in a cylindrical tube. *Mem. de l'Acad. des Sciences*, 6:388, 1822.

[31] P.R. Nott and J.F. Brady. Pressure-driven flow of suspensions: Simulation and theory. *J. Fluid Mech.*

[32] N. Ohl. *Die Beschreibung des Fliessverhaltens von Suspensionen viskoelastischer Flüssigkeiten bis zu hohen Volumenkonzentrationen.* Dissertation, Universität Karlsruhe, Karlsruhe, 1991.

[33] R.J. Phillips, R.C. Armstrong, R.A. Brown, and J.R. Abbott. A constitutivddde equation for concentrated suspensions that accounts for shear-induced particle migration. *Phys. Fluids*, A4:30–40, 1992.

[34] C.J. Lawrence P.J.A.Hartman Kok, S.G. Kazarin and B.J. Briscoe. Near-wall particle depletion in a flowing colloidal suspension. *J. Rheol.*, 46(2):481–493, 2001.

[35] P.Mills and P. Snabre. Rheology and structure of concentrated suspensions of hard spheres. shear induced particle migration. *J Phys. France.*

[36] J.L.M. Poiseuille. Recherche sur les causes du movement du sang dans les vaiseaux capillaires. *Ann. des Sciences Nature*, 2(5):111, 1836.

[37] J. Raasch. Data values of resistance forces onto particles near solid walls according to formula of happel and brenner. personal communication, 2002.

[38] A.L. Graham N. Tetlow R.E. Hampton, A.A. Mammoli and S.A. Altobelli. Migration of particles undergoing pressure driven flow in a circular conduit.

[39] K. Rottschäfer. *Geschwindigkeitsverteilungen in durchströmten Füllkörperschüttungen.* Dissertation, Universität München, München, 1997.

[40] P.G. Saffman. The lift on a small sphere in a slow shear flow. *J. Fluid Mech.*, 22:385, 1965.

[41] G.W. Scott-Blair. *J. Phys. Chem.*

[42] G. Segr and A. Silberberg. Radial particle displacements in poiseuille flow of suspensions. *Nature*, 189(4760):209–210, 1961.

[43] J.B. Keller S.I. Rubinow. The transverse force on spinning sphere moving in a viscous fluid. *J. Fluid Mech.*

[44] G.G. Stokes. On the effect of internal friction of fluids on the motion of pendulums. mathematical and physical papers 3, 1. *Trans. Camb. Phil. Soc.*, 8:287, 1843.

[45] G.G. Stokes. On the effect of internal friction of fluids on the motion of pendulums. mathematical and physical papers 1, 75. *Trans. Camb. Phil. Soc.*, 9:8/106, 1851.

[46] A. Acrivos U. Schaflinger and H. Stibi. An experimental study of viscous resuspension in a pressure-driven plane channel flow. *Int. J. Multiphase Flow.*

[47] U. Yilmazer and D.M. Kalyon. Slip effects in capillary and parallel disk torsional flows of highly filled suspensions. *J. Rheol.*, 33(2):1197–1212, 1989.

[48] N. Phan-Thien Z. Fang. Numerical simulation of particle migration in concentrated suspensions by a finite volume method. *Journal of Non-Newtonian Fluids.*

pagestyleempty

Lebenslauf

Name	Silke Sandra Muckenfuß
Geburtsdatum	27. Oktober 1974
Geburtsort	Pirmasens

Schulbildung:

1981-1994	Grundschule in Neustadt/Weinstr.
	Leibniz-Gymnasium in Neustadt/Weinstr.
	Abitur am 17. Juni 1994

Studium:

10/1994-12/2000	Studium des Chemieingenieurwesens an der Universität Karlsruhe (TH)
9/1997-8/1998	zwei Auslandssemester an der University of Massachussetts, Amherst

Seminararbeit im Laboratory for Experimental Rheology,
University of Massachussetts, Amherst
(Konzeption und Programmierung einer Software zur Analyse
rheologischer Daten)

Hauptfächer:
- Angewandte Mechanik
- Technische Thermodynamik

Diplomarbeit am
Institut für Mechanische Verfahrenstechnik und Mechanik
der Universität Karlsruhe (TH) bei Prof. Dr. rer. nat. H. Buggisch
*Ermittlung von Zusammenhängen zwischen den rheologischen
und molekularen Eigenschaften eines Polymers*

Promotion:

1/2001-6/2005	Wissenschaftliche Mitarbeiterin am
	Institut für Mechanische Verfahrenstechnik und Mechanik
	der Universität Karlsruhe (TH),
	Bereich Angewandte Mechanik